Investigations on terahertz imaging with pulsed optical parametric oscillator radiation and heterodyne Fourier techniques

Dissertation

Zur Erlangung des Doktorgrades

der Naturwissenschaften

vorgelegt beim Fachbereich Physik

der Johann Wolfgang Goethe -Universität

in Frankfurt am Main

von

Daniel Voß

aus Fulda

Frankfurt 2019

(D 30)

vom Fachbereich 13 der

Johann Wolfgang Goethe - Universität als Dissertation angenommen.

Dekan : Prof. Dr. Michael Lang

Gutachter : Prof. Dr. Hartmut Roskos und Prof. Dr. John Sheridan

Datum der Disputation : vsl. 18. März 2019

Für meine Eltern

Acknowledgements

This work was supported by the European Union through the Marie Curie Action "Industry-Academia Partnership and Pathways", project: "Hyper Spectral Imaging and Sensing" (HYPERIAS) and the HA Hessen Agentur GmbH commissioned by the Hessischen Ministerium für Wissenschaft und Kunst through the action "LOEWE Förderlinie 3: KMU-Verbundvorhaben", project: "Terahertz-Kamera für die zivile Sicherheitstechnik (475/15-17)".

Summary

With the discovery of light beyond human visibility, scientists strove to extend the range of observation to invisible parts of the light's spectrum. Realising that light of all frequencies is part the same physical phenomenon, brought a leap in understanding about electromagnetic waves. With the development of more advanced technology, detectors with higher sensitivity for adjacent frequencies to the visible were built. From this, with each new observable wavelength, more insight into otherwise invisible processes and phenomenons were observed. Hand in hand with this went the enhancement of the output power of corresponding sources. This has lead to higher sensitivity setups throughout the spectrum, leading to observations which have given a deeper understanding in various fields of science. Nowadays, detectors and emitters in many different regions of the invisible electro magnetic spectrum have found their way in our every day life. Innovations in technology has lead to practical applications such as X-rays in medicine, motion sensors and remote controls using infrared light, distance sensors and data transmission using radar and radio devices. The frequency regions above infrared are optically generated and below radar can be produced using electric methods. There is no straight line that separates these frequencies. There rather is a whole intermediate region known as the terahertz (**THz**) regime. Due to the lack of sensitive detectors and efficient sources, the THz frequency region has not been exploited for application use on a widespread basis so far. It combines properties from the surrounding frequency ranges which make it an ideal spectrum for various applications. Consequently, THz radiation and THz imaging are active fields of research.

The work presented in this thesis consists of the development and testing of novel THz imaging concepts, which uses a THz antenna coupled field effect transistor (**TeraFET**) detector. Two detection principles are applied using two different optical setups. The first uses a pulsed optical parametric oscillator (**OPO**) THz source where the optical output power is detected. The source relies on a nonlinear effect of a lithium niobate crystal to generate tunable THz pulses from a Q-switched pump laser. The THz signal is detected and amplified by a double stage operational amplifier for monitoring the real time 20 ns pulses on an oscilloscope where a signal to noise ratio (**SNR**) of ~ 25 at a frequency

range from 0.75 to 1.1 THz is reached. Imaging of the area of interest with a resolution of 1.2 mm is achieved through raster scanning of the THz pulses. Also spectroscopy with a frequency resolution of ~ 50 GHz is demonstrated using a para-aminobenzoic acid sample. The second setup utilises two synchronised electronic multiplier chain sources where their output is mixed on the detector. To form a heterodyne detection setup, the intermediate frequency is fed to a lock-in amplifier which then amplifies the so called beat signal from the TeraFET detector. One source is fixed relative to the detector even through scanning to ensure a stable signal. This detection method allows for amplitude and phase detection for every scanning position, making numerical light field propagation and object reconstruction possible. Numerical focussing is a key feature achieving a lateral resolution of the input transmittance of ≈ 2 mm.

After the introduction, the second chapter describes the setup, measurement results and challenges which arise using a TeraFET together with the pulsed THz source "Firefly-THz". In the description of the setup, special attention is given to the shielding of the detector and the electronics. General findings discuss first the overall performance and later spectroscopy and imaging as application examples. Another subsection continues with potential noise sources before the chapter is concluded. Chapter three expands on the topic of Fourier optics from a theoretical point of view. First, parts of the theory of the Fourier Transform (**FT**) are set out for the reader and how the Fast Fourier Transform (**FFT**) results from the Discrete Fourier Transform (**DFT**). This approach is used for theoretical considerations and the implementation of a Fourier optic script that allows for numerical investigations on electro magnetic field propagation through an optical system. The boundary conditions are chosen to be practical relevant to make predictions on measurements presented in chapter four. The following fourth chapter describes the realisation of a heterodyne THz detection setup. Before the measurement results are presented, the setup and its electric configuration are shown. The results come close to the analytical predictions so that the same algorithm which propagates the field from an object to the Fourier plane is used to propagate the measured field back to the object. The influence of phase noise on the measurement results are discussed before simulation and measurement is compared. The last chapter in this thesis concludes on the findings in the pulsed THz detection and the heterodyne THz Fourier imaging and gives an outlook for both configurations.

Zusammenfassung

Mit dem Wissen von Licht jenseits der menschlichen Sichtbarkeit versuchten Wissenschaftler den beobachtbaren Bereich auf unsichtbare Teile des Lichtspektrums auszuweiten. Die Erkenntniss, dass Licht aller Frequenzen das gleiche physikalische Phänomen ist, brachte das Verständnis der elektromagnetischen Wellen weiter voran. Mit dem Fortschritt von Technologie wurden immer empfindlichere Detektoren für die an die sichtbar angrenzenden Frequenzen gebaut und man erhielt mehr Einsicht in andernfalls unsichtbare Prozesse und Phänomene. Die Verbesserung hinsichtlich der Ausgangsleistung zugehöriger Quellen verlief dazu Hand in Hand. Dies führte zu sensitiveren Messaufbauten über das gesamte Spektrum, was wiederum Untersuchungen zu tieferen Einblicken und Verständnis verhalf. Heutzutage haben viele Detektoren und Quellen in vielen verschiedenen Regionen des elektromagnetischen Spektrums ihren Weg in unseren Alltag gefunden. Von Röntgenstrahlen in Sicherheitsanwendungen und der Medizin über Kameras im sichtbarem Bereich, einschließlich Infrarot in Bewegungsmeldern und Fernbedienungen. Noch langwelliger sind Radarwellen, die in Abstandssensoren und Datenübertragung genutzt werden bis zu Radiowellen, mit der täglich Rundfunk übertragen wird. Wie angedeutet gibt es zwei Bereiche, die sich in der Art und Weise der Strahlungserzeugung unterscheiden lassen. Dabei gibt es keine scharfe Trennung zwischen der niedrigen Infrarotstrahlung und der hochfrequenten Radarwellen. Es ist vielmehr ein ganzer Bereich, den wir heute als terahertz (**THz**) Strahlung kennen. Wegen mangelnder sensitiver Detektoren und effizienten Quellen, hat die THz Frequenz noch nicht ihren Weg in Anwendungen unseres alltäglichen Lebens gefunden. Obwohl sie, durch die Kombination der Eigenschaften angrenzender Frequenzbereiche, für viele Anwendungen interessant ist.

Da die Abbildung von THz Strahlung ein aktives Forschungsfeld ist, gibt es zahlreiche unterschiedliche Ansätze für Messaufbauten. Bis sich für diese jungen Disziplin der THz Forschung eine Lösung als die "Beste" etabliert hat, ist es erstrebenswert möglichst viele verschiedene Umsetzungen zu studieren. Bis zum Beginn dieser Arbeit gab es keine veröffentlichte Forschung von Feld Effekt Transistoren (**FET**) als Detektoren zusammen mit einer optisch parametrischen Oszillator (**OPO**) THz Quelle. Auch der Ansatz der THz Fourier Bildgebung wurde bisher ebenfalls kaum verfolgt. Die vorliegende Arbeit

studiert diese zwei sehr unterschiedlichen Setups, bei denen jeweils ein THz Antennen gekoppelter Feld Effekt Transistor (**TeraFET**) zum Einsatz kommt. TeraFETs sind als empfindliche Detektoren bekannt und finden meist Anwendung mit modolierten (mechanisch oder elektronisch) Dauerstrich Quellen und einem Lock-In-Verstärker. Somit ist die Verwendung von TeraFETs für die Echtzeitmessung von Einzelpulsen und den Einsatz in heterodyner Detektion weitestgehend unerforscht. Folgende Studie trägt dazu bei weitere Schritte auf dem Weg der kommerziellen THz Abbildung zu gehen indem sie das Potential von TeraFETs zusammen mit der kommerziellen OPO THz Quelle "Firefly-THz" und in Heterodynedetektion in der Anwendung tested.

Nach der Einleitung behandelt das zweite Kapitel den Aufbau der gepulsten hochintensitäts THz Quelle. Hier detektiert der TeraFET ähnlich wie ein Photodetektor die Leistung des Ausgangssignals. Die komerzielle Quelle "Firefly-THz" beruht auf einen inter kavitären OPO. Der nichtlineare Effekt im Lithiumniobat Kristall lässt sich ausnutzen, um Frequenz einstellbare ~ 20 ns THz-Pulse aus einem gepulsten Neodym-dotierter Yttrium-Aluminium-Granat-Lasers (**Nd:YAG-Laser**) zu generieren. Zur Detektion wird das Ausgangssignal des Detektors in zwei Stufen mit rauscharmen Operationsverstärkern zu einem mit dem Oszilloskop messbarem Signal verstärkt. Der Güteschalter der Kavität wird mit Hochspannung betrieben und generiert ein Spannungssignal, das in sämtlichen Kabeln des Messaufbaus Rauschen verursachen kann. Da die THz Generierung zeitgleich mit der Güteschaltung stattfindet, kann das THz Signal nicht von dem Schaltprozess getrennt werden. Ohne ausreichende Abschirmung ist dieser Güteschalter Signalschatten um Größenordnungen stärker als das eigentliche THz Signal. Die Abschirmung des Detektors, Verstärker und beider Spannungversorgungen stellt einen maßgeblichen Schritt zum erfolgreichen Einsatz dieses Messaufbaus dar. Besonders wichtig sind Kabel, die elektrisch vor dem Eingang des Verstärkers liegen. Bei erfolgreicher Abschirmung werden Einzelpulse ohne Mittelung mit einem Signal zu Rausch Verhältnis (**SNR**) und Dynamik von > 20 bzw. > 300 bei 0.8 THz aufgenommen. Im Einsatz des TeraFET Detektors mit dem "Firefly-THz" zeigt sich, dass die Austrittsleistung hoch genug ist den Detektor in Sättigung zu treiben, was vielversprechend für potentielle Multidetektion und Kameraanwendungen ist. Die Pulsbandbreite von ~ 50 GHz der Quelle lässt die Aufnahme eines Spektrums zu, wodurch Karakteristiken von unterschiedlichen Materialien zwischen 0.7 THz und 2 THz detektiert werden können. Am Beispiel von para-Aminobenzoesäure **PABA** ist das Absorptionsspektrum aufgenommen. Im gleichen Kapitel wird die Bildgebung in Transmission anhand einer Leiterplatte demonstriert, bei der eine Auflösung von ~ 1.2 mm erreicht wird. Schließlich wird genauer auf die Auswirkungen des Güteschalters und potentielle Kaskardeneffekte im optischen parametrischen Oszillator thematisiert.

Während die Auswirkungen des Hochspannungssignals weitestgehend unterdrückt werden können, sorgen diese Kaskardeneffekte dafür, dass die strikte Korellation von THz Signal und Infrarot Signal beeinträchtigt ist. Insbesondere für Frequenzen hoher Austrittsleistung ist die Korrelation nicht gegeben.

Ein weiterer Hauptteil der Arbeit umfasst theoretische Untersuchungen zur Fourier Bildgebung. Zunächst wird das grundlegende Prinzip und die mathematischen Eigenschaften der Fouriertransformation erleutert. Aus dem Fresnel Integral und der Phasen Transformation einer Linse wird eine Formel zur Propagation eines Lichtfeldes zur Focus Ebene einer Linse aufgestellt. Mit Hilfe von numerischen Algrorithmen werden Eigenschaften dieser Propagationsformel untersucht. Die resultierende komplexe Amplitude (Intensität und Phase) in der Fourier Ebene von unterschiedlichern Objekten wird berechnet und nach gezielten Modifikationen dieser mit der invertierten Propagationsformel numerisch zurück propagiert. Entgegen der gewöhnlichen Bildgebung, bestimmt die Auflösung in der Fourier Ebene den Abbildungsbereich der Objektebene und der Detektionsbereich in der Fourier Ebene bestimmt die Auflösung in der Objektebene. Dies ist direkt auf die Eigenschaft der Fourier Transformation zurück zu führen und insbesondere für Messungen relevant. Während ein unveränderter Datensatz (Inensität und Phase) in einem genauen Abbild der Eingabe Transmittät resultiert, erzeugt Beschnitt, Rauschen oder abweichende Parameter der Gleichung Veränderungen des Abbildes der Eingabe. Zufälliges Rauschen in Intensität und Phase wirkt sich unterschiedlich stark auf die Berechnung der Eingabe aus. Während relatives Rauschen der Intensität einen eher geringen Effekt hat, ist ein Rauschen der Phase als deutlich kritischer für eine klare Abbildung einzustufen. Ein Beschnitt der Raumfrequenzen in der Fourier Ebene führt zur reduzierten Auflösung des zurück gerechneten Objektes, kann aber auch gezielt für die Auswahl bestimmter Raumfrequenzen und damit Merkmale des Objektes genutzt werden. Die genaue Kenntnis über die Frequenz der verwendeten Strahlung, der Brennweite der Linse und die Distanz von Objekt zur Linse spielen ebenfalls eine entscheidende Rolle. Bei der Wahl einer Distanz für die zurück Propagierung, kommt es nur zu einer scharfen Abbildung, wenn diese der tatsächlichen Distanz der Eingangstransmission zur Linse ist. Dies sorgt für einen weiteren Parameter, der bei einer Messung berücksichtigt werden muss. Allerdings bedeutet dieser Zusammenhang auch, dass mit einem Bild in der Fourier Ebene zusätzlich zur lateralen Abbildung ebenfalls ein Tiefeneindruck generiert werden kann. Dies zeigt sich in einer Simulationsreihe, bei der die virtuelle Distanz variiert wird und nur dann eine scharfe Abbildung durch die Rekonstruktion erreicht wird, wenn die benutzte und virtuelle Distanz übereinstimmen.

Im zweiten hier vorgestellten Messaufbau findet wieder ein TeraFET als Detektor Anwendung. In diesem Fall aber, wird durch heterodyne Detektion die Messung der komplexen Amplitude (Intensität und Phase) ermöglicht. Dazu kommen zwei elektronische 300 GHz Vervielfacher Quellen zum Einsatz, deren Austrittsstrahlung auf dem Detektor gemischt wird. Eine der Quellen ist dabei relativ zum Detektor fixiert und dient als Lokaloszillator. Sie ist über einen Strahlteiler oder in einer späteren Konfiguration von der Luft aus direkt auf den Detektor fokussiert. Die zweite Quelle oder auch Signalquelle sitzt auf einer drei dimensionalen Verschiebeeinheit. Zur Erzeugung eines Bildes wird die gesamte Verschiebeeinheit über den zu untersuchenden Bereich zweidimensional gescannt während der Detektor in der Fokusebene der Linse steht. Wie in der theoretischen Betrachtung wurden unterschiedliche Objekte studiert. Da die Messungen den numerischen Untersuchungen nachempfunden sind, lassen sich viele Ergebnisse aus der Simulation in der realen Messung wieder finden. So lässt sich mit Intensität und Phase der Fourier Ebene über den gleichen Algorythmus das Objekt mit einer Auflösung von ~ 2 mm rekonstruieren. Hier zeigt sich vor allem, dass die Gaussische Intensitätsverteilung der Signalquelle und die Limitierung der Detektionsfläche zum Teil großen Einfluss auf das berechnete Objekt haben. Da dies in der Simulation bereits antizipiert wurde, lassen sich in der Messung im direkten Vergleich mit äquivalenten Simulationen eine Korrelation von bis zu 73% nachweisen. Auch die Sensitivität der Entfernung des Objekts zur fokussierenden Linse kann in einer Messreihe bestätigt werden. Während die Abbildung mehrerer Objekte hintereinander noch eine Herausvorderung darstellt, werden im Weiteren störende Effekte und Rauschen analysiert. Wie bereits in den Simulationen dargestellt, wird auch hier das Rauschen der Phase als kritischer eingestuft als das der Intensität. Außerdem kommt es in der Messung zu stehenden Wellen, die durch koherente Reflektionen verursacht werden. Dadurch ergibt sich nicht nur in der Intensität sondern auch in der Phase ein Rauschen, was die Rekonstruktion stark beeinflussen kann. In der Diskussion dieses Kapitels werden beiden Konfigurationen (mit Strahlteiler und ohne Strahlteiler) des verwendeten heterodyne Messaufbaus eine ähnliche Leistungsfähigkeit zugeschrieben. Allerdings wird der einfachere, lineare Messaufbau, der keinen Strahlungsteiler benötigt, als dieser mit höherem Potential eingestuft.

Die vorliegende Arbeit ist wie folgt strukturiert. Die Einleitung gibt einen Einstieg in das Thema der THz Bildgebung. Nach der Einleitung beschreibt das zweite Kapitel den Aufbau, Messergebnisse und Herausvorderungen, die aus dem Einsatz eines TeraFET Detektor mit der gepulsten THz Quelle "Firefly-THz" resultierten. Während der Erläuterung des Aufbaus wird besonderes Augenmerk auf die Abschirmung des Detektors und der Elektronik gelegt. Ergebnisse der Messung gehen zunächst auf die allgemeine Performance

des Messaufbaus ein, während im Weiteren Spektroskopie und Bildgebung als Anwendungsbeispiele beleuchtet werden. Ein weiteres Unterkapitel greift potentielle Störquellen auf, bevor das Kapitel mit einem Fazit endet. Kapitel drei greift das Thema der Fourier Optik in einer theoretisch basierten Betrachtungsweise auf. Zunächst werden Teile der Fourier Transformationstheorie dargelegt und wie die Diskrete- aus der Schnellen Fourier Transformation resultiert. Dieser Ansatz wird für theoretische Überlegungen und die Implementierung eines Fourier Optik Skripts benutzt, das numerisch die Propagation von elektromagnetischen Feldern durch ein optisches System untersucht. Dabei wird bei der Wahl der untersuchten Objekte großen Wert auf Praxisnähe gelegt, um Vorhersagen für die in Kapitel vier vorgestellten Messungen machen zu können. Das folgende Kapitel vier befasst sich dann mit der Realisierung eines heterodyne THz Detektionsaufbaus. Vor der Präsentation der Messergebnisse wird die besondere Anordnung der zwei elektronischen Vervielfacher-Quellen in der Setup Beschreibung zum Thema gemacht, wobei die Wichtigkeit der elektronischen Anordnung nicht zu unterschätzen ist. Die Resultate der Messung sind so nahe an der analytischen Vorhersage, dass die selben Algorithmen, die schon in Kapitel drei genutzt werden um ein elektrisches Feld vom Objekt zur Fourier Ebene zu propagieren, auch dazu genutzt werden können die Felder aus den Messdaten zurück zum Objekt zu verfolgen. Da die Phase ein essenzieller Parameter ist, hat dessen Rauschen einen großen Einfluss auf die Rekonstruktionsqualität des Objektes. Abweichungen können mit Phasenrauschen unterschiedlicher Ursprünge begründet werden. Dies wird erörtert, bevor der nächste Abschnitt die Ergebnisse von Simulation und Messung vergleicht und evaluiert. Das letzte Kapitel fasst die Befunde der Aufbauten gepulster THz Detektion mit Echtzeit Abbildungspotential und hetorodyn THz Fourier Bildgebung zusammen und gibt einen Ausblick in zukünftige Untersuchungen.

Contents

Author's contributions

Parts of this work are already published in a journal and presented on two conferences:

[1] W. Zouaghi, D. Voß, C. McDonnell, D. Mundy, J. R. P. Bain, N. Hempler, G. P. Malcolm, G. T. Maker, A. Rämer, S. A. Chevtchenko, W. Heinrich, V. Krozer, and H. G. Roskos, "Real-time detection of the thz pulses from a thz opo using algan/gan terafets", in *41st International Conference on Infrared, Millimeter, and Terahertz waves (IRMMW-THz)*, 2016.

[2] D. Voß, W. Zouaghi, M. Jamshidifar, S. Boppel, C. McDonnell, J. R. P. Bain, N. Hempler, G. P. A. Malcolm, G. T. Maker, M. Bauer, A. Lisauskas, A. Rämer, S. A. Shevchenko, W. Heinrich, V. Krozer, and H. G. Roskos, "Imaging and spectroscopic sensing with low-repetition-rate terahertz pulses and gan terafet detectors", *Journal of Infrared, Millimeter, and Terahertz Waves*, vol. 39, no. 3, pp. 262–272, Mar. 2018. DOI: 10.1007/s10762-017-0447-1.

[3] K. Ikamas, J. Zdanevičius, L. Dundulis, S. Pralgauskaité, A. Lisauskas, D. Cibiraitė, D. Voß, V. Krozer, and H. G. Roskos, "Quasi optical thz detectors in si cmos", in *2018 22nd International Microwave and Radar Conference (MIKON)*, May 2018, pp. 719–721. DOI: 10.23919/MIKON.2018.8405336.

1 Introduction

Processing visual data has been vital for survival of the human race. Therefore, it is not surprising that evolution equipped humans with a brain capable of super efficient image processing. Through the centuries, countless discoveries and findings have been driven by the observation abilities with the naked eye and later with various optical instruments like telescopes and microscopes. With the discovery of radiation beyond the visible spectrum [1, 2], studies were undertaken to detect these frequencies with higher and higher sensitivity. Following this, it was discovered that not only the short wavelength of X-rays but also radio frequencies are all manifestations of the same physical phenomenon [3]. Detectors extended the range in which humanity gathers information about nature and its characteristics [2, 4, 5]. As a result, systems with imaging capabilities were developed to present captured data in one of the most natural ways – through visualisation. For example X-ray imaging is of major importance for medical and security purposes, infrared based night vision cameras are commercially available for police surveillance, military and natural science. Also radiation in the radar frequency band is imaged with modern technology for weather screening, topography investigations or military use. Radar radiation is produced electrically and therefore not counted to the optical regime, although it is just a lower frequency.

The regime in between radar and infrared frequencies is called the THz regime where both, electrical and optical methods face challenges to produce and/or detect radiation. It is also known as the "THz-gap", because of the lack of a source or detector for this radiation. Nowadays, there are enough methods to fill the gap, however sources and detectors lack output power or sensitivity compared to microwave and radar frequencies. The THz radiation bridges the gap between the adjacent radio and infrared frequencies

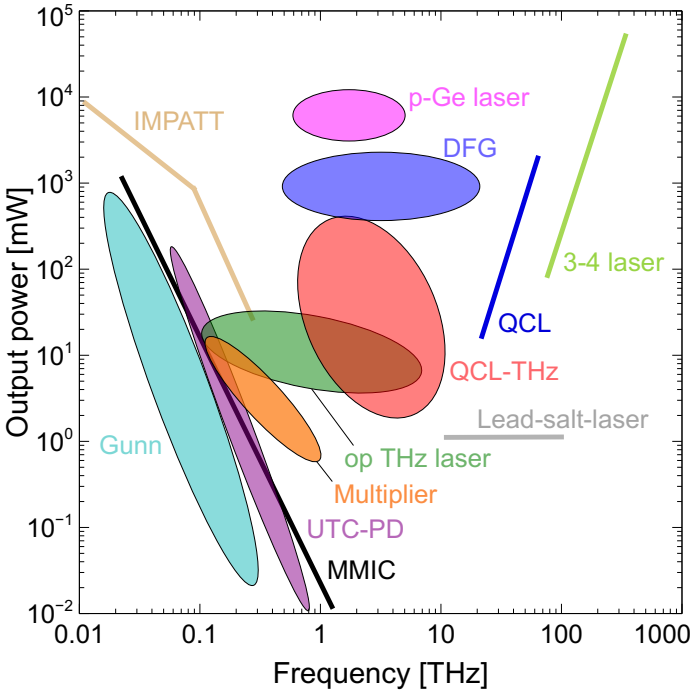

Figure 1.1: Typical output power of various THz sources as a funciton of frequency. MMIC stands for microwave monolithic integrated circuit, TUNNET stands for tunnel injection transit time, IMPATT stands for impact ionisation avalanche transit-time diode, DFG stands for difference frequency generation, Gunn stands for Gunn diodes, UTC-PD stands for uni-travelling-carrier photodiode, Multiplier for frequency multiplier, op THz laser stands for optical pumped THz laser and QCL for quantum cascade laser [6–8].

featuring characteristics of both. Hence, mirrors and lenses for THz radiation have a manageable size to guide the beam and to form reflective and refractive optics for setups like any other optical regime. Additionally, materials like paper, cardboard, plastics and clothing are transparent which allows insight into packaging, boxes and clothing. The photon energy is too small to ionise atoms and thus unharmful to living cells in contrast to X-rays. Consequently, THz radiation is an active research field with growing interest especially in THz imaging. Spectroscopy and imaging with THz radiation holds the potential to be used in many different application fields such as from medical diagnostics, imaging material properties to security screening [9]. For this purpose, desirable THz sources often have a (quasi-) continuous wave THz radiation output. Various classes of different sources have been developed over the past years. Figure 1.1 shows a few

different approaches where THz frequencies of > 1 THz can be reached with cooled quantum-cascade lasers or difference frequency generation and p-Ge laser. Below 0.7 THz, electronic emitters based on multiplier chains are widespread. Both frequency ranges can be covered by photoconductive mixers (not displayed), which down converts the radiation of near-infrared lasers down to THz frequencies, with the drawback of limited beam power [10]. Optical pumped THz lasers are an attractive alternative which present a tunable table top solution which operate at room temperature.

For any measurement setup, the detector is just as important as the source. Without a responsive detector, even high output power cannot be detected. There are various types of detectors based on different which can be sensitive to THz radiation. For example, the broad class of bolometers where the energy carried by the THz radiation is deposited and detected in the system. Prominent solutions are hot electron bolometers, micro bolometers or the "Golay Cell" [11–16]. While those detectors are most often sensitive for a broad range of THz radiation, other detector types like Schottky barrier diodes or field effect transistors (**FET**) are designed for a certain selected frequency range. Coupled with a THz antenna, the latter achieve a noise equivalent power (**NEP**) of < 20 nW in video mode at 25 Hz frame rate [8].

The main goal for this work is to investigate two new detector source setups, and evaluate their performance for THz imaging. The first setup combines a FET detector to a pulsed low repetition Q-switched optical parametric oscillator (**OPO**) THz source. The second setup presented in this work studies the possibility of heterodyne detection in a Fourier imaging setup in the THz regime, mixing the output of two electronic multiplier chain THz sources. These two approaches on THz imaging broadens the application area of known sources as well as detectors.

2 Pulsed terahertz detection

Table-top THz sources with enabled tunability tend to lack in output power which leads to a lower signal to noise ratio (**SNR**) in imaging solutions (see (2.1)). A Q-switched optical parametric oscillator (**OPO**), considering its size and room temperature operation, can emit large output powers. It produces frequency tunable nanosecond long pulse trains at a low repetition rate [17, 18]. As a result, the OPO is able to generate high pulse energies with high peak power. A commercially available implementation of an OPO is used for the study presented in this work [19]. This technique has been demonstrated with success for various different detection schemes [20, 21]. Another alternative detection method is represented by the THz antenna coupled field effect transistor (**TeraFET**) power detectors, which are based on antenna coupled field-effect transistors. They have already been proven to be competitive power detectors for THz radiation [22–25]. The fabrication of these devices is exclusively done by a standard microelectronic foundry process and therefore relatively cheap in mass production. The regime with the highest responsivity can be designed to be anywhere between gigahertz frequencies and beyond 10 THz [26–28]. This chapter starts with a step wise description of the setup, followed by a section about the measurements presenting general findings and demonstration of application in spectroscopy and imaging. A discussion of limitations and possible improvements of the SNR closes the chapter.

2.1 Setup of pulsed terahertz detection

As mentioned above, the measurements presented in this chapter are done with a commercial available Q-switched OPO named "Firefly-THz" developed by M Squared Lasers

as a source and an antenna coupled field effect transistor detector. Figure 2.1 shows a sketch and a photograph of the setup on the left and the right side, respectively. It consists of the detector, the sample, a linear xyz-translation stage, a parabolic mirror and the Firefly-THz source. Not displayed is the amplifier, the 40 MHz digital oscilloscope and the computer which controls the translation stage as well as the oscilloscope and the Firefly-THz. The radiation pulse trains with a frequency between 0.7 and 2.5 THz leave the output window of the Firefly-THz (see section 2.1.1) nearly collimated and hit the parabolic mirror. The four inch mirror focuses the radiation onto the sample which can be scanned with the translation stage through the focus and the transmitted radiation is collected by the shortly after mounted detector (see section 2.1.2). Directly connected to the detector is the double stage amplifier (see section 2.1.3) which amplifies the signal and passes it to the oscilloscope. This is used to digitise the analogue output of the amplifiers and transfer the acquired data with an optional pulse integration to the computer where it is stored for evaluation and post processing.

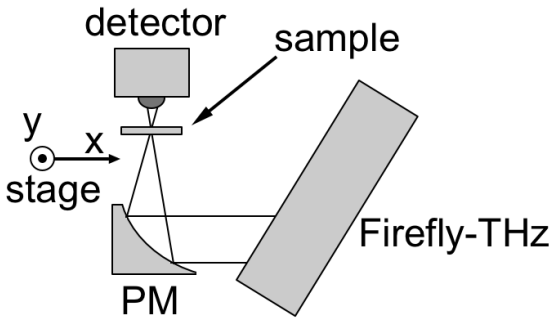

(a) Sketch of the used setup

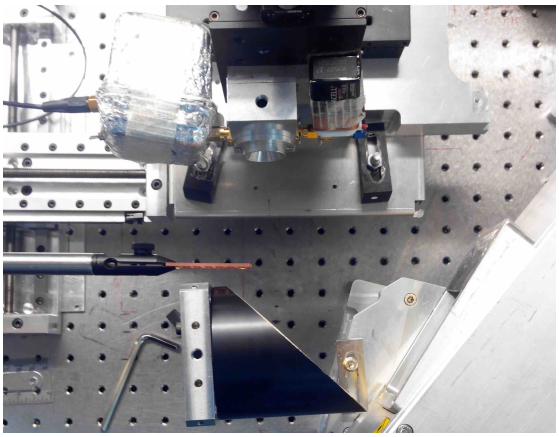

(b) Picture of the used setup

Figure 2.1: (a) Sketch of the setup with detector, sample, xyz-translation stage, parabolic mirror (PM) and the Firefly-THz source. (b) Image of the major part of the used setup. [1]

Two of the most important characteristics of any measurement setup are the SNR and the dynamic range (DR). They are used to determine the performance of a setup and

[1] Reprinted by permission from Springer Nature: Springer JIMT, "Imaging and Spectroscopic Sensing with Low-Repetition-Rate Terahertz Pulses and GaN TeraFET Detectors", Daniel Voß et al., 2018

are directly linked to the ability of measuring small deviations as well as a big range of signal strength. Those two values are mainly influenced by the source and the detector characteristics as well as the integration time over which the signal is averaged. Both important values can be calculated following the approach of [29]. The SNR can be calculated with,

$$SNR = \frac{S_{mean}}{S_{std}}, \tag{2.1}$$

where S_{mean} is the average peak signal of the detector and S_{std} the standard deviation of the peak detector signal defined as,

$$S_{mean} = \frac{1}{N}\sum_{i=1}^{N} x_i, \qquad \text{and} \tag{2.2}$$

$$S_{std} = \sqrt{\frac{1}{N}\sum_{i=1}^{N}(x_i - S_{mean})^2}, \tag{2.3}$$

where N stands for the total number of measurements and x_i the value of the ith measurement. Note, x_i can be an averaged value itself. The DR can be easily calculated as well,

$$DR = \frac{S_{mean}}{N_{rms}}, \tag{2.4}$$

where S_{mean} stands again for the signals average peak signal and N_{rms} stands for the root mean square of the noise floor (without signal) calculated by,

$$N_{rms} = \sqrt{\frac{1}{N}\sum_{i=1}^{N} x_{noise,i}^2} \ . \tag{2.5}$$

2.1.1 Firefly-THz source

The commercial available THz source "Firefly-THz" from M Squared Lasers Ltd is an optical parametric oscillator (OPO) which consists of a Q-switched Nd:YAG laser with its cavity between mirror M1 and M2 (see Fig. 2.2) [18]. The Nd:YAG crystal (LG) is pumped by a temperature controlled laser diode. The Nd:YAG laser provides the near-IR pulses for the nonlinear optical parametric process inside the lithium niobate crystal (LN)

which is also placed inside a secondary cavity consisting of mirror M3 and M4. The THz radiation is coupled out by silicon prisms. The OPO gains frequency tunablility by rotating the LN crystal together with the hole secondary cavity arm relative to the main cavity axis. During the optical parametric oscillator process one pump photon $\vec{k}_p$ is split in a

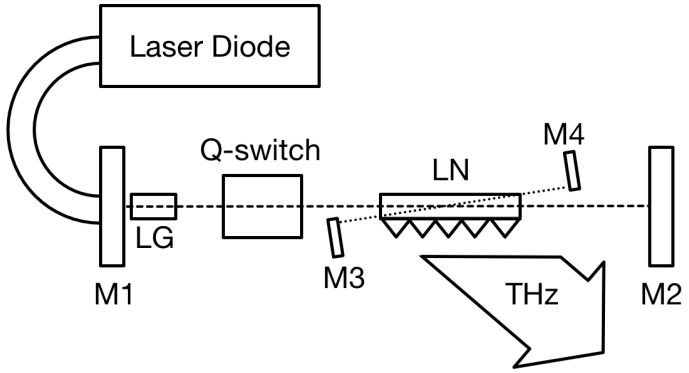

Figure 2.2: Schematic of the Q-switched OPO "Firefly-THz". Printed are the Laser Diode, the four cavity mirrors M1-M4, the Nd:YAG crystal (LG), the Q-switch and the nonlinear lithium niobate crystal (LN).

signal photon with wave vector $\vec{k}_s$ and an idler photon with the wave vector $\vec{k}_i$. Energy conservation has to be satisfied so that (see Fig. 2.3),

$$\vec{k}_p = \vec{k}_s + \vec{k}_i. \tag{2.6}$$

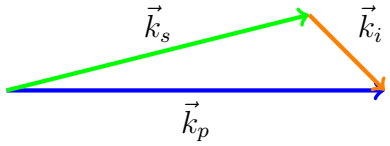

Figure 2.3: Photon energy down conversion

The pulses which leave the output window under an angle of $\sim 30°$ (slightly dependent on the output frequency) to the normal axis are ~ 25 ns long, each [18]. The pulses can be triggered externally within a rather low repetition range from 20 to 90 Hz which leaves the pulse energy constant at > 10 nJ [18]. Whereby, the maximum output energy is only reached at 1.3 THz in the center of the frequency tune window between 0.7 and 2.5 THz (see Fig. 2.7a). The pulses are narrowband with a spectral width ≈ 50 GHz. The output radiation is detected by a TeraFET described below.

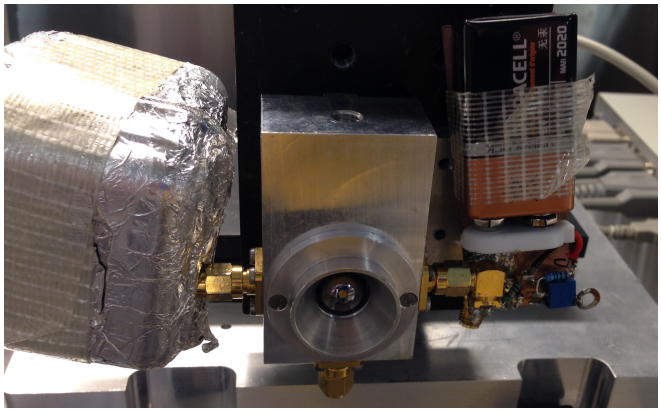

(a) Picture of the detector box

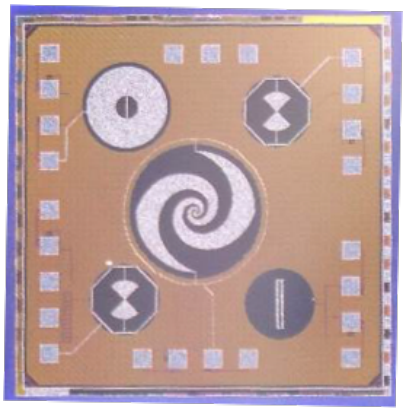

(b) Detector chip

Figure 2.4: (a) Shown is a photograph of the amplifier box (left), detector (center) and its gate voltage supply (right). (b) The detector chip with two bow-tie atennas (bottom left and top right), a spiral antenna (middle) and a dipol (bottom right) and disk (top left) antenna.

2.1.2 Field effect transistor detector

The antenna coupled field effect transistor (TeraFET) detection principle is based on resistive mixing [30, 31]. For higher frequencies higher than the transit-time frequency, its behaviour is altered and plasmonic effects in the channel become notable [25]. TeraFETs in CMOS technology have been used to implement on-chip focal plane arrays and THz cameras [32–35]. With respect to the high output power of the Firefly-THz and the thread of degenerating the buffer layer in the CMOS device, one decided in favour for the more robust [36] AlGaN/GaN high-electron-mobility transistor (**HEMT**) technology [37–39]. The present detector is coupled with a bow-tie antenna (see Fig. 2.4b) featuring an optical noise-equivalent power (NEP) of $\leq 31\text{pW}/\sqrt{\text{Hz}}$ obtained in a frequency range of maximal sensitivity from 0.49 to 0.65 THz [37].

For the experiments, the detector is housed in a metal box, which only leaves one opening for the substrate mounted hyperhemispherical silicon lens with a diameter of 12 mm [40, 41]. The metal box is grounded to minimise the influence of the Q-switch induced high electromagnetic pulsed field. The required -1.7 V gate voltage is provided by a potential divider hooked up to a usual 9 V battery. This is necessary to keep cables as short as possible in order to reduce noise picked up by these cables.

2.1.3 Double stage amplifier

Usually, the above described TeraFET detector is used together with a lock-in amplifier and a chopped (electrical or mechanical) THz source. A typical repetition rate would be in the order of 1 kHz with an integration time of several milliseconds. Since the repetition rate of the Firefly-THz is low (see above), a different approach is chosen. The chosen solution is a double stage amplifier ($10\times$ each) whose input is directly connected (without intermediate cable) to the detector. Figure 2.5 shows the electrical circuit. R_1, R_2 and R_3 are resistors whose resistance can be adjusted for different amplification factors. In the case of two $10\times$ amplification, R_1, R_2 and R_3 are chosen to be $470\ \Omega$, $47\ \Omega$ and $470\ \Omega$, respectively. A first version of this circuit is soldered by hand in order to be able to investigate on appropriate operational amplifiers and amplification factors. After the circuit was established, PCB amplifiers are produced and utilised in a more compact version double stage amplifier. In order to reduce the before mentioned Q-switch influence, the amplifier is housed in a metal box with batteries as the power supply also included in the housing (see 2.4a). Due to capacities within the circuit (connections and others), the output pulse is broadened to ~ 250 ns full width at half maximum (see Sec. 2.2.1) compared to the original THz pulse of 25 ns. The output pulse of the amplifier circuit is without integration directly connected to the digital oscilloscope which is triggered to show the signals voltage pulse.

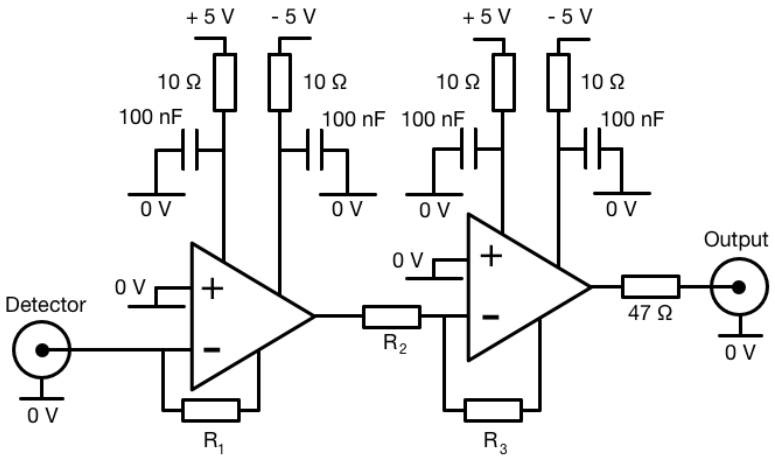

Figure 2.5: Sketch of the used double stage amplifier circuit. Resistors R_1, R_2 and R_3 are variable to tune the amplification factor.

2.2 Experimental results

In order to estimate the full system potential, the setup presented above is used for different measurements. First, some general findings of the system like signal pulse shape, frequency response, SNR and DR are presented. Afterwards, spectroscopy and imaging as potential applications are discussed in more detail.

2.2.1 General characteristics of the setup

TeraFET detectors have not been paired with Q-switched OPO THz sources in previous research. As such, preliminary investigations into the basic interaction properties of the source and detector must be undertaken first. Since the pulsed source has a repetition rate < 90 Hz, a lock-in amplifier would have to integrate over a big fraction of a second to provide reasonable data. As described before, a double stage amplifier circuit is used to amplify the output's signal. However, the Q-switch of the OPO uses a high voltage to switch the high power Nd:YAG laser. This voltage spike on the power supply can be picked up by any cable. This has to be avoided for the measurement since the Q-switch induced voltage peak masks the actual THz signal of the detector (see section 2.3.1). Figure 2.6 shows an example THz signal pulse (black) and the corresponding (of the non-linear process) IR pulse (red). The 0.8 THz pulse is recorded with the detector and amplified by the double stage amplifier and digitalised with the oscilloscope before being transmitted to the computer. The red pulse is the corresponding IR pulse created in the OPO process and measured with a commercially available photo diode also connected to the oscilloscope.

Because of the Firefly-THz sources tuning range from 0.7 THz to 2.6 THz, it is possible to measure a corresponding output spectrum (see Fig. 2.7a). This measurement is performed in a normal laboratory environment. Therefore, one can identify water absorption lines in the spectrum measured with the Golay Cell (red). Unfortunately, the design frequency of the TeraFET detector lies outside of the tuning range of the source. This can be seen by the signal dropping over the entire frequency range. Even though the maximum output (according to the Golay Cell) is at 1.3 THz, the signal of the GaN/AlGaN

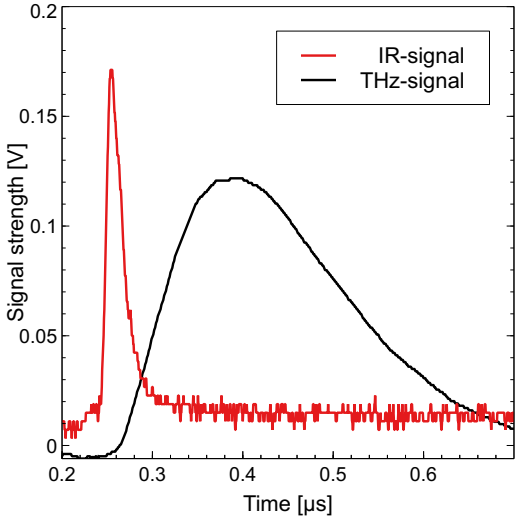

Figure 2.6: THz pulse example (black), measured with the TeraFET detector and amplified by the double stage amplifier with its corresponding IR pulse (red), measured with a photo diode.[2]

detector at this frequency falls down to one quarter of the signals strength at 0.8 THz. Note that the y-axis of the GaN/AlGaN detector is on the left side in black and the y-axis for the Golay cell on the right in red. Each data point represents an integration over 128 pulses done internally on the oscilloscope.

In order to determine the SNR and DR of the setup using the GaN/AlGaN detector, equations (2.1) and (2.4) are used with N, the number of measurements being 1000 for each frequency point, where the maximum of each pulse is taken as x_i in the formulas. The noise root mean square (N_{rms}) is calculated again with 1000 samples but since the noise floor is invariant with the frequency it is just taken for one frequency and applied to all others. Both graphs, SNR and DR against frequency, are shown in figure 2.7b. Note that the y-axis for the SNR is on the left in black while the y-axis for the DR is shown on the right. If one compares the trend of the DR with the trend of the frequency spectrum, it can be seen that the DR follows the slope of the maximum signal in the spectrum decreasing from > 350 at 0.75 THz down to 40 at 1.3 THz. This is expected since the definition of the dynamic range is the signals magnitude divided by the noise's

[2]Reprinted by permission from Springer Nature: Springer JIMT, "Imaging and Spectroscopic Sensing with Low-Repetition-Rate Terahertz Pulses and GaN TeraFET Detectors", Daniel Voß et al., 2018

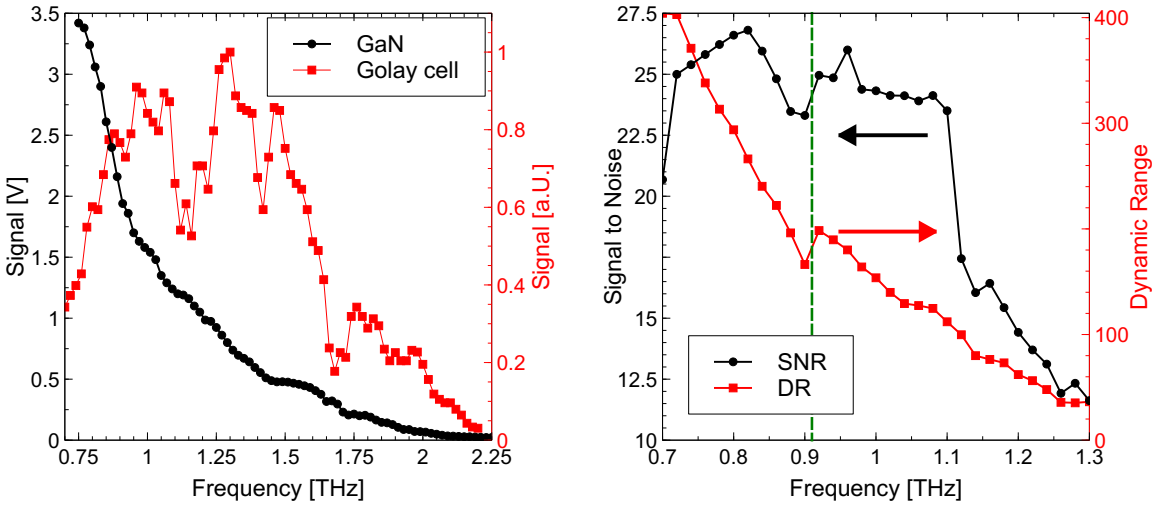

(a) Frequency spectrum

(b) SNR and DR vs. frequency

Figure 2.7: (a) Frequency sweep measured with the Golay Cell (red) and the GaN TeraFET detector (black). (b) Obtained signal to noise ratio (SNR) and dynamic range (DR) as a function of tuning frequency.[3]

root mean square N_{rms}, with the latter being constant over frequency and several orders lower than the signal but dominated by the Q-switch noise (even when reduced by the shielding measures). The green dashed line at 0.91 THz indicates a small readjustment of the detectors position which is necessary since the output angle and therefore the position of the focus shows a small drift as a function of output frequency [18]. This caused the DR and SNR to increase slightly after the readjustment. The frequency dependence of the SNR shows different behaviour. It rises shortly after the lower end of the tuning range to ~ 25 and stays nearly constant up to 1.2 THz. The relatively low value of the SNR is a consequence of the high pulse to pulse fluctuations of the laser source, increasing the standard deviation of the signal S_{std}. The fact that the SNR stays constant till 1.1 THz results from the similar frequency behaviour of S_{mean} and S_{std} over a frequency range of nearly 0.4 THz. This is not surprising, since the detector is operated in the linear response regime. The reason why the SNR drops after 1.1 THz is not clear. Water absorption lines can be taken out of consideration since unless the humidity changed quickly during

[3]Reprinted by permission from Springer Nature: Springer JIMT, "Imaging and Spectroscopic Sensing with Low-Repetition-Rate Terahertz Pulses and GaN TeraFET Detectors", Daniel Voß et al., 2018

measurement of one frequency point, a general signal reduction should keep the ratio between S_{mean} and S_{std} constant. An explanation for the SNR behaviour could be the additional non-linear effects during THz generation which is discussed in section 2.3.2.

2.2.2 Linearity measurements

Another important characteristic is the detector's response, which is most often preferred to be linear. This is tested by the highest value of each averaged (64 pulses) signal from the oscilloscope as a function of beam power. The detector is placed in the focus of the parabolic mirror without any sample. Post-it sticky notes are used to gradually attenuate the signal. This is done to have an equal staying attenuation step per post-it, which is roughly 0.5 dB per note paper. The exact value is dependent on the humidity of each note as well as the frequency. Figure 2.8 shows a selection of three frequencies (0.9, 1.0 and 1.1 THz). Each frequency graph is normalised to its individual power maximum with

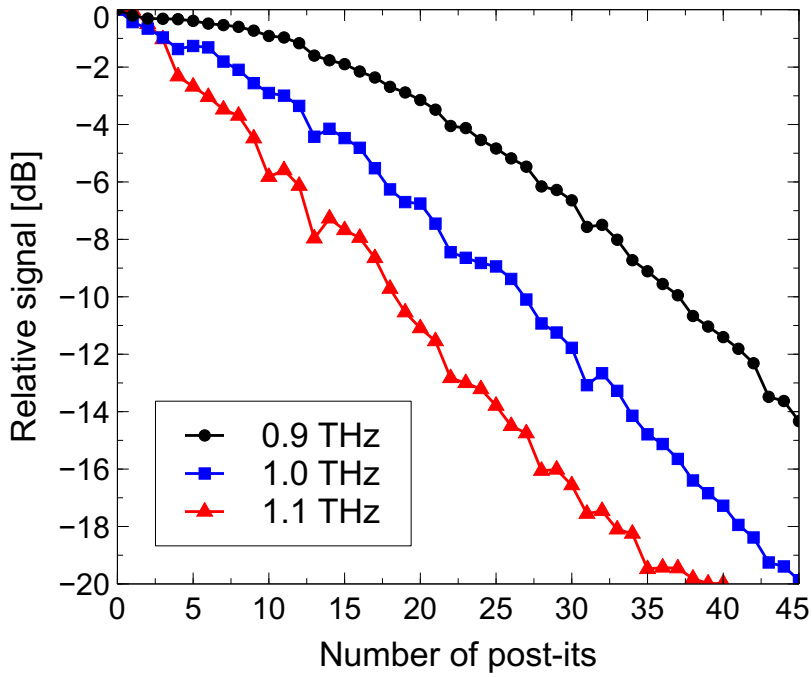

Figure 2.8: Gradually attenuation with post-it sticky note paper of the THz signal at frequencies 0.9, 1.0 and 1.1 THz measured with the bow-tie antenna detector. For each frequency the signal strength is normalised to the full signal for each frequency.[4]

no post-its inserted in the beam path. The graphs show a linear behaviour between the measured signal and the output power for the majority of the laser output power. They also show that the detector can be driven in saturation at frequencies below 1.0 THz. This is visible in a changing slope towards the number of post-its being < 20 for 0.9 THz and < 10 for 1.0 THz, respectively, because the responsivity for lower frequencies is higher (due to the bow-tie antenna). The saturation is more pronounced at 0.9 THz since it is closer to the responsivity peak where the saturation is most dominant [42]. The estimated field strength in air of unattenuated radiation is as high as several hundred V/cm in the focus. More specifically, one can assume 550 V/cm given a focus area of 1 mm^2, a pulse energy of 10 nJ and a pulse duration of 25 ns. This indicates that the Firefly-THz provides enough THz output power to distribute the radiation over multiple pixels for simultaneous detection [5]. In order to have an optimal imaging and spectroscopic setup, the detector is operated in the linear regime.

2.2.3 Spectroscopy

Earlier in this chapter, the tunability of the THz frequency output of the source is demonstrated with a frequency bandwith of ≈ 50 GHz [18]. As a next step, two different samples are used to illustrate the spectroscopy capabillities of the setup. Both samples are prepared from powder mulls pressed to discs with a thickness of 1.5 mm and a diameter of 2 cm. One sample is 100% potassium bromide (KBr) while the other has 10% weight of para-aminobenzoic acid (PABA) added to the potassium bromide matrix. Figure 2.9 shows the THz transmission spectra measured by the GaN detector from 0.7 to 0.95 THz of both, the pellet with 10% PABA content and the pure KBr pellet [43]. For each point in either spectrum, the digital oscilloscope averages over 128 THz pulses and sends the resulting time trace to the computer where the maximum value is determined and stored with the corresponding frequency. PABA/KBr and KBr spectra are plotted as

[4] Reprinted by permission from Springer Nature: Springer JIMT, "Imaging and Spectroscopic Sensing with Low-Repetition-Rate Terahertz Pulses and GaN TeraFET Detectors", Daniel Voß et al., 2018

[5] During the time of this study, a five detector line array was implemented and used to take a THz picture of a cell phone which can be seen in figure A.2.

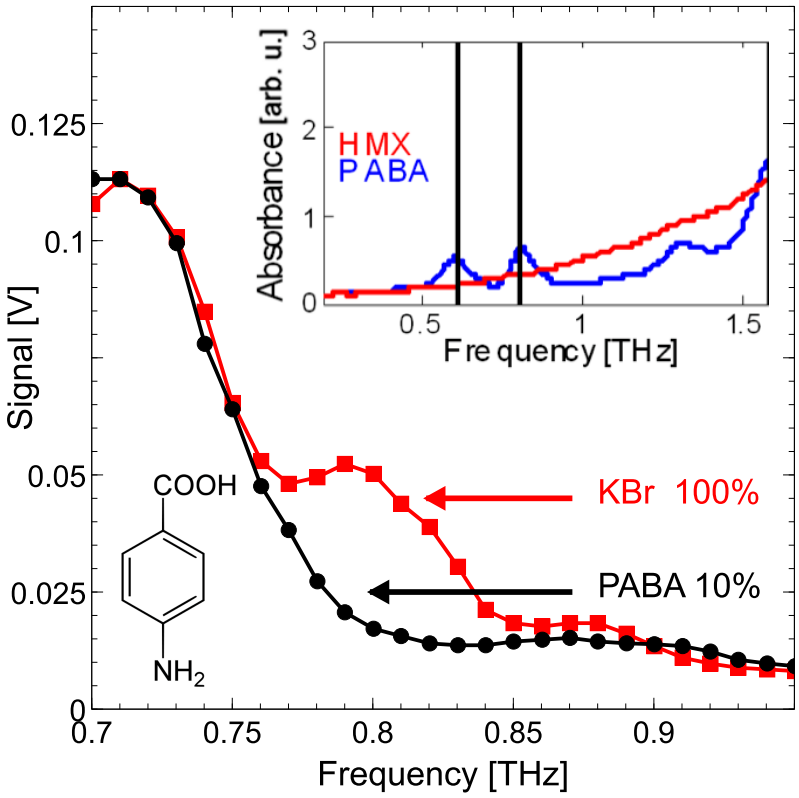

Figure 2.9: Transmission spectra of a KBr pellet (red squares and curve) and with 10% weight added PABA (black dots and curve) from 0.7 to 0.95 THz. The inset shows a published spectrum from Ref. [44]. The second inset on the bottom left shows the structural formula of a PABA (4-aminobenzoic acid) molecule.[6]

they are recorded without any normalisation to show the decrease of the signal to higher frequencies where both spectra should be featureless. They do show a clear divergence at 0.8 THz where PABA has an absorption line (see insert of Fig. 2.9). The decrease of the THz signal in both spectra towards higher frequencies can be explained by the general decay of the measured signal due to the detector responsivity itself (see Fig. 2.7a). This shows that the system itself is capable of spectroscopy applications.

[6]Reprinted by permission from Springer Nature: Springer JIMT, "Imaging and Spectroscopic Sensing with Low-Repetition-Rate Terahertz Pulses and GaN TeraFET Detectors", Daniel Voß et al., 2018

2.2.4 Imaging

Utilising the setup presented in figure 2.1, a step-scan image can be created where the transmission of each point of the sample is measured. Figure 2.10 shows such a step-scan image of a printed circuit board object. It is chosen because it's transparent holes and opaque rest have a high contrast. The top part is an optical image of the PCB next to a ruler to give an idea of it's dimensions. The images in the center and the bottom are two examples of a step-scan image generated from a simple shadow configuration where no other optical elements are required. In both cases, the chosen frequency is 0.8 THz, the pixel pitch is 0.25 mm and the covered area is 50×25 mm^2 (200×100 pixels). Considering this, both images are oversampled since the wavelength equals 0.375 mm. At each position of the center image, only one pulse is transmitted to the computer where the maximum value corresponds directly to the shown pixel colour. In comparison, the pixels of the bottom image are the maximum of 64 averaged time trace pulses. Both images show the same features of the object. The holes in the second row are clearly distinguishable and have a diameter and pitch of 1.2 mm and 6 mm, respectively. The bottom row holes with a diameter of 1.0 mm and a pitch of 2.5 mm, however, are not resolved in either picture. This is not surprising, since for 0.8 THz, the Rayleigh criterion is estimated to be 0.84 mm. Also astigmatism caused by non-spherical components lead to a lower resolution than the theory would predict.

The scan of the center image has no pulse integration resulting in a higher granularity. This can be traced back to the relatively high pulse to pulse fluctuation resulting in a low SNR mentioned earlier (see section 2.2.1). Splitting a part of the radiation to use that as a reference could improve the SNR with the drawback of sacrificing beam power. Attempts to refer the detected signal of the bow-tie antenna with the optical output of the Firefly-THz measured by a photo diode (see Fig. 2.6) to improve the SNR show no success. Unfortunately, only a small range of the spectrum around 0.8 THz shows a high correlation with the measured THz signal which makes referencing impractical. The next section takes up this finding and discusses a possible reason why it could be challenging as well as other noise sources influencing the measurement.

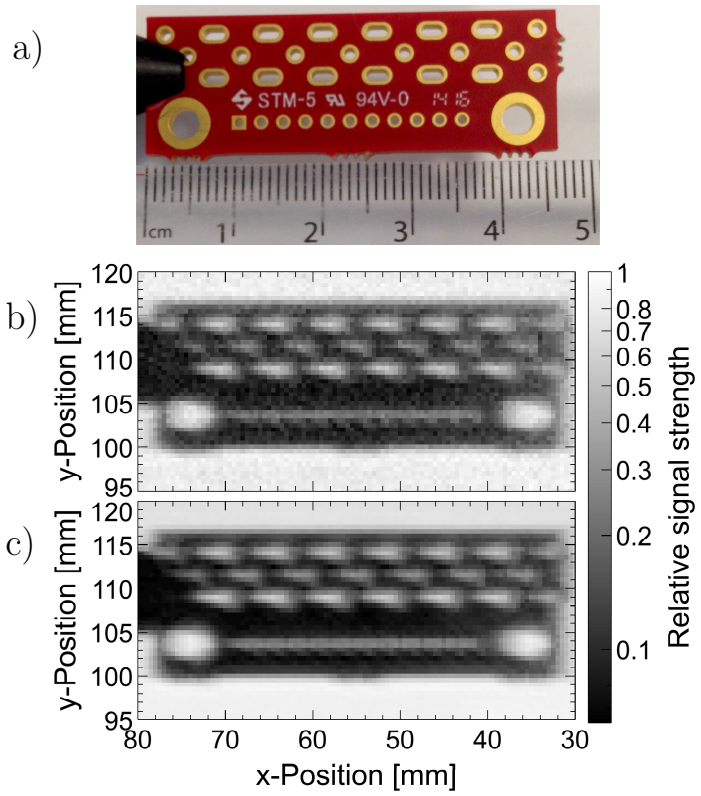

Figure 2.10: a) Photograph of the imaging test object, a metallic printed circuit board. b) Image taken at 0.8 THz with a single pulse per pixel. c) Image taken at 0.8 THz with each pixel averaged over 64 pulses.[7]

2.3 Noise origins

In order to take meaningful data, one has to consider two noise sources or influences to minimise their effect on the measurements. First discussed is the source, which is the most prominent and essential to suppress, namely the earlier mentioned Q-switch noise which is an accompanying effect of the THz generation of this source. The second disturbance is more subtle but also should not be neglected. Especially regarding the efforts of increasing the SNR through correlation of THz signal and pump or idler signal, the side effects of the optical parametric oscillator play a major role.

[7]Reprinted by permission from Springer Nature: Springer JIMT, "Imaging and Spectroscopic Sensing with Low-Repetition-Rate Terahertz Pulses and GaN TeraFET Detectors", Daniel Voß et al., 2018

2.3.1 High voltage quality switch

The THz source "Firefly-THz" is based on an OPO process where the non-linear lithium niobate crystal is placed inside the cavity of a Q-switched Nd:YAG laser (see section 2.1). The Q-switch, however, is operated with a very high voltage leading to strong electro magnetic fields in the presence of the operating system. Every wire could act as an antenna for this radiation. Since the switching process in the laser occurs to the same time as the THz generation, one cannot separate these two peaks in time. In fact, the picked up Q-switch noise could completely cloak the amplified THz signal coming from the detector. To tackle this issue, one has to keep all wires as short as possible. Especially those going towards the detector and amplifier, since noise at the input of the amplifier is amplified. Therefore, every connection including the detector and amplifier are revised. First of all, the gate voltage supply for the detector is changed to be a battery with potentiometer (for adjustable voltage between 0 and -3 V) directly connected to the input of the gate voltage at the detector box (see Fig. 2.4a). Secondly, the metal housing of the detector as well as housing the amplifier circuit improves the situation. Using batteries as the power supply for the amplifier circuit and including those in the housing brought down the Q-switch noise to a level where the DR is > 300 for lower frequencies (see Fig. 2.7).

2.3.2 Parasitic side effects in the optical parametric oscillator

By correlating not only the maximum but each value of the THz signal time trace to the maximum of the IR signal, a new time trace is obtained. Figure 2.11 shows such a correlation against time for frequencies between 0.7 and 1.4 THz. There is a high correlation observable between 0.7 and 0.9 THz at 40 ns after the trigger point. Those frequencies are at the lower end of the frequency tuning spectrum of the "Firefly-THz" (see Fig. 2.7a). Interestingly, the correlation strength is reduced and oscillates for higher frequencies where the THz output power of the source is increased.

The non-linear process which occurs in the lithium niobate crystal is well understood. However, it is also known that this process often induces some unwanted, hard to control

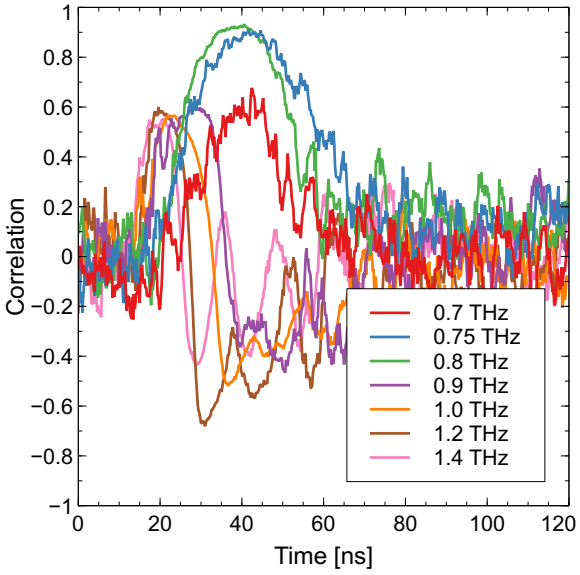

Figure 2.11: The correlation for different frequencies between 0.7 and 1.4 THz at each time position of the THz signal and the maximum of the photo diode output.

side effects which might lead to creation of radiation with other than the desired frequency underlying the main frequency [45, 46]. Especially in the range where more beam power is available, an IR photon is down converted multiple times to generate multiple THz photons from one IR photon. Even though this increases the efficiency of the source and enhances the THz output power, a reduced correlation between THz signal and IR signal is measured. Figure 2.12 shows the spectra from the pump and signal output of the Firefly-THz measured with a spectrum analyser with the THz output frequency set to 0.9 THz. Between the maximum of the pump spectrum and signal spectrum are 3.44 nm difference in wavelength which corresponds to a frequency difference and therefore output frequency of 0.897 THz. A second peak in the pump spectrum is visible, exactly two times the wavelength difference between signal and pump maximum value. This indicates that a cascade process takes place at 0.9 THz already.

Also, internal reflections may cause some frequencies to be unintentionally coupled out. At one side of the output window of the Firefly-THz, a spot through an IR viewer can be seen for some frequencies in the tuning range of the Firefly-THz. The IR radiation only marginally overlaps with the THz radiation and is therefore externally blocked (see Fig. A.1).

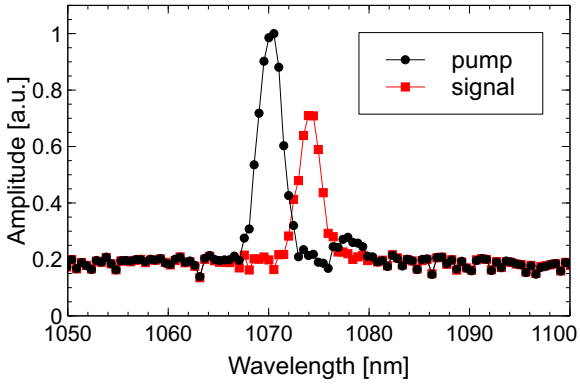

Figure 2.12: The figure shows the pump and idler output intensity of the Firefly-THz recorded by the spectrum analyser with a THz output frequency set to be 0.9 THz.

2.4 Discussion and conclusions

Imaging and spectroscopy is demonstrated using a Q-switched OPO THz source together with a TeraFET detector based on GaN/AlGaN technology for the first time. This technology proves to be more robust than CMOS based detectors, enabling its operation under the influence of high electric fields – THz signal or otherwise. By enclosing the detector in a metal box and providing the gate voltage through a battery and keeping all cables as short as possible, the setup reaches a SNR of > 20 and DR of > 300 at 0.8 THz for single pulse detection. To quantify the spectroscopy ability of the Firefly-THz, sample pallets of 10% para-aminobenzoic acid (PABA) and 90% potassium bromide (KBr) were produced and measured in a transmission configuration. The characteristic absorption dip of PABA at 0.8 THz in the spectrum is identified by direct comparison with the pure featureless KBr reference sample. Even though the tuning range of the Firefly-THz is quite wide, one should be able to cover the hole range of this THz source using two detectors with sufficient sensitivity, when their antennas are designed appropiately [47]. The source provides enough THz power to spread the signal over a larger area to enable multi-pixel detection or even a THz camera. GaN/AlGaN are produced in a stepper process. This process is cheaper for small number production whearese the mass production in the standard process makes CMOS cheaper for high quantities [35, 48]. TeraFETs have a fast intrinsic speed which enables single pulse detection making fast imaging a natural application of

this setup. Even without averaging, the achieved resolution is approximately 1.2 mm with a high contrast object. After all investigations, it is still not clear where exactly the pulse-to-pulse fluctuations come from. A possible explanation is multi down conversion of optical photons which lead to an inconsistent number of THz photons per photon of the pump beam [45, 46]. Due to that inconsistency, there is only a weak correlation between THz signal and IR-signal or pump signal, which makes a pulse wise referencing challenging. Another option is to split the THz signal and reference the probing signal by its unaltered counter part. Although this is not a preferred solution, an increase in SNR of one order of magnitude could be obtained using referencing, making this setup even more interesting for potential applications.

3 Fourier optics simulations

In conventional imaging, the phase of the source is not of general interest since the image is solely created by the intensity. In Fourier optics, however, the objects are not directly observed. Instead of placing the detector in the image plane of the focussing lens, the field is measured with the amplitude and phase in the focus plane of a lens. It is also called the Fourier plane, because the field in the focus plane is the Fourier transform of the object with – in general – an additional phase factor (see section 3.2). To determine the input in front of the focussing lens, numerical calculations are needed to back propagate the measured field. The phase, contains information of the electromagnetic field and as such plays a key role in Fourier optics. In the following chapter, the basics of Fourier transformation are presented and formulas are derived to theoretically investigate Fourier optics. The implementation of the formulas is considered in more detail, before a closer look is taken on the role of the intensity and phase. The chapter finishes with further simulation results focussing on experimental boundary conditions.

3.1 Fourier analysis

Waves and vibrations are ubiquitous phenomenons in physics. Most fields in physical science have to consider them in various manifestations. Either as a carrier of required information in interferometry, spectroscopy, electro engineering, optics, acoustics etc. or an unwanted effect in mechanical movements, electronics etc. which adds noise and/or instability to the system. In all these fields, the vibrations or *signals*, regardless if it is wanted or not, generally consist of a spectrum of frequencies. In fact, any signal can be associated with a superposition of interfering sine waves. The Fourier analysis

utilises the Fourier transform in order to determine those different frequencies and their amplitude. In the following section, the Fourier transform is briefly introduced, continuing with the Discrete Fourier transform (**DFT**) and the related, more efficient Fast Fourier transform (**FFT**), before the Fourier transform is extended to two dimensions. The Fresnel approximation is derived from the Huygens-Fresnel principle leading together with the phase transform of a lens to the formula used throughout the Fourier optics simulation and the Fourier THz imaging chapter.

3.1.1 Fourier transform

This work follows the definition of [49–51] were the Fourier transform of a general complex function $g(x)$ in space domain x, represented by $\mathcal{F}\{g(x)\}$, is defined as

$$\mathcal{F}\{g(x)\} = \int_{-\infty}^{+\infty} g(x)e^{-i2\pi xu}\mathrm{d}x = \tilde{g}(u), \tag{3.1}$$

where u is the spacial frequency. The inverse Fourier transformation of a function $\tilde{g}(u)$, is correspondingly represented by $\mathcal{F}^{-1}\{\tilde{g}(u)\}$,

$$\mathcal{F}^{-1}\{\tilde{g}(u)\} = \int_{-\infty}^{+\infty} \tilde{g}(u)e^{i2\pi xu}\mathrm{d}u = g(x). \tag{3.2}$$

For this definition, the Fourier transformation and the inverse Fourier transformation are very similar and differ only by the sign of the exponent in the integral. The existence of the Fourier transform of $g(x)$ is determined by the conditions [50],

1. The integral of $|g(x)|$ is finite on the interval from $-\infty$ to $+\infty$
2. The number of minima, maxima and discontinuities is finite in any finite interval
3. All discontinuities have to be finite

Bracewell states that the Fourier transform of a function exists if the function is physically possible [50], which is sufficient for our purpose. Sometimes, it is practical to use a non

physical function to approximate a real situation. For example the Dirac δ function is used to represent a very short pulse, even though it does not fulfil condition 3. since its discontinuity is not finite.

Given that the Fourier transform exists and $\tilde{g}(u)$, $g(x)$ are a Fourier pair, its most important properties are listed below [50].

1. **Fourier integral theorem**

   By performing successive the Fourier transformation and the inverse Fourier transformation, one obtains the original function $g(x)$,

$$g(x) = \mathcal{F}^{-1}\{\mathcal{F}\{g\}\} = \int_{-\infty}^{+\infty} \left[\int_{-\infty}^{+\infty} g(x) e^{-i2\pi xu} \mathrm{d}x \right] e^{i2\pi xu} \mathrm{d}u \, . \tag{3.3}$$

2. **Linearity theorem**

   The transformation of a weighted sum of two functions g and h can be calculated by the weighted sum of the individual transformed functions,

$$\mathcal{F}\{\alpha g(x) + \beta h(x)\} = \alpha \mathcal{F}\{g(x)\} + \beta \mathcal{F}\{h(x)\}. \tag{3.4}$$

3. **Similarity theorem**

   A scaling in the space domain results in an inversely proportional scaling in the frequency domain as well as a change in the overall amplitude of the spectrum,

$$\mathcal{F}\{g(ax)\} = \frac{1}{|a|} \tilde{g}\left(\frac{u}{a}\right). \tag{3.5}$$

4. **Shift theorem**

   A displacement of a in the space domain results in a linear phase shift $\exp[-i2\pi au]$ in the frequency domain,

$$\mathcal{F}\{g(x-a)\} = \tilde{g}\{u\} \exp[-i2\pi au]. \tag{3.6}$$

5. **Rayleigh's theorem**

   The absolute value of $g(x)$ squared corresponds to the energy density, hence the integral over the complete space corresponds to the total energy in space domain. Since the energy must be conserved, it is equal to the energy in the frequency domain,

$$\int_{-\infty}^{+\infty} |g(x)|^2 \mathrm{d}x = \int_{-\infty}^{+\infty} |\tilde{g}(u)|^2 \mathrm{d}u \,. \tag{3.7}$$

6. **Convolution theorem**

   Let $\tilde{h}(u)$ be the Fourier transform of another complex function $h(x)$, then the convolution of g and h in space domain equals the inverse Fourier transform of the product of $\tilde{g}$ and $\tilde{h}$ in frequency domain,

$$\int_{-\infty}^{+\infty} g(\xi)h(x-\xi)\mathrm{d}\xi = \mathcal{F}^{-1}\left\{\tilde{g}(u)\tilde{h}(u)\right\}. \tag{3.8}$$

Fourier transforms can also be used to determine the frequency components of a signal. Figure 3.1a shows three sine waves with the amplitudes $0.8, 0.3, 0.5$ and frequencies $0.25, 0.5, 1$, respectively. The sum of those sine waves as well as the constant offset of 0.5 result in a superposition which is shown in Fig. 3.1b. By Fourier transforming the superposition[1], a frequency spectrum is obtained shown in Fig. 3.1c. Note that the graph is mirrored with the lower frequencies located in the center. Also, each peak's hight corresponds to the amplitude of the sine wave with the respective frequency.

Most functions are made up by a continuous number of frequencies which results in a new function in the Fourier spectrum. Figure 3.2 shows two example Fourier pairs. On the top left, (Fig. 3.2a) one can see a 'top-hat' or *rect* function,

$$h(x) = \mathrm{rect}_w(x) = \begin{cases} 1, & \text{if } |x| \leq w/2 \\ 0, & \text{if } |x| > w/2, \end{cases} \tag{3.9}$$

[1] A Fast Fourier transform algorithm was previously used (see chapter 3.1.3).

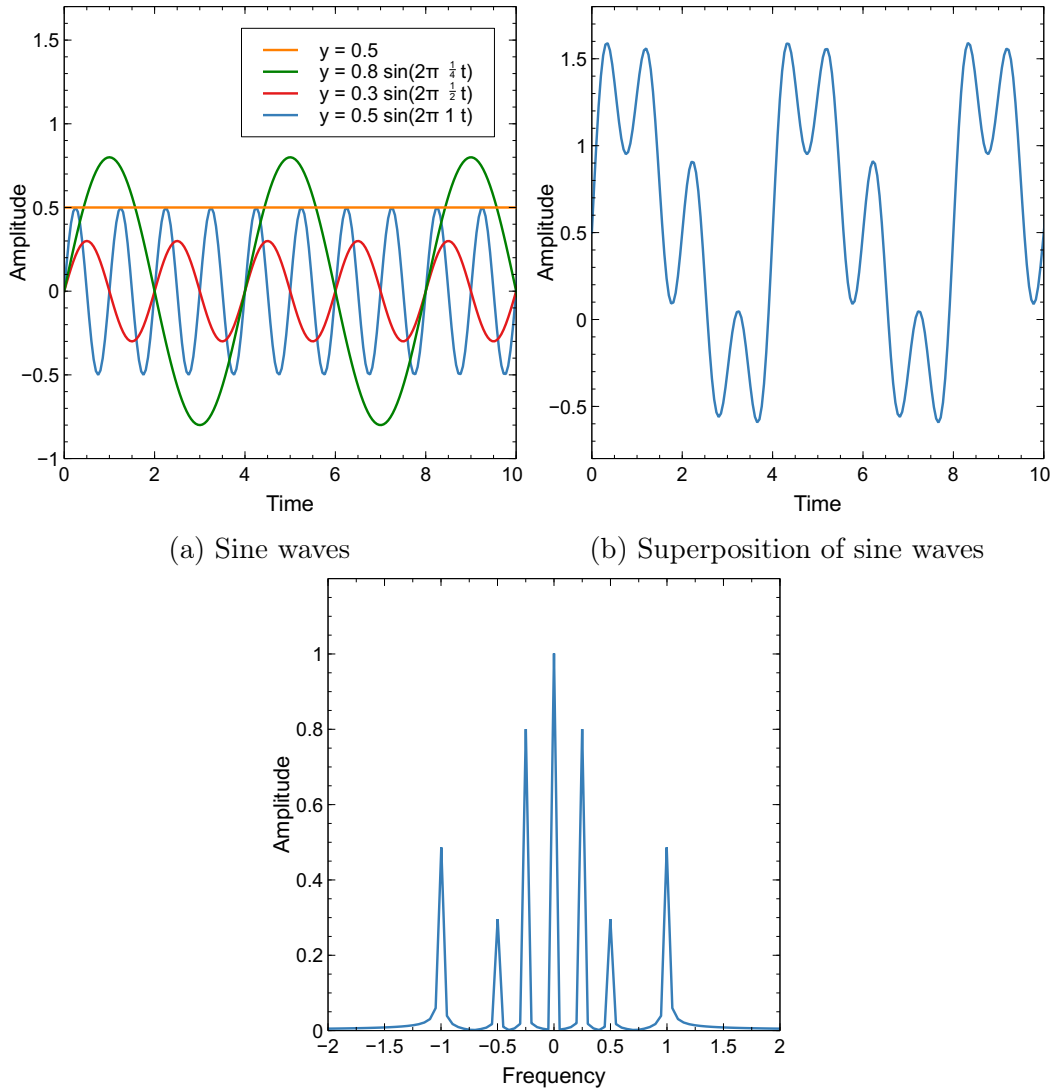

(a) Sine waves

(b) Superposition of sine waves

(c) Fourier transform of superposition

Figure 3.1: (a) Sine waves with different frequencies and amplitudes and offset. (b) Superposition of sine waves shown in figure (a). (c) Fourier transform of the superposition.

with height 1 and width w. It's Fourier transform is a *sinc* function

$$\tilde{h}(u) = w\,\mathrm{sinc}(\pi u w) = w\frac{\sin(\pi u w)}{\pi u w} \tag{3.10}$$

which is plotted underneath with zero points at $|u| = 1/w,\ 2/w,\ 3/w\ldots$. This can be

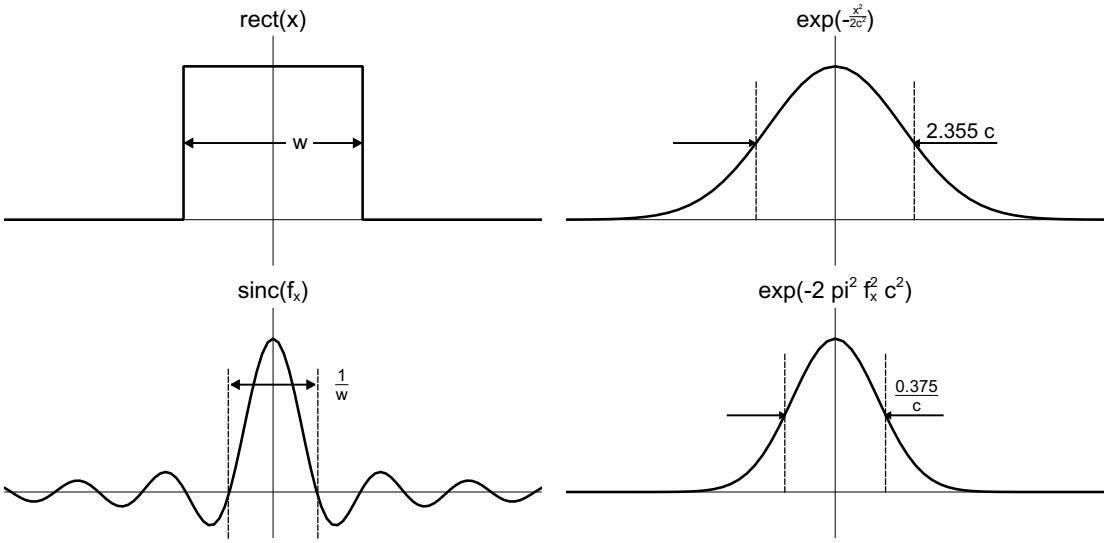

(a) Rectangle and sinc function pair (b) Gaussian and Fourier transform pair

Figure 3.2: (a) The rectangle function and its Fourier transform, a sinc function. (b) A gaussian function with its Fourier transform, a gaussian function.

found by Fourier transforming $h(x)$ [52],

$$\begin{aligned}\tilde{h}(u) &= \int_{-\infty}^{+\infty} \mathsf{rect}_w(x) e^{-i2\pi xu} \mathsf{d}u = \int_{-w/2}^{+w/2} e^{-i2\pi xu} \mathsf{d}u \\ &= \frac{-1}{i2\pi u}\left[e^{-i\pi wu} - e^{i\pi wu}\right] \\ &= \frac{1}{\pi u}\frac{e^{i\pi wu} - e^{-i\pi wu}}{2i} = w\,\frac{\sin(\pi wu)}{w\pi u} \\ &= w\,\mathsf{sinc}(\pi wu)\;, \end{aligned} \tag{3.11}$$

where the definition $\mathsf{sinc}(x) = \frac{\sin(x)}{x}$ is used in the last step. The top right shows a Gaussian function (Fig.3.2b) defined as,

$$g(x) = a\exp\left(\frac{-x^2}{2c^2}\right). \tag{3.12}$$

Its Fourier transform is also a Gaussian function and can be obtained by Fourier transformation (similar to the Fourier transform of Eq. 3.11),

$$\tilde{g}(u) = a\sqrt{2\pi c^2}\exp\left(-2\pi^2 c^2 u^2\right)\;. \tag{3.13}$$

The full width at half maximum (**FWHM**) is obtained by solving the equation for the position x_{fwhm} for which the half height h_0 is reached,

$$\begin{aligned} \frac{1}{2}h_0 &= a\exp\left(\frac{-x_{\mathsf{fwhm}}^2}{2c^2}\right) \\ \Rightarrow x_{\mathsf{fwhm}} &= \pm\sqrt{2\ln(2)}c\,, \end{aligned} \tag{3.14}$$

where $h_0 = a$ which results in a FWHM of $w = 2\sqrt{2\ln(2)}c \approx 2.355c$. Performing the equivalent steps for the Fourier transformed function $\tilde{g}(u)$, the FWHM is calculate with $w = \frac{\sqrt{2\ln(2)}}{\pi c} \approx \frac{0.375}{c}$. Even though the Fourier pair are two Gaussian functions, the FWHM of the Fourier transform is antiproportional to the FWHM of $g(x)$ and has a different amplitude. The factor c appears as a scaling factor inside of the exponential function as well as a factor in the amplitude which is just what is expected regarding the similarity property of the Fourier transform (see Eq. 3.5).

Another common function to consider is the Dirac delta-function $\delta(x)$, defined as

$$\begin{aligned} \delta(x) &= \begin{cases} \infty, & \text{if } x = 0 \\ 0, & \text{if } x \neq 0 \end{cases} \\ 1 &= \int_{-\infty}^{+\infty} \delta(x)\mathsf{d}(x). \end{aligned} \tag{3.15}$$

As mentioned earlier, this function does not fulfil the finite discontinuities criteria but still has a Fourier transform. It can be regarded as a Gaussian function which gets narrower and higher with its Fourier transform being also a Gaussian function with amplitude one getting wider and wider with the limit being one for all frequencies,

$$\mathcal{F}\left\{\delta(x)\right\} = 1. \tag{3.16}$$

The next section will make use of the called Dirac comb Ш,

$$\text{Ш}_a(x) = \sum_{n=-\infty}^{\infty} \delta(x - na), \tag{3.17}$$

where a represents the spacing between the Dirac delta-functions. As can be seen from the definition, Ш is a set of equally spaced Dirac functions with its Fourier transform being also a Dirac comb with spacing $\frac{1}{a}$ and equal height $\frac{1}{a}$,

$$\mathcal{F}\{\text{Ш}_a\} = \frac{1}{a}\text{Ш}_{\frac{1}{a}}(u). \tag{3.18}$$

3.1.2 Discrete Fourier transform

The Fourier transform can be analytically performed by integration. However, in practice the data most often is presented as a set of discrete points which require a separate integration for each point. With such data sets, the DFT is needed and defined as [52],

$$\mathcal{F}_{\mathsf{D}}\{g(x_k)\} = \sum_{k=0}^{N-1} g(x_k)e^{-i2\pi x_k u_k/N} = \tilde{g}(u_k) \qquad k = 0, 1, 2, ..., N-1. \tag{3.19}$$

This is very similar to the familiar Fourier transform (see Eq. 3.1) with continuous space variable x and spacial frequency u changed to discrete positions x_k and spacial frequencies u_k, as well as the integral being replaced by a summation over discrete positions. It can be shown that by multiplying the continuous function $g(x)$ by a Dirac comb, the Fourier transform of $g(x)$ yields the DFT from above [52],

$$\int_{-\infty}^{+\infty} \sum_{k=0}^{N-1} \delta(x - ak)g(x)e^{-i2\pi xu}\mathsf{d}x = \mathcal{F}_{\mathsf{D}}\{g(x_k)\}. \tag{3.20}$$

The integral over x collapses with the Dirac function and leaves the sum over $N-1$ discrete values. Note that a finite Dirac comb with N Dirac delta functions replaced the infinite Dirac comb. This is sufficient if $g(x)$ is negligible outside of the range $-a/2$ to $(N-1/2)a$. The inverse discrete Fourier transform (**iDFT**) is stated by,

$$\mathcal{F}_{\mathsf{D}}^{-1}\{\tilde{g}(u_k)\} = \frac{1}{N}\sum_{k=0}^{N-1} \tilde{g}(u_k)e^{i2\pi x_k u_k/N} = g(x_k) \qquad k = 1, 2, 3, ..., N-1, \tag{3.21}$$

so that DFT and iDFT have the same properties as Fourier transform and inverse Fourier transform.

3.1.3 Fast Fourier transform

This procedure becomes time consuming for large data sets. However, with the discovery of the so called Fast Fourier transformation (**FFT**), the number of calculations needed to perform a Fourier transform decreases significantly [53]. Nowadays, this algorithm can be performed very quickly and is used in various applications [52].

By defining the parameter,

$$W = e^{-i2\pi/N}, \tag{3.22}$$

the DFT of equation 3.19 is written as matrix multiplication,

$$\begin{bmatrix} G(0) \\ G(1) \\ G(2) \\ \vdots \\ G(N-1) \end{bmatrix} = \begin{bmatrix} W^0 & W^0 & W^0 & \cdots & W^0 \\ W^0 & W^1 & W^2 & \cdots & W^{(N-1)} \\ W^0 & W^2 & W^4 & \cdots & W^{2(N-1)} \\ \vdots & \vdots & \vdots & \vdots & \vdots \\ W^0 & W^{(N-1)} & W^{2(N-1)} & \cdots & W^{(N-1)^2} \end{bmatrix} \begin{bmatrix} g(0) \\ g(1) \\ g(2) \\ \vdots \\ g(N-1) \end{bmatrix}. \tag{3.23}$$

To evaluate this matrix multiplication, N^2 multiplications and N additions are performed, summing up to $N^2 + N$ operations for the DFT. The FFT exploits the obvious identity $W^0 = 1$ and the cyclic nature of W, leading to further simplifications and computational savings. Many books can be consulted for the detailed derivation of the FFT algorithm (eg. [52, 54]). The FFT algorithm reduces the number of needed calculations to $N\ln(N)$ multiplications and N additions, resulting in a total number of $N\ln(N)+N$ computations to perform with the FFT algorithm. For large enough N, one compares the DFT and FFT with $\sim N^2$ and $\sim N\ln(N)$ calculations, respectively. Taking an example of a vector with 10^6 entries leading to $\sim 10^7$ instead of $\sim 10^{12}$ calculations, being the equivalent of a few milliseconds instead of several minutes computation time with modern computers [52]. As a result, the FFT is very practicable to use for a wide span of applications.

3.1.4 Fourier analysis in two dimensions

The previously discussed Fourier transform and FFT can be extended for functions with multiple independent variables, where all properties and methods are still valid. Here and in the rest of this work, the consideration is limited to a function $g(x, y)$ with two independent variables x, y. The Fourier transform of $g(x, y)$, represented by $\mathcal{F}\{g(x, y)\}$, is written as an integration over two independent variables,

$$\mathcal{F}\{g(x,y)\} = \iint_{-\infty}^{+\infty} g(x,y)e^{-i2\pi(xu+yv)}\mathrm{d}x\mathrm{d}y = \tilde{g}(u,v), \tag{3.24}$$

where u and v are the special frequencies. By comparing the one and the two dimensional Fourier transform (Eq. 3.1, Eq. 3.24), one will notice the additional factor $e^{-i2\pi yv}$ in the integral. The two dimensional inverse Fourier transformation of a function $\tilde{g}(u, v)$, represented by $\mathcal{F}^{-1}\{\tilde{g}(u, v)\}$, is again very similar to the two dimensional Fourier transform but for the sign of the exponent and has analogical to the two dimensional Fourier transform an additional factor $e^{i2\pi yv}$,

$$\mathcal{F}^{-1}\{\tilde{g}(u,v)\} = \iint_{-\infty}^{+\infty} \tilde{g}(u,v)e^{i2\pi(xu+yv)}\mathrm{d}u\mathrm{d}v = g(x,y). \tag{3.25}$$

The Fourier transform is applied now in future to a function with two independent variables, the two dimensional Fourier and inverse Fourier transform are used and therefore will be referred to as Fourier and inverse Fourier transform, respectively.

3.1.5 Fresnel- and Fraunhofer Diffraction

Whenever a wave hits an object (e.g. an aperture) on its path, the wave bends and can be observed in the geometrical shadow of the object. This phenomenon is known as diffraction. Below, the Huygen- Fresnel- principle is introduced before the Fresnel diffraction integral is derived whit the Fraunhofer diffraction as a limit approximation. For simplicity, monochromatic light is assumed through all considerations.

Huygen-Fresnel principle

While the effect of diffraction has been long known, it was Huygens who first gave an intuitively accessible explanation by treating each point of the wavefront as a new "secondary" point source of a new elementary wave [49, 55]. In an optical isotropic medium, the envelope of these spherical elementary wavefronts form the new primary wave (see Figure 3.3a) [56].

At this point it is noteworthy that Huygens principle can also explain the relationship between the angle of incidence, reflected and refracted wavefront at a boundary surface of two materials with different refraction indices n [57]. By assuming $n_1 < n_2$, Figure 3.3b shows the refraction of a wave at an interface between two optical isotropic media with refraction index n_1 and n_2, respectively. The wave front hits the interface at an angle α with the propagation speed of the wave in medium one and two being $c_1 = c_0/n_1$ and $c_2 = c_0/n_2$, respectively. An elementary wave is created at point A where the wave front hits the interface which takes the time $\Delta t = \overline{AB}/c_2$ to travel the distance to point B. In the same time $\Delta t = \overline{DC}/c_1$, the wave travels from point D to the point C. The tangent of the spherical wave originated at point A through the point C creates a new wave front. With distances $\overline{AB}$ and $\overline{DC}$ one finds for each triangle ACD and ABC

$$\overline{AC} = \frac{\overline{DC}}{\sin\ \alpha} \qquad \text{and} \qquad \overline{AC} = \frac{\overline{AB}}{\sin\ \beta}\ . \tag{3.26}$$

With the previous observation this leads to

$$\frac{\sin\ \alpha}{\sin\ \beta} = \frac{\overline{DC}}{\overline{AB}} = \frac{c_1}{c_2} = \frac{n_2}{n_1}\ , \tag{3.27}$$

what is recognised as **Snell's law** for refraction at an interface [57]. The observation of reflection is analogue, resulting in a reflection angle α' being the same as the incident angle α.

The Rayleigh-Sommerfeld solution predicts for $r_{01} \gg \lambda$ that the Huygen-Fresnel prin-

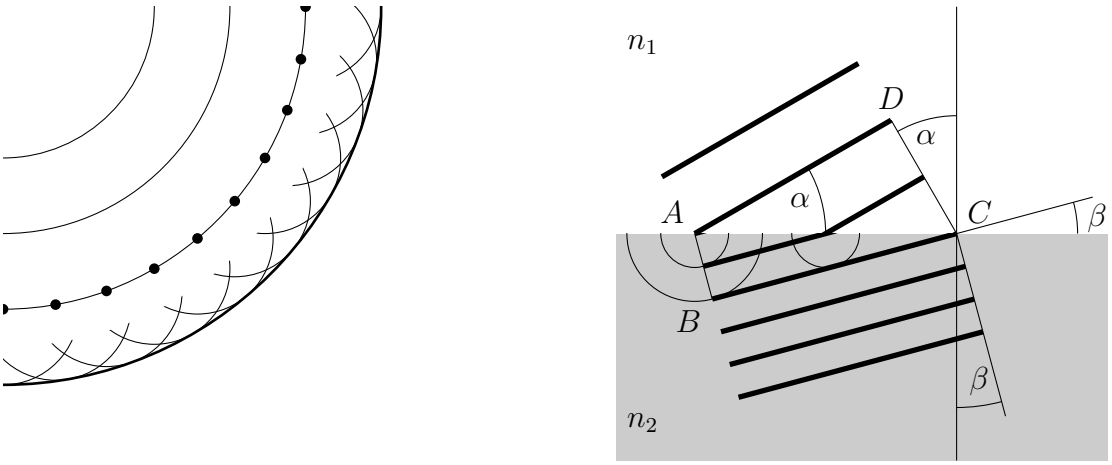

(a) Huygens principle (b) Refraction at an interface

Figure 3.3: (a) The new wave front can be displayed by the superposition of secondary wavelets. (b) Refraction at an interface shown with Huygens principle.

ciple can be expressed mathematically by

$$U(P_0) = \frac{i}{\lambda} \iint_{\Sigma} U(P_l) \frac{\exp(-ikr_{01})}{r_{01}} \cos(\theta)\, \mathrm{d}s, \tag{3.28}$$

where λ is the wavelength, k is the wave vector equal to $2\pi/\lambda$, θ is the angle between $\vec{n}$ (the normal vector on the aperture plane) and $\vec{r_{01}}$ [49]. The field $U(P_0)$ at P_0 results by superimposing the spherical waves $\exp(-ikr_{01})/r_{01}$ of secondary sources with amplitude $U(P_1)$ in every point within the aperture Σ. r_{01} simply states the absolute value of the vector $\vec{r_{01}}$ from the point of observation P_0 to point P_1 in the aperture. For the in depth derivation of equation (3.28) the interested reader is referred to [49]. Please note that hereafter the convention is used that the field $E(\vec{r})$ of an in z propagating wave with amplitude $A(\vec{r})$ is defined as,

$$E(\vec{r}) = A(\vec{r})e^{-ikz}. \tag{3.29}$$

Fresnel and Fraunhofer approximation

Following the steps presented in [49], further assumptions to the Fresnel-Huygens principle are made. For cartesian coordinates, the Huygens-Fresnel diffraction problem is sketched

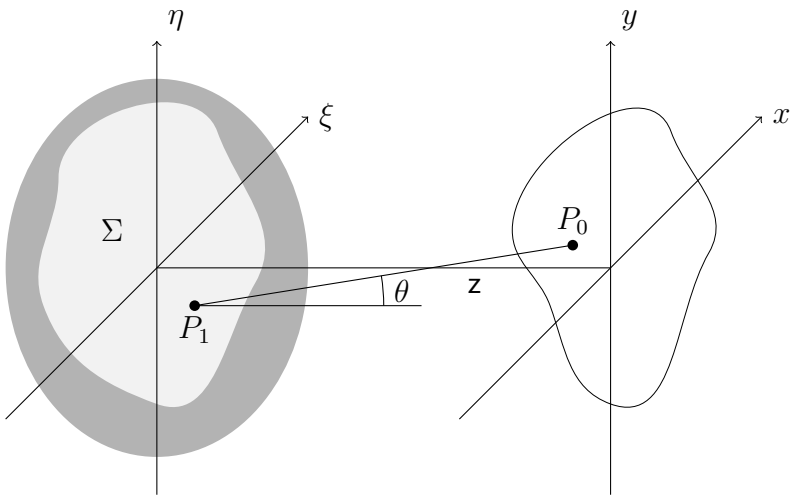

Figure 3.4: Sketch for Huygens-Fresnel diffraction problem

in figure 3.4. By regarding this figure, the cosine in equation (3.28) can be substituted by z/r_{01} yielding

$$U(P_0) = \frac{iz}{\lambda} \iint_{\Sigma} U(\xi,\eta) \frac{\exp(-ikr_{01})}{r_{01}^2} \, \mathrm{d}\xi \mathrm{d}\eta, \tag{3.30}$$

where the constant distance z was written before the integral. The absolute value of vector r_{01} can be substituted by

$$r_{01} = \sqrt{z^2 + (x-\xi)^2 + (y-\eta)^2}$$

$$= z\sqrt{1 + \left(\frac{x-\xi}{z}\right)^2 + \left(\frac{y-\eta}{z}\right)^2}, \tag{3.31}$$

where ξ and η are the coordinates in the plane of the aperture where x and y are the coordinates in the plane of observation. The square root can be rewritten as a binomial series using

$$f(a) = \sqrt{1+a} = \sum_{k=0}^{\infty} \frac{f^{(k)}(a=0)}{k!} a^k \approx 1 + \frac{1}{2}a + \mathcal{O}(a^2), \tag{3.32}$$

with $a < 1$ where terms with higher order in a are dropped. By identifying the second and third term of equation (3.31) as a in the previous binomial series, r_{01} is approximated

by

$$r_{01} \approx z \left[1 + \frac{1}{2} \left(\frac{x-\xi}{z} \right)^2 + \frac{1}{2} \left(\frac{y-\eta}{z} \right)^2 \right]. \tag{3.33}$$

This is valid for angles $\theta < 45°$ because by rewriting previous restriction $a < 1$, one obtains

$$1 < a = \left(\frac{x'}{z} \right)^2 + \left(\frac{y'}{z} \right)^2 = \left(\frac{r_{01}}{z} \right)^2 \underbrace{\left(\sin^2\phi + \cos^2\phi \right)}_{=1} = \tan^2\theta, \tag{3.34}$$

with the new coordinates $x' = x - \xi$, $y' = y - \eta$ in the x, y plane with their origin at the orthogonal projection of P_1 and r, ϕ being the polar coordinates of point P_0. Substituting r_{01} in equation (3.30) using (3.33) where z^2 is approximated by r_{01}^2 in the denominator but all terms for r_{01} in the exponent, one gets

$$U(x,y) = \frac{ie^{-ikz}}{\lambda z} \iint_{-\infty}^{+\infty} U(\xi,\eta) \exp\left\{ -i\frac{k}{2z} \left[(x-\xi)^2 + (y-\eta)^2 \right] \right\} \mathrm{d}\xi \mathrm{d}\eta, \tag{3.35}$$

where $U(\xi,\eta)$ was redefined so it vanishes outside of the aperture and writing the constant phase factor e^{-ikz} in front of the integral. Using $r_{01} = z$ wont suffice in the exponent since an error in the phase is more critical moreover being multiplied with k [49]. By evaluating the quadratic terms in the exponent, equation (3.35) rewrites as

$$U(x,y) = \frac{ie^{-ikz}}{\lambda z} e^{-i\frac{k}{2z}\left(x^2+y^2\right)} \iint_{-\infty}^{+\infty} \left\{ U(\xi,\eta) e^{-i\frac{k}{2z}\left(\xi^2+\eta^2\right)} \right\} e^{i\frac{2\pi}{\lambda z}(x\xi+y\eta)} \mathrm{d}\xi \mathrm{d}\eta, \tag{3.36}$$

which is known as the **Fresnel diffraction integral** [49, 55]. As it can be seen in chapter 3.1.4, that it is a two dimensional Fourier transform of a complex field multiplied with a quadric phase factor [49].

The Fresnel diffraction integral can be transformed to the Fraunhofer diffraction integral by making further restrictions to the quadratic phase exponent in equation (3.36) demanding

$$z \gg \frac{k}{2} (\xi^2 + \eta^2)_{\mathrm{max}}. \tag{3.37}$$

The exponent vanishes, leaving unity as a factor over the range of integration, which then

simplifies (3.36) to the **Fraunhofer diffraction integral**,

$$U(x,y) = \frac{ie^{-ikz}}{\lambda z} e^{-i\frac{k}{2z}\left(x^2+y^2\right)} \iint_{-\infty}^{+\infty} U(\xi,\eta) e^{i\frac{2\pi}{\lambda z}(x\xi+y\eta)} \mathrm{d}\xi \mathrm{d}\eta. \tag{3.38}$$

The Fraunhofer diffraction integral is derived as a special case of the Fresnel diffraction integral. The former is an additional simplification and proves sufficient for many cases to predict experimental results. As a simple measure when to use the Fresnel diffraction integral and when the Fraunhofer diffraction integral will be sufficient, the **Fresnel number** can be defined as,

$$N_F = \frac{a^2}{\lambda z}, \tag{3.39}$$

with the radius of the aperture a, the wavelength λ and the distance z to the aperture [49]. Two regions can be distinguishes as $N_F \gg 1$ and $N_F \ll 1$. The former indicates the **near field** close to the aperture and the latter the so called **far field** further away from the aperture, while the transition regime is denoted by $N_F \approx 1$. The Fraunhofer approximation can only be applied in the far field. Assuming a plane wave with a normalised amplitude and the wave length $\lambda = 1$ mm hit a 1 mm aperture ($a = 0.5$ mm). Then Figure 3.5 shows the fields intensity behind the aperture for different distances from 0.025 mm to 2.5 mm (left side) with the corresponding Fresnel number from 10 to 0.1 (right side). For comparison, each intensity was normalised to the input plane wave's intensity and then shifted by 1 for better readability. In the near field, the intensity steeply rises and oscillates strongly within the aperture boundaries. With increasing distance z and decreasing N_F, the field does not fall as steep to both sides. The oscillations become smooth till a peak in the middle of the aperture is isolated and broadens for distances further away. Note that in the near field, field enhancement is obtained indicated by intensities greater than one. These become pronounced in the transition regime before they decline in the far field. This effect is exploited by a zone plate which focuses monochromatic light, preferably used for frequencies e.g. x-rays where lenses do not work, due to their refractive index being close to one [56].

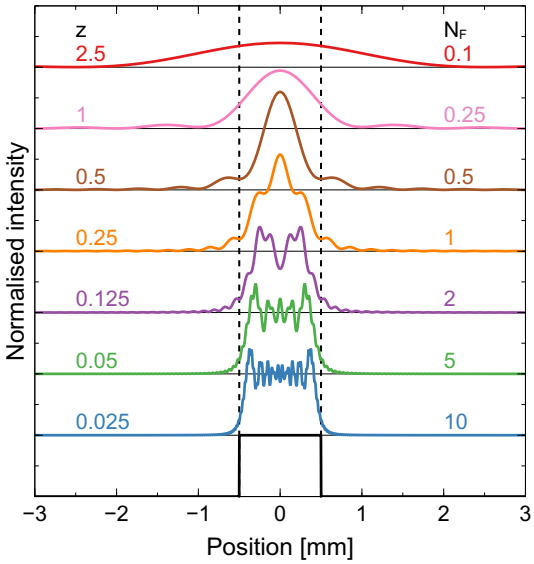

Figure 3.5: The Intensity distribution for various distances after an aperture (black).

3.2 Fourier optics

It is well known that an electromagnetic field passing through a lens is Fourier transformed at the focus plane of that lens. This is exploited in multiple applications such as filtering, optical information processing, pattern recognition ect. [49]. In the following section, the previous discussed diffraction approximation is utilised to write down the equations for calculating the light propagation through an optical system. The field of view and resolution discussion terminates this section.

3.2.1 Fourier transformation by a lens

To investigate the Fourier transform by a lens, the below observation will make use of the above derived Fresnel diffraction integral (see equation 3.36). As before, monochromatic and coherent light is assumed. An input transparency $t_0(x, y)$ is considered which will be stated hereafter as input. Firstly, the case is discussed where the input is placed directly against the lens. There, the input field is phase transformed through a thin lens and propagated to the focus. Second, the input is placed an additional distance d in front of the lens which requires the input field to be propagated a length d towards the lens.

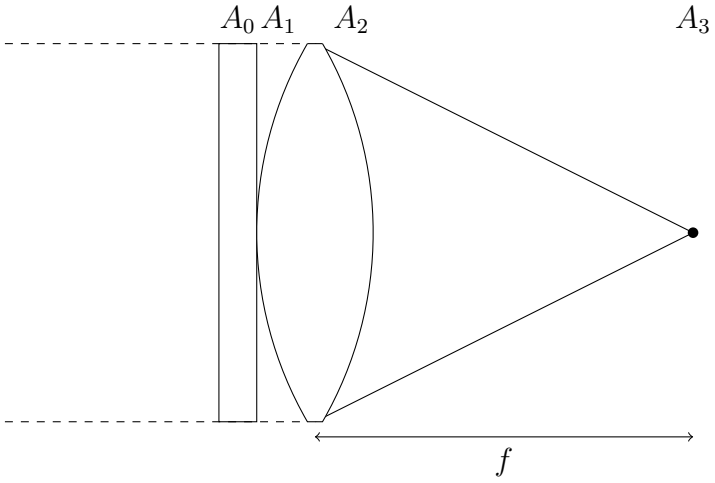

(a) Input against the lens

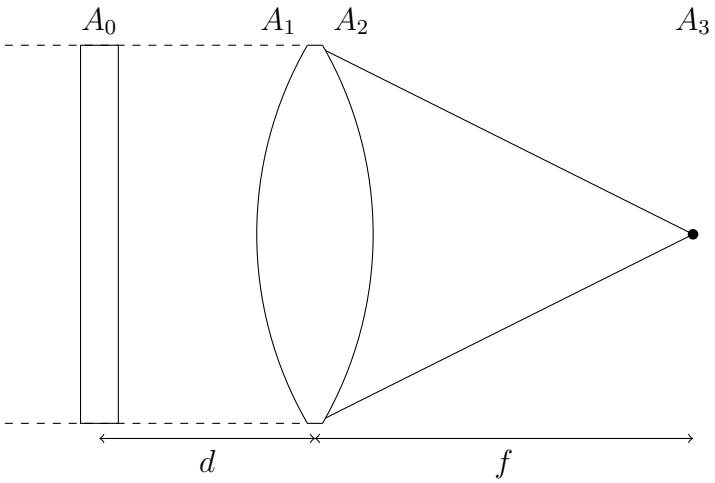

(b) Input d in front of lens

Figure 3.6: (a) The input placed directly against the lens with focus length f. (b) The input placed a distance d in front of the lens with focus length f. A_i indicates the field at the input, just before the lens, just after the lens and at the focus for $i = 0$,1,2 and 3, respectively.

Phase transformation by a lens

A lens is usually made of an optically more dense medium than the surrounding which is chosen to be air/vacuum ($n = 1$). The lens is defined to be spherically shaped with a refractive index n. A plane wave travelling through a lens with thickness $\Delta d(x, y)$ (dependent on the position of incident), experiences a phase transformation based on the phase delay t_l,

$$t_l = e^{-ik(n-1)\Delta d}, \tag{3.40}$$

where k is the wave vector $k = 2\pi/\lambda$ with the wavelength λ. By expressing the thickness Δd as a function of x and y assuming spherical surfaces and applying the paraxial approximation,

$$\sqrt{1 - \frac{x^2 + y^2}{R_i^2}} \approx 1 - \frac{x^2 + y^2}{2R_i^2}, \qquad i = 1, 2 \tag{3.41}$$

one gets the phase transformation of a lens,

$$t_l = \exp\left[i\frac{k}{2f}(x^2 + y^2)\right]. \tag{3.42}$$

In the last step the substitution,

$$\frac{1}{f} = (n - 1)\left(\frac{1}{R_1} - \frac{1}{R_2}\right), \tag{3.43}$$

is used, where the focal length of the lens is f, the radius of the lens front plane curvature is R_1 and the back plane curvature is R_2. The definition of a propagating wave (3.29) with a negative phase factor is used again. A surface with a positive radius is concave with the light coming from the left [49]. For an incident plane wave on the lens, this is a spherical wave front converging towards a point in a distance f behind the lens which is the focus point (see Fig. 3.7).

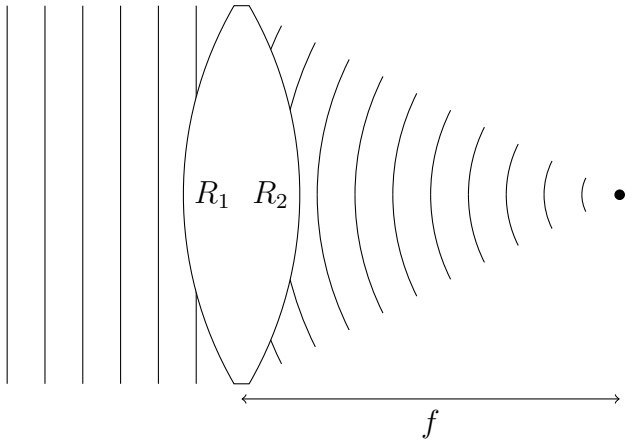

Figure 3.7: Focosing lens

Input placed against a lens

Monochromatic collimated light with the amplitude A passes an input with transparency $t_0(x, y)$ which results in a field amplitude of $A_0 = At_0(x, y)$, where the input phase is set to zero without limitation of generality. Since the distance to the lens is zero, $A_0 = A_1$ resulting in a field behind the lens of

$$A_2(\xi, \eta) = A_1 \exp\left[i\frac{k}{2f}(\xi^2 + \eta^2)\right] = At_A(\xi, \eta) \exp\left[i\frac{k}{2f}(\xi^2 + \eta^2)\right], \tag{3.44}$$

with k and f being the wave vector and the focus length, respectively. Substituting A_2 for U in the Fresnel diffraction integral (3.36) yields,

$$A_3(x, y) = \frac{ie^{-ikz}}{\lambda z} e^{-i\frac{k}{2z}(x^2+y^2)} \iint_{-\infty}^{+\infty} \left\{ A_1(\xi, \eta) e^{i\frac{k}{2}\left(\frac{1}{f}-\frac{1}{z}\right)(\xi^2+\eta^2)} \right\} e^{i\frac{2\pi}{\lambda z}(x\xi+y\eta)} \mathrm{d}\xi \mathrm{d}\eta, \tag{3.45}$$

setting the distance behind the lens z equal to the focus length of the lens f results in,

$$A_3(x, y) = \frac{i}{\lambda f} e^{-i\frac{k}{2f}(x^2+y^2)} \iint_{-\infty}^{+\infty} A_1(\xi, \eta) e^{i\frac{2\pi}{\lambda f}(x\xi+y\eta)} \mathrm{d}\xi \mathrm{d}\eta\,, \tag{3.46}$$

where a constant phase factor is dropped. By comparing (3.46) with the two dimensional Fourier transform (see 3.24), it can be seen that A_3 can be written as the Fourier transform of A_1 multiplied by a quadratic phase factor,

$$\begin{aligned} A_3(x, y) &= \frac{i}{\lambda f} e^{-i\frac{k}{2f}(x^2+y^2)} \tilde{A}_1\left(-\frac{x}{\lambda f}, -\frac{y}{\lambda f}\right) \\ &= \frac{iA}{\lambda f} e^{-i\frac{k}{2f}(x^2+y^2)} \tilde{t}_0\left(-\frac{x}{\lambda f}, -\frac{y}{\lambda f}\right), \end{aligned} \tag{3.47}$$

using $\tilde{A}_1 = A\tilde{t}_0$ in the last step.

Input placed in front of a focussing lens

Considering the situation shown in figure 3.6b, where an object is placed a distance d in front of the lens. If that object with transparency t_0 is illuminated by a planar wave front

with amplitude A, the phase can be set to zero without loss of generality since only the relative phase within the field is relevant. Consequently, the Fourier transform of the field directly behind the object A_0 is written as

$$\tilde{A}_0(u,v) = \mathcal{F}\{A_0\} = \mathcal{F}\{At_0\}. \tag{3.48}$$

The input field A_0 relates to the field directly in front of the lens A_1 in a distance d with $u = \frac{x}{\lambda f}$ and $v = \frac{y}{\lambda f}$,

$$\tilde{A}_1(u,v) = \tilde{A}_0(u,v)e^{i\pi\lambda d\left(u^2+v^2\right)} = A\tilde{t}_0 e^{i\frac{\pi d}{\lambda f^2}\left(x^2+y^2\right)}, \tag{3.49}$$

by comparing this equation with (3.47) one obtains,

$$\begin{aligned} A_3(x,y) &= \frac{i}{\lambda f}e^{-i\frac{k}{2f}\left(x^2+y^2\right)}e^{i\frac{kd}{2f^2}(x^2+y^2)}\tilde{A}_0\left(-\frac{x}{\lambda f},-\frac{y}{\lambda f}\right) \\ &= \frac{i}{\lambda f}e^{-i\frac{k}{2f}\left(1-\frac{d}{f}\right)\left(x^2+y^2\right)}\tilde{A}_0\left(-\frac{x}{\lambda f},-\frac{y}{\lambda f}\right) \\ &= \frac{iA}{\lambda f}e^{-i\frac{k}{2f}\left(1-\frac{d}{f}\right)\left(x^2+y^2\right)}\tilde{t}_0\left(-\frac{x}{\lambda f},-\frac{y}{\lambda f}\right), \end{aligned} \tag{3.50}$$

where it can be seen that the field at the focus of a lens A_3 equals the Fourier transform of the input field t_0 multiplied by a quadratic phase factor and a constant factor. For the case that the distance d of the object in front of the lens equals the focus length f, the equation simplifies to,

$$A_3(x,y) = \frac{iA}{\lambda f}\tilde{t}_0\left(-\frac{x}{\lambda f},-\frac{y}{\lambda f}\right), \tag{3.51}$$

the exact Fourier transform of the input transparency t_0.

In practice, it must be considered that an additional quadratic phase term has to be included in the Fourier transform, if the detection plane is not exactly in the focus plane of the lens. Furthermore, in reality the lens has a finite aperture which also has to be taken into consideration. In the simplest case, the aperture of the lens can be expressed

by a function $P(x, y)$,

$$P(x,y) = \begin{cases} 1, & \text{if inside of the lens} \\ 0, & \text{if otherwise.} \end{cases} \tag{3.52}$$

Taking the finite aperture into account and considering the general case of $z \neq f$ and $d \neq 0$, with (3.49) equation (3.46) can be written as,

$$A_3(x,y) = \frac{iA}{\lambda z} e^{-i\frac{k}{2}\left(\frac{1}{z}-\frac{d}{f^2}\right)(x^2+y^2)} \iint_{-\infty}^{+\infty} \left\{ t_0(\xi,\eta) P(\xi,\eta) e^{i\frac{k}{2}\left(\frac{1}{f}-\frac{1}{z}\right)(\xi^2+\eta^2)} \right\} e^{i\frac{2\pi}{\lambda z}(x\xi+y\eta)} \mathrm{d}\xi \mathrm{d}\eta. \tag{3.53}$$

However, the aperture has no effect if the illuming light is not clipped by the aperture of the lens. Therefore, for simplicity, the aperture is not considered in further observations, since the illuminated area is smaller than the aperture of the lens, as one sees below. In practice, the Fourier spectrum is measured with a phase sensitive detection method and the input is reconstructed via numerical methods with the inversion of equation (3.49).

3.2.2 Field of view and resolution

Two of the key features of every image are the resolution and the field of view. As seen before, the field in the focus plane is related through a Fourier transform with the field of the object plane. Therefore, the mapping of the input to the Fourier plane (see Fig. 3.6) shares all the properties of a Fourier transform. This also includes the Similary theorem (Eq. 3.5), leading to the fact that a high resolution of the Fourier image results in a large field of view in the object plane and a large field of view results in a high resolution of the object.

First, the change in resolution of the image is demonstrated by taking different sized parts of the Fourier spectrum into account. Figure 3.8 shows in the top left corner the original image and on the bottom left its Fourier transform. The two squares indicate two different segments which are shown bottom center and bottom right. From the original Fourier spectrum with 500×500 pixels only 128×128 pixels (big, blue square) and 68×68

pixels (small red square) were taken, respectively. The inverse Fourier transformations of these spectra show the original images field of view with a changed resolution. While the middle image still shows a lot of detail, the right images resolution suffers from the drastically reduced Frequency spectrum ($< 2\%$ of the original information).

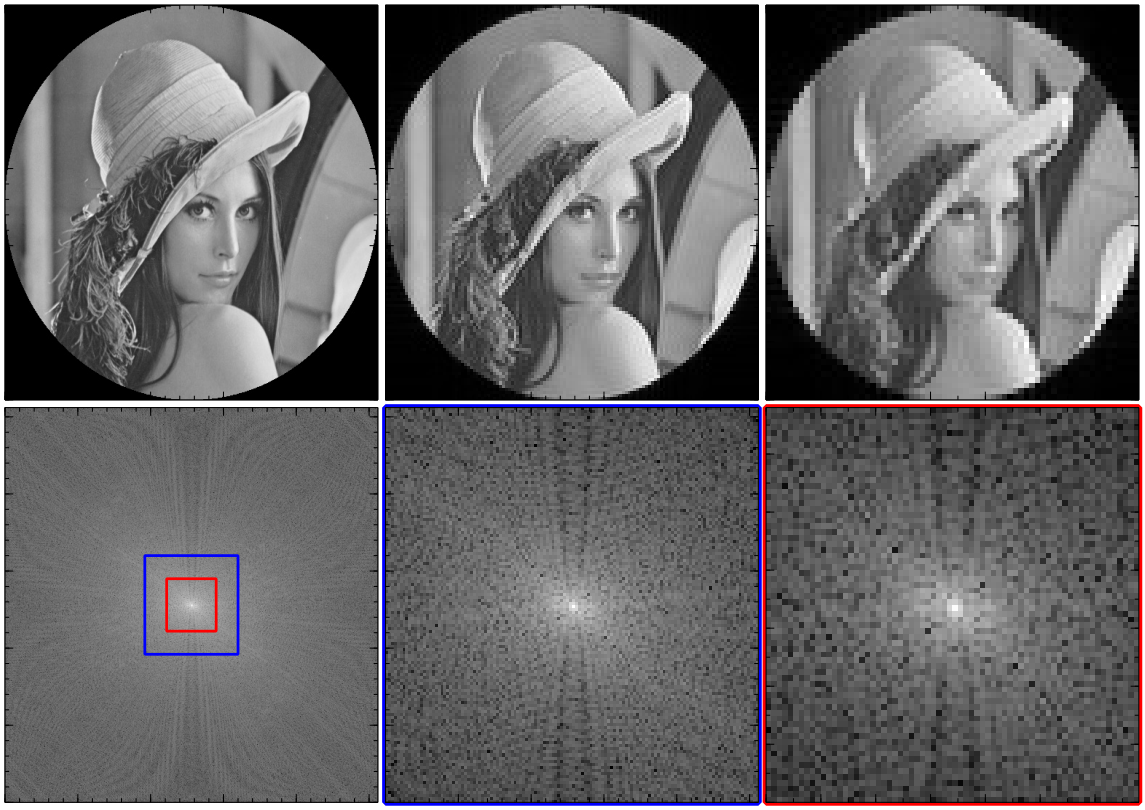

Figure 3.8: The top row shows the original image on the left and the results of the inverse Fourier transform from the Fourier spectra shown in the bottom row. The squares in the bottom left Fourier spectrum indicate the parts of the Fourier spectrum taken for bottom center (big, blue square) and bottom right (small, red square).

By lowering the resolution of the Fourier spectrum, the field of view can be modified of the inverse Fourier transform while keeping it's resolution constant. Figure 3.9 shows the original image on the top left with its respective Fourier transform on the bottom left. The inset shows 30×30 pixels of the original 1024×1024 pixels image. If the resolution of the original Fourier spectrum is reduced to 512×512 pixels, a magnified version of the center segment of the original image is obtained. The inset shows the same 30×30 pixels of the eye which shows that the resolution of the image was not reduced by reducing the

resolution of the Fourier spectrum. The bottom right shows the Fourier spectrum of the original image with a decreased 256×256 pixels resolution by taking only ever fourth pixel of each column and row. The inverse Fourier transformation is again a zoomed in version of the original image with the same resolution, which is shown in the 30×30 pixels inset. In practice, the input is calculated through a numeric back propagation algorithm from the measured amplitude and phase of its Fourier spectrum. The inputs resolution is determined by the field of view of the recorded Fourier spectrum and its field of view results from the resolution of the recorded Fourier spectrum.

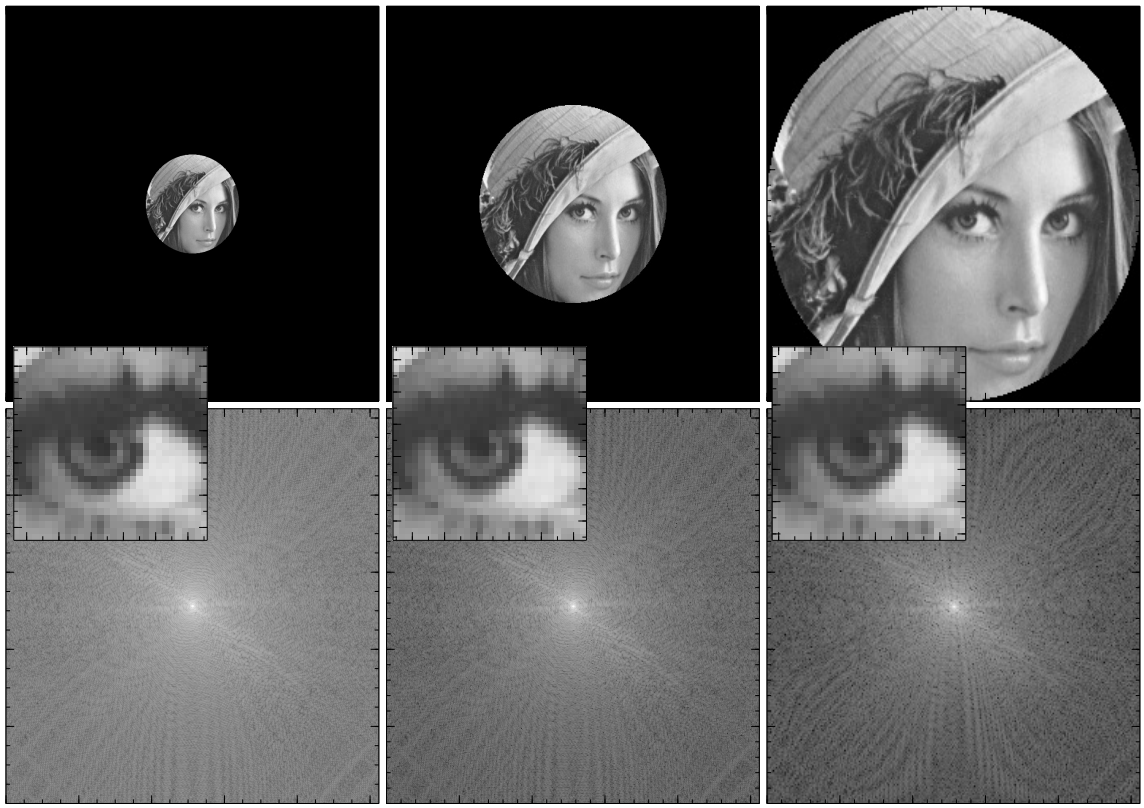

Figure 3.9: The top row shows the original image on the left and the results of the inverse Fourier transform from the Fourier spectra shown in the bottom row. On the bottom left, one can see the original Fourier spectrum of which resolution was reduced from 1024×1024 pixels to 512×512 pixels and 256×256 pixels for bottom center and bottom right, respectively. The insets in each column show a 30×30 pixels segment of the respective inverse Fourier transform.

3.3 Simulation method

The fast Fourier transform (FFT) is utilised to implement an algorithm, based on the formulas derived in section 3.2 to numerically propagate an electrical field through a focussing lens and determine amplitude and phase at its focus. The propagation from the input to the focus is referred to as simulation, while the propagation from the focus plane back to the input is called back calculation.

3.3.1 Input transparencies for Fourier simulation

Since the simulation should be as close as possible to the conducted experiments (see chapter 4), the inputs are chosen to be simple. Even though, the input itself as well as its resolution and field of view vary frequently. Figure 3.10 shows the most common inputs used in this work. All four pictures were generated as a 201×201 array where the values at each array position are represented by the pixel's colour. Because of the grid's periodicity, bright spots are observed in the Fourier spectrum at the corresponding spacial frequencies. This makes it a good test object for Fourier optics. An aperture is a very simple object that can be easily realised in an experimental set-up. The Siemens-star is a fairly simple standard test chart commonly used in imaging applications to estimate the achieved resolution. A Gaussian profile is underlaid to the object, since the output intensity is likely to be a Gaussian profiled beam during measurements (see chapter 4). It is also very convenient since its Fourier transform has again a Gaussian shape. The vast majority of all simulations were performed with either one of those shapes or a combination (width, periodicity, diameter are varied). The way those objects are implemented makes it very simple to combine them through element wise multiplication.

3.3.2 Field propagation equation

To simulate the field in the focus A_3 of the focusing lens (see Fig. 3.6), equation (3.50) is used,

$$A_3(x,y) = \frac{iA}{\lambda f} e^{-i\frac{k}{2f}\left(1-\frac{d}{f}\right)\left(x^2+y^2\right)} \tilde{t}_0\left(-\frac{x}{\lambda f}, -\frac{y}{\lambda f}\right), \tag{3.54}$$

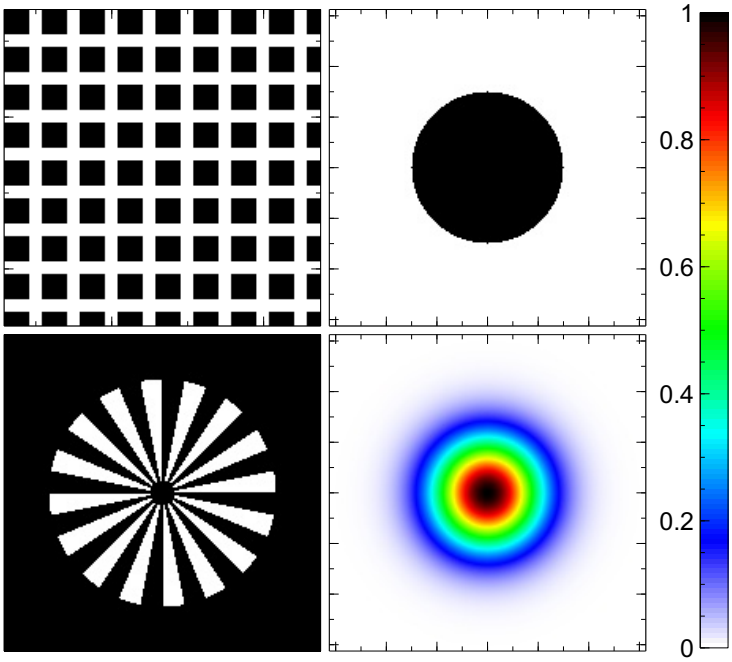

Figure 3.10: Four commonly used inputs objects. From left to right top to bottom: grid, aperture, Siemens-star, Gaussian

where the amplitude is $A = 1$ V/m and the focus length of the lens $f = 0.15$ m. λ is the wavelength of the radiation which is chosen to be 1.19 mm corresponding to a frequency of 252 GHz. k is the wave vector with its the definition $k = 2\pi/\lambda$. The distance of the input t_0 to the focusing lens is d, where the $\tilde{t}_0$ stands for the Fourier transform of the input t_0 which is numerically calculated through the fast Fourier transformation (FFT) (see 3.1.3). Note that the inversion of this formula,

$$t_0\left(-\frac{x}{\lambda f}, -\frac{y}{\lambda f}\right) = \mathcal{F}^{-1}\left\{\frac{\lambda f}{iA} e^{i\frac{k}{2f}\left(1-\frac{d}{f}\right)\left(x^2+y^2\right)} A_3(x,y)\right\}, \tag{3.55}$$

is used to calculate back to the input plane t_0. The back calculation is a crucial tool to gain knowledge on how modifications of the data in the Fourier plane influences the back propagation to the input. Possible modifications might be lowering the resolution or detecting only certain areas of the Fourier spectrum. This is important when the input is calculated from measurement data at the Fourier plane (see section 4).

To be able to plot the results correctly, x and y must be rescaled to the coordinates in the Fourier plane x_f and y_f. y_f is calculated analogically to the here presented x_f,

$$x_f = [\quad -\tfrac{N-1}{2},\quad -\tfrac{N-1}{2}+1,\quad ...,\quad \tfrac{N-1}{2}-1,\quad \tfrac{N-1}{2}]\quad \tfrac{\lambda f}{\Delta x(N-1)} \quad \text{if } N \text{ is odd}$$
$$x_f = [\quad -\tfrac{N}{2},\quad -\tfrac{N}{2}+1,\quad ...,\quad \tfrac{N}{2}-1\quad]\quad \tfrac{\lambda f}{\Delta x N} \quad \text{if } N \text{ is even,}$$

where Δx is the sample spacing in the discrete position array. To insure the existence of a 0 entry in the center, the array is not symmetric if the number of elements N in x is even.

3.4 Intensity and phase

In this section, a closer look is taken on the importance of the intensity and phase in Fourier optics. Some key aspects can already be shown with numerical simulations. Therefore, investigations of noisy intensity and phase are carried out and their impact on the back calculations is compared. Afterwards, some comments on the input-lens distance information are made which is encoded in the field.

3.4.1 Intensity and phase noise

The formulas to calculate the SNR and the DR of a system are defined in equation 2.1 and 2.4. While those values are straight forward for conventional imaging, the situation is different for Fourier imaging. In conventional imaging, the resulting image is not influenced by the detected phase, while the input reconstruction with (3.50) in Fourier imaging is highly phase dependent. In fact, the phase is more important than the intensity for the back calculation which can be easily shown by swapping the phase of two Fourier transformed images (see appendix A.3 for an example). It does not only contain the information about the distance of the input to the focusing lens, but is also crucial for the reconstruction of the input intensity itself. Therefore, the SNR and DR of a Fourier imaging system is better described by the SNR and DR in the back transformation rather than the raw data.

To estimate the impact of experimental noise on the back calculation, the impact of noisy intensity and phase on the SNR and DR of the resulting image are determined. Here, an aperture object is taken and Fourier transformed. In the top row of figure 3.11, one

can see the object on the left, the intensity in the center and the phase on the right. The noise is then added to the simulation results (intensity and phase) shown in the second row. For both, intensity and phase, a random array with the same number of rows and columns is generated. The noise array for the intensity holds values in the range between $1 - n_I$ and 1, where n_I is the intensity noise. The noise array of the phase contains values between $-n_P\pi$ and $n_P\pi$, where n_P is the phase noise. The intensity noise array is element wise multiplied with the intensity array of the simulation, in contrast to the phase noise array which is element wise added to the phase array of the simulation. In the example of the bottom row in figure 3.11, the intensity noise n_I and phase noise n_P have the same value $n_I = n_P = 0.4$. As a result to the added noise, the back calculation (bottom left) shows not an exact replication of the input (top left) but a noisy, uneven circle. The SNR is calculated using equation (2.1), where x_i are only the values located in the center spot of the input. The DR is analogically obtained using (2.4) with $x_{noise,i}$ being the values everywhere but in the center spot. In the example below, the noise values for intensity and phase of $n_I = n_P = 0.4$, result in a SNR of 8.8 and DR of 133.1.

To gain a better understanding on how the noise influences the back calculation, the same procedure of the above example is performed not with a single value for intensity and phase, but with an array for each. Figure 3.12 displays the generated two dimensional colour map with the intensity noise n_I plotted at the x-axis and the phase noise n_P at the y-axis, where the colour of each pixel corresponds to the calculated SNR (left) or DR (right) on a logarithmic scale. As before, the intensity noise n_I is used to generate a noise array with random values between $1 - n_I$ and 1 which is then element wise multiplied to the simulated intensity. The phase noise n_P is again used to create a random value array with values between $-n_P\pi$ and $n_P\pi$ which are then element wise added to the phase of the simulation. The resulting SNR and DR of the center spot are presented as one pixel in the coordinate system at its corresponding position (n_I,n_P). Note that the highest SNR and DR values (with no noise) are clipped to 40 dB (10^4) and 80 dB (10^8), respectively, for better visibility. At a first glance, one already notices the very similar behaviour of SNR and DR to phase and amplitude noise. The SNR map (see 3.12a), however, has a higher granulation than the DR map (see 3.12b). It is believed that this is a result of statistics,

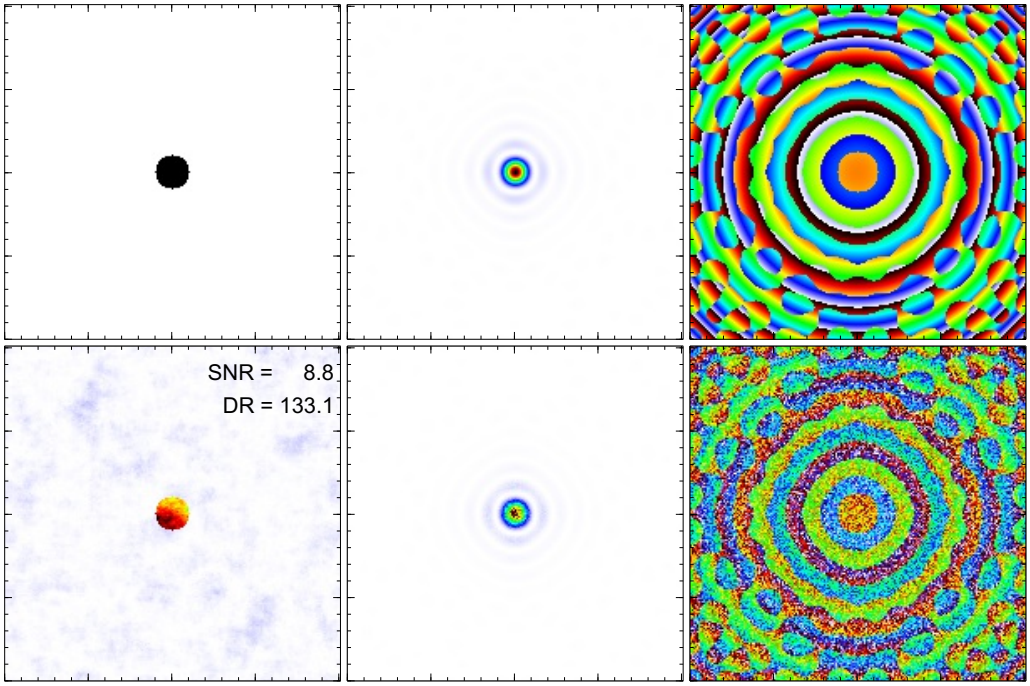

Figure 3.11: First row shows an aperture on the left, its Fourier spectrums intensity and phase at the center and right, respectively. The second row shows the back calculation of the input on the left with the corresponding noisy intensity at the center and noisy phase at the right.

because the S_{std} is calculated using only $N = 317$ (see Eq. 2.1) values compared to the N_{rms} computation where $N = 4084$ (see Eq. 2.4) values are used. Both, SNR and DR drop faster in the direction of phase noise. The drop in SNR or DR has only a strong dependence of the intensity noise when the phase noise is very low or zero. The phase noise, however always has a strong impact on the obtained SNR and DR indicated by the horizontal colour trends. This strengthens the previous statement of this section where in Fourier optics, more importance is attributed to the phase than to the amplitude.

3.4.2 Encoding of the distance information

For the case of detecting the light field in the focus plane of the lens ($z = f$), the exact Fourier spectrum of an input a distance d in front of the lens is measured. Considering $d \neq f$, the Fourier spectrum is multiplied by a quadratic phase factor (see Eq. (3.50))

$$e^{-i\frac{k}{2f}\left(1-\frac{d}{f}\right)\left(x^2+y^2\right)}, \tag{3.56}$$

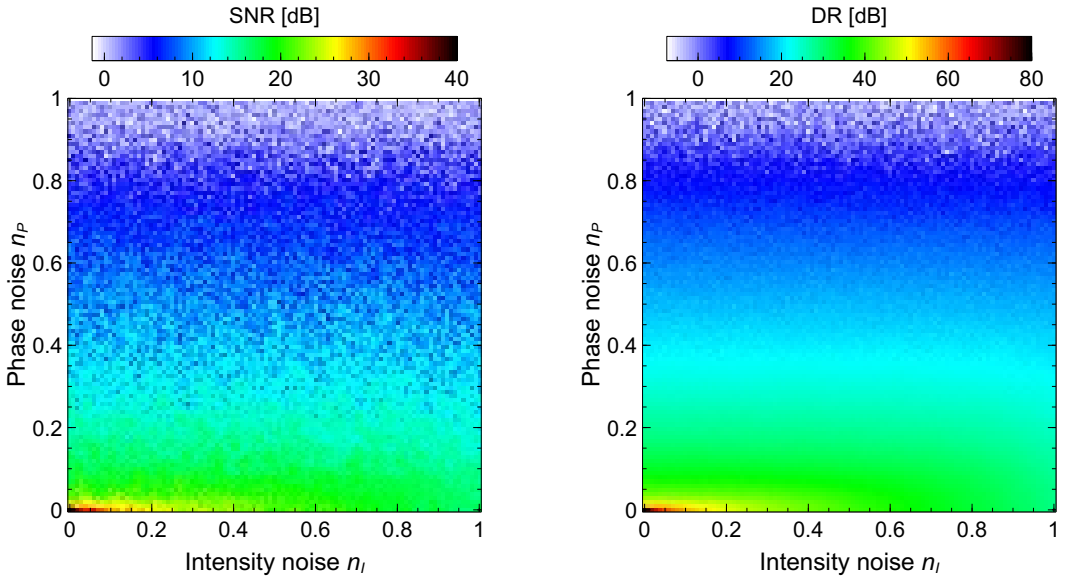

(a) SNR as a function of n_I and n_P

(b) DR as a function of n_I and n_P

Figure 3.12: (a)The resulting signal to noise ratio (SNR) and (b) dynamic range (DR) of the back calculation when noise is applied on the intensity and phase of the simulation.

where k is the wave vector $\frac{2\pi}{\lambda}$ and f the focus length of the lens. The distance of the object to the lens d does not appear anywhere else in the Fourier spectrum calculation. Therefore, the intensity of the Fourier spectrum is independent on d. The phase, however, features a curved phase factor on top of the phase of the objects pure Fourier transform. The curvature is then $-\frac{k}{f}(1-\frac{d}{f})$. For a given set-up with a fixed wavelength, this is a linear function in d with a zero point at $d = f$ where the curvature changes sign from negative to positive. To obtain a sharp input, it is crucial to use the right d in the reconstruction. The better the phases curvature can be determined, the higher is the depth sensitivity of the Fourier imaging process. Without knowledge of the input, this is challenging, since the curvature is on top of the phase of the inputs Fourier transform. At this point it is noteworthy that changing the focus length f will alter the gradient of the d dependent curvature change. Or in other words, the steepness of the linear curvature function. A shorter focus length results in a steeper gradient and therefore makes the set-up more depth sensitive as one with a longer focus length, since a smaller change in d results in a bigger change of the phase curvature even with taking the rescaling of the Fourier spectrum into account.

3.5 Simulation results

Numerical simulations can provide some important information and give insights on how an experimental set-up might perform. The more accurate a simulation can be set up, the closer the results are to the measurements. It also shows whether or not all the important influences are understood and taken into account. Simulated results which differ a lot from the measured data indicate another important mechanism not yet considered. Therefore, the following section discusses some of the most important results regarding the simulations being performed to generate a more complete picture of the Fourier optics set-up. First, a look at the results created by the already seen inputs is taken. Secondly, the situation is changed by a modified detection pattern and last with multiple objects in a three dimensional scene.

Here, only reasonable inputs and boundary conditions are chosen to evaluate the performance reduction which is to be expected when one has to compromise on detection area and resolution in favour of acquisition speed.

3.5.1 Different objects

Above, different inputs can be seen in figure 3.10 which are used in simulations of a Fourier optics set-up. Figure 3.13 shows a simulation of three different objects shown in the top row with values: $A = 1$ V/m, $f = 0.15$ m, $\lambda \approx 1.2$ mm and $d = 0.13$ m (see Eq. (3.54)). The center row shows the simulations intensity spectrum and the bottom row shows their respective phase. The top left input is a Gaussian beam shape with the form,

$$f(x, y) = \exp\left(-\frac{(x - x_0)^2 + (y - y_0)^2}{2c^2}\right), \tag{3.57}$$

where c is chosen to be 9 pixels and x_0, y_0 are 1, 2 pixels, respectively. This Gaussian intensity distribution is multiplied with a centered aperture with a diameter of 44 pixels

of the form,

$$a(x,y) = \begin{cases} 1, & \text{if } x^2 + y^2 \leq 22 \\ 0, & \text{else} \end{cases} \tag{3.58}$$

This configuration was reused for the other two inputs. For better visibility, the initial 201×201 pixels array (not shown here) is zoomed to display 96×96 pixels for the inputs and 168×168 pixels for intensity and phase, respectively. This corresponds to a displayed area of 144 cm^2 in all cases, indicating a resolution of 8 pixel/cm and 14 pixel/cm for the input and Fourier spectrum, respectively. With a wavelength of 1.2 mm this is slightly oversampled for the letter. The result of the simulated input is a simple spot in the intensity and concentric rings in the phase. The phase has some rotationally asymmetry. This can be attributed to the slight offset of the Gaussian function ($x_0 = 1$ pixel and $y_0 = 2$ pixels) away from the center of the aperture to simulate with more real boundary conditions, since it is not trivial to align the lenses perfectly centric in a real set-up.

For the second input in the center column, the left input was multiplied with a grid where the periodicity of the grid is 6 pixels and the grid width (white stripes) is 2 pixels. With the before introduced resolution, that corresponds to 7.5 mm and 2.5 mm, respectively. The input is again numerically propagated through the set-up with a resulting intensity and phase shown in the center and bottom row. The Fourier spectrum's intensity shows a bright center spot with a grid of spots around it. The spots become weaker the further they occur away from the center with the first order spots being the second brightest after the zero order spot in the center. The smaller the aperture of the input, the broader each spot is. The phase has again a similar grid like pattern with points of more or less constant phase at the positions of higher intensity. By comparing the phase pattern of the Gaussian Fourier transform and the latter, the phases can be seen to have similarities, featuring the same asymmetrical center and phase value indicating the common features of the input.

The input at the right consists again of the same Gaussian illumination multiplied by the aperture of the first input. This time it is additionally multiplied with a Siemens-star

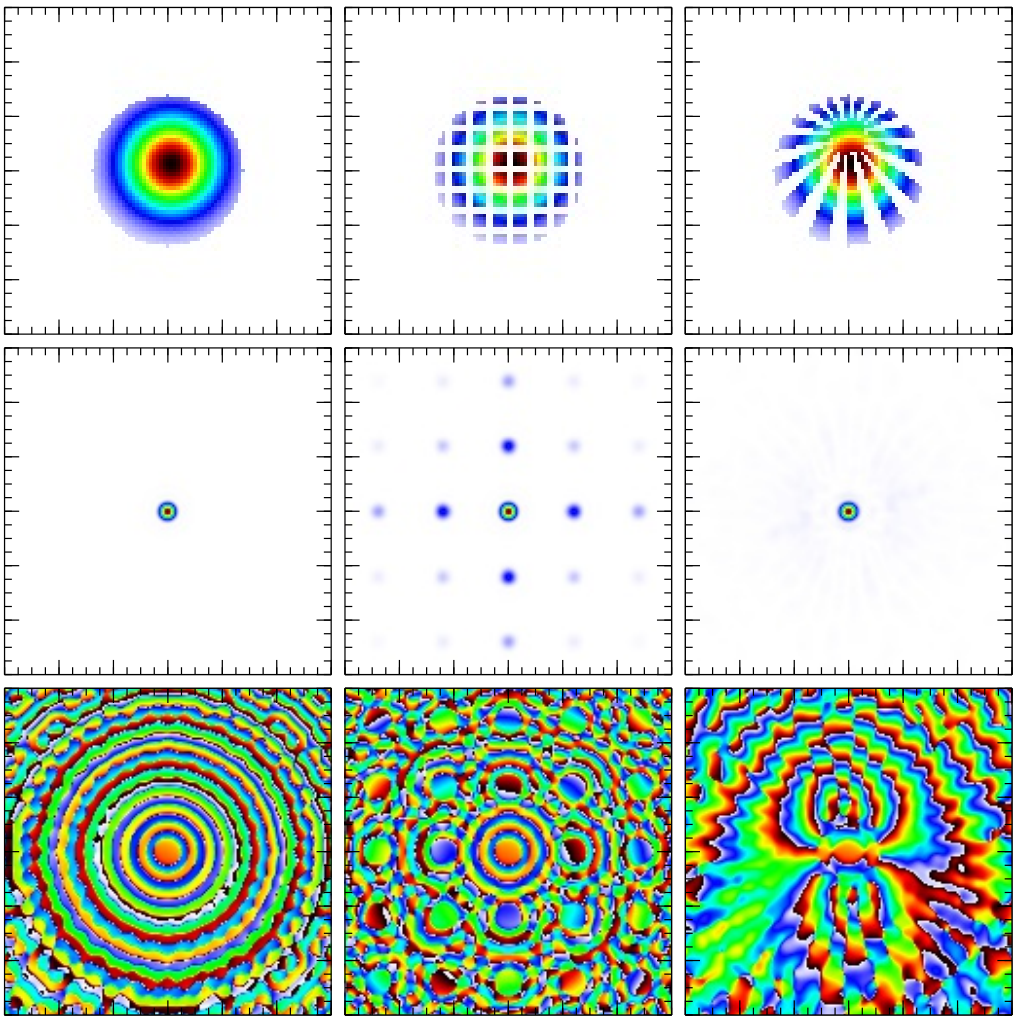

Figure 3.13: The top row shows 96×96 pixels out of 201×201 pixel of the inputs consisting of either Gaussian and aperture (left), Gaussian and aperture overlayed with a grid (center) or Siemens-star (right). In the center row, the respective intensity spectra and at the bottom, the resulted phase in the Fourier plane can be seen.

pattern. The inner radius, where the opaque fingers stop is chosen to be 5 pixel with a total shift relative to the center of the array being 10 pixel in y direction. On first glance, the intensity result of the simulation looks just like the Gaussian intensity with the aperture. But a closer look unveils a ray like pattern around the center spot. The phase is even more interestingly shaped. It builds a two leaf like pattern pointing away from the center. Through multiple simulations, the axis of symmetry is found to be dependent on offset direction of the Siemens-star. Also, there is no center area with concentric pattern.

3.5.2 Detection pattern

In the above simulations, no information is lost or altered through noise, interpolating or other methods. Therefore, the inverse propagation using equation (3.55) produces exactly the given input without any deviation. The area, over which the Fourier spectrum is spread is quite large. For measurements, this means a large range must be covered with high resolution in order to detect the hole area. This could either not be possible or lead to a long acquisition time. Previous simulation results are reused, modified in "detection" area, resolution or both and then back propagated for a better understanding on how the back calculated objects are effected by those modifications.

Figure 3.14 shows the back calculations of modified Fourier plane data. The starting point are again the three different, 201×201 pixels objects (96×96 are shown). The center row shows the center 101×101 pixels of the simulated phase in the Fourier plane padded with zeros around to generate an array with the original 201×201 pixels (168×168 are shown). Even though only the phase is displayed, the same procedure is done with the intensity of the Fourier spectrum. This modified data is then used to calculate back to the object plotted in the bottom row using equation (3.55). The back calculation of the Gaussian intensity plus aperture shows almost no difference to the original input with the exception of a not quite as sharp edge. The loss of information is more relevant for the back calculation of the grid (center column). Here, the grid like pattern can still be seen but all sharp edges are washed out and in the place of small squares, dots are visible. The highest intensity, however, still shows the center spots which fades out towards the aperture's edge. The back calculation of the Siemens-star suffers also from the reduced data in the Fourier plane. Again, edges appear to be more smooth due to averaging effects, which leads also to a different intensity distribution over the back calculation. The area with the highest intensity in the input, right at the transition from the fingers to the transparent center, does not show a smooth transition of intensity towards the center anymore. The thin tips of the transparent fingers are interpolated with the nearby opaque areas leading to a reduced intensity just around the center transparency.

By changing the array size from 201×201 to 101×101 pixels, the data size is reduced

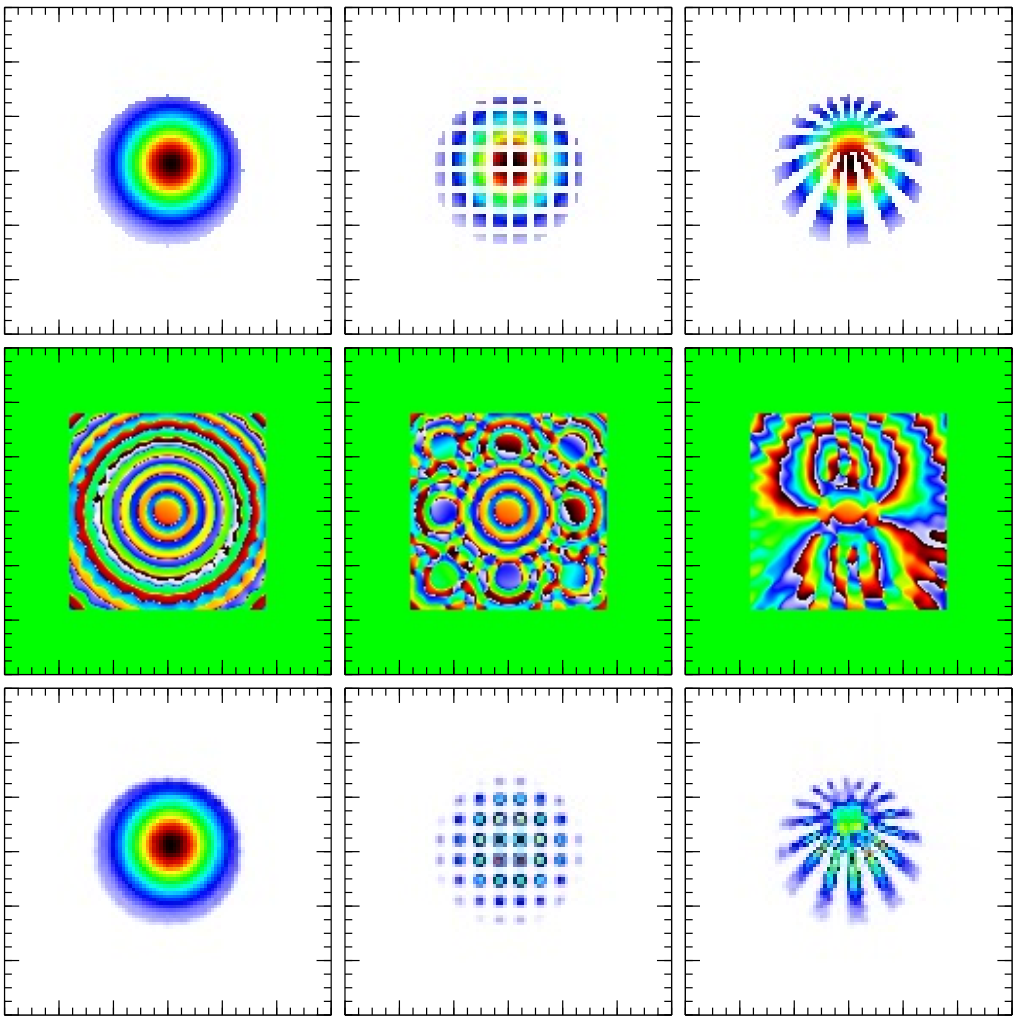

Figure 3.14: The top row shows the inputs consisting of either Gaussian and aperture (left), Gaussian and aperture overlayed with a grid (center) or Siemens-star (right). In the center row one sees, the center of the resulting phase (101×101 pixels) padded with zeros to generate a again 201×201 pixels array (168×168 are shown). The right column shows the respective back calculatoin using the modified simulation results.

to a quarter of its initial value. Removing any input higher spatial frequencies results in a reduction in the quality of the back calculation image. Objects with only a few sharp edges or small features do not contain many high frequency components. Therefore, a restriction of those object's Fourier spectrum to lower spacial frequencies does not have a big impact on the back calculation (see first column Fig. 3.14). Much more affected are the back calculations of objects with a higher content of small features and sharp edges. The simulated grid in the center column of figure 3.14 contains crossed opaque

stripes that have a sharp edge to the transparent squares. Replacing the higher spacial frequencies with zeros has a high impact on the back calculation. The general structure is still grid shape, but the transparent squares are reduced to simple spots. A similar situation can be observed with the Siemens-star. The sharp edges of the opaque fingers narrowing towards the center indicate high spacial frequencies occurring in the Fourier spectrum. Neglecting this information results in a less sharp Siemens-star with an altered intensity distribution.

Even though the objects are changed, they are still easily distinguishable. However, one might not be able to tell apart similar objects after the higher spacial frequencies are removed. The reduction of information effects mostly the small features in the object leaving the general structure untouched. This allows a differentiation of the simulated objects. Therefore, it could be advantageous to reduce the spacial frequencies in experiments, since a reduction in spacial frequencies corresponds to a reduced detection area in the Fourier plane. A smaller recording area results in fewer points to measure, reducing acquirement time per Fourier spectrum.

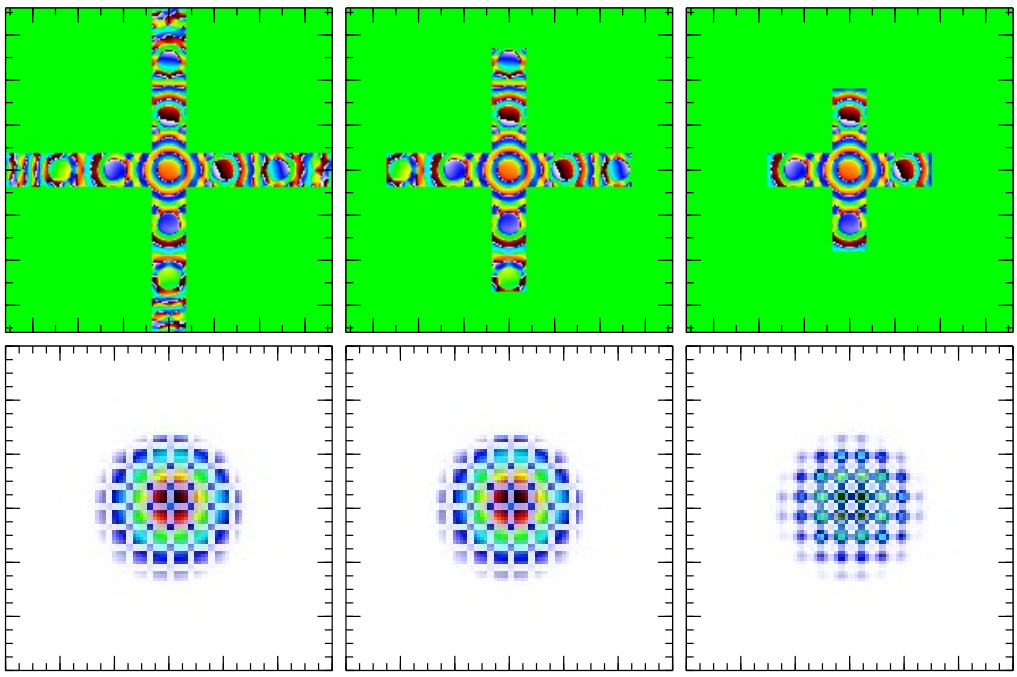

Figure 3.15: The top row shows the simulated phase of a grid object where only a center column of 21 pixel in widht and a center row of 21 pixel in hight are used. The bottom row shows the respective back calculations.

The number of pixels can be reduced even further and still increase the reconstruction's quality. This is possible by reshaping the pattern of detection. Figure 3.15 shows simulations of the known grid input (see Fig. 3.14) but instead of using a square in the center for the back calculations, the used information lies on a centered cross with a width of 21 pixels. The top row shows the used inputs (201×201 pixels plotted) with their respective back calculations in the bottom row. For better visibility, out of the total number of pixels (201×201) only 96×96 pixels of the back calculations are plotted. From left to right the crosses have width and hight of 201, 151 and 101 pixels, respectively. This results in the total number of pixels being 8001, 5901 and 3801. Compared to the previous 101×101 pixels, the total number of used pixels is reduced for all three crosses, but the back calculations of the biggest cross on the left is very similar to the input itself. The second biggest cross in the middle has sufficient information to generate an almost exact reconstruction of the input. Only the smallest cross with a width of 101 pixels shows no squares, but spots aligned in a grid shape which is the same case as the situation of figure 3.14. This behaviour is attributed to the unique pattern of a grid. Since its general shape is almost only made up by horizontal and vertical spacial frequencies, it is sufficient to only use those frequencies aligned horizontal and vertical in the Fourier spectrum for the back calculation. Most of the other frequencies are zero and therefore not as important. In general, his does not work for a generic input. It is highly dependent on the input's structure, which spacial frequencies it contains and therefore at which positions in the Fourier spectrum the intensity is increased. If specific features of an input are required, the detection area could be tailored to the spacial frequency of those features to detect them with a minimum detection area and time.

3.5.3 Three dimensional scene

Above, the importance of the distance for the back calculation is mentioned. Only if the correct distance of the object to the lens is used for the back calculation, a sharp image of the back calculation is produced. Simulations with the Siemens-star at four different distances are performed to show the effect of using various distances for the

back calculation. The four columns of figure 3.16 show the results of four simulations placing the Siemens-star input (see Fig. 3.14) at four different positions 12, 14, 16 and 18 cm away from the focussing lens. To demonstrate how potential measurement results look like, just the center 101×101 pixel are taken and padded with zeros to form 201×201 pixel spectra for the back calculations. Each modified Fourier spectrum is then used to calculate back to the object. Instead of using just one distance for back calculations, four distances 12, 14, 16 and 18 cm are used, shown in each row. Only where the used distance for the back calculation (rows) matches the distance where the Siemens-star input is placed (columns), the back calculation creates a sharp image of the input (see Fig. 3.14). For better visibility only 50×50 pixels are shown in each panel. This series of simulations shows the sensitivity of the back calculation towards the distance used. In order to calculate back to the input, the position must be known. This might lead to complications in reality, where the distance is not or just approximately known and the sharpest image must be chosen out of a series of back calculations with each using a different distance from object to the lens.

The sensitive to the distance also holds the chance of scanning through a three dimensional scene of different objects. Figure 3.17 presents a simulation of a three dimensional scene where two different inputs are used in one set-up. Top left (1) of figure 3.17a shows the known Siemens-star input, multiplied by a Gaussian intensity distribution and an aperture as before (only the center 98×98 pixel out of 201×201 pixel are shown). The Siemens-star is placed at a virtual distance of 14 cm away from the lens. This input is then propagated to the plane 8 cm away from the lens where the second object is placed. The second object is the previously used grid shown in the top right (2) (only the center 98×98 pixel out of 201×201 pixel are shown). At this plane, the intensity of the electric field is generated through multiplication of the propagated Siemens-star intensity with the grid pattern. The phase is simply given by the field propagated from the Siemens-star input. From this point, the simulation is performed as before with the combined field of Siemens-star and grid used as an input. The resulting intensity and phase of the Fourier spectrum are shown bottom left (3) and bottom right (4), respectively. Again, to mimic a measurement, only the center 101×101 entries are used and padded with zeros to form

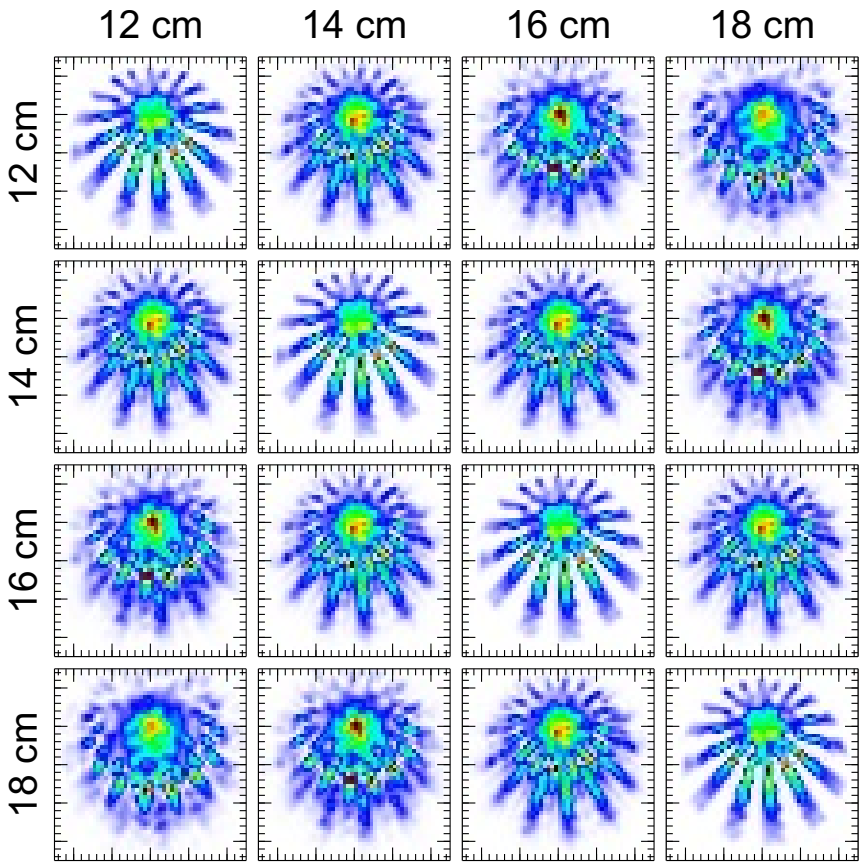

Figure 3.16: Each column represents a set of data at distances 12, 14, 16 and 18 cm. Each row represents a set of back calculations with the back calculated distance 12, 14, 16 and 18 cm. The positions, where the back calculated distance matches the real distance, the back calculation results in a sharp image of the Siemens-star input.

a 201×201 entries field array (168×168 pixel are shown). Figure 3.17b shows the back calculations of the simulated Fourier spectrum for four different distances 8, 10, 12 and 14 cm from the object to the lens. Obviously, the Siemens-star input should be visible at 14 cm and the grid at 8 cm, since those inputs are placed at those planes to generate the Fourier spectrum. The grid features come out quite good compared to the previous grid simulation. The Siemens-star, however, is not visible at its position. The poor quality of the back calculations has multiple origins. First, the Siemens-star is illuminated by a Gaussian beam profile like it is in a measurement. Second, the grids features dominate the scene by blocking the line of sight to the Siemens-star. Also, by using just the center

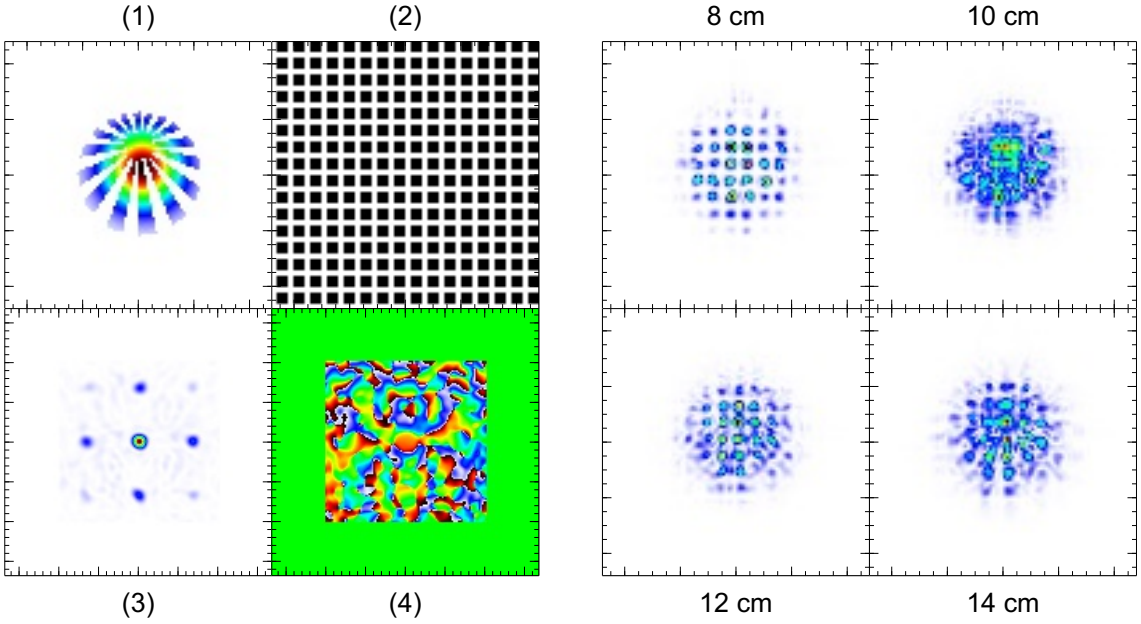

(a) Siemen-star and grid input

(b) Back calculation at different positions

Figure 3.17: (a) (1) and (2) are the Siemens-star object and the grid input, respectively. (3) and (4) are the center 101×101 pixel intensity and phase at the Fourier plane padded with zeros to make a 201×201 pixel field. (b) The result of the back calculation using the field of (a)(3)+(4) for different distances to the lens (8, 10, 12 and 14 cm).

101×101 elements of the Fourier spectrum array for the back calculation, a large portion of information is neglected. For a single input, the spacial frequency restriction was still acceptable to retrieve the input at a reasonable quality. This can not be said for the three dimensional scene with two objects. In the present case, the Siemens-star can not be identified. In order to capture a three dimensional scene with multiple objects, the detection range has to be increased and less opaque objects have to be used to retrieve optimal results.

4 Terahertz Fourier imaging

In order to realise Fourier imaging measurements, the intensity and the phase in the Fourier plane must be detected. Here, a method is presented, on how THz Fourier imaging can be realised through heterodyne detection. This detection method is successfully demonstrated using two electrical multiplier chain sources mixed on a TeraFET detector for amplitude and phase measurements in the Fourier plane. This information is used to recover the object through a numerical back calculation.

4.1 Principle of heterodyne detection

Field effect transistor detectors are power detectors and therefore sensitive to intensity but not to the optical phase. Through optical mixing it is still possible to capture the phase. In order to do so, the probe signal is overlayed with a phase stable reference signal called the local oscillator (**LO**). The resulting interference (beating) carries information about the amplitude and the phase of the probe signal. If the frequencies of the probe signal and the LO are slightly different, this technique is called optical heterodyning, optical mixing, photomixing light beating or coherent optical detection [58].

The time dependent electrical fields of the probe and the LO signal are $E_{sig}(t)$ and $E_{LO}(t)$, respectively. Then, their fields can be written as [55],

$$E_{sig}(t) = A_{sig} \cos\left(\omega_{sig} t + \phi\right) \text{ and} \tag{4.1}$$

$$E_{LO}(t) = A_{LO} \cos\left(\omega_{LO} t\right), \tag{4.2}$$

with their frequencies ω_{sig}, ω_{LO}, amplitude A_{sig}, A_{LO} and a constant phase difference ϕ.

If the two signals are aligned parallel and have the same polarisation, the superposition of the two fields is simply their sum. Since the intensity is proportional to the square of the electrical field, the intensity of the interference is proportional to [58],

$$I \propto \left[A_{LO}\cos\left(\omega_{LO}t\right) + A_{sig}\cos\left(\omega_{sig}t + \phi\right)\right]^2. \tag{4.3}$$

By expanding the product, reordering and using the identities,

$$\cos^2 x = \frac{1}{2}\left[1 + \cos(2x)\right] \text{ and} \tag{4.4}$$

$$\cos x \cos y = \frac{1}{2}\left[\cos(x-y) - \cos(x+y)\right], \tag{4.5}$$

one obtains three kind of terms,

$$\begin{aligned} I \propto & \frac{1}{2}\left[A_{sig}^2 + A_{LO}^2\right] \\ & + A_{sig}^2\frac{1}{2}\cos(2\omega_{sig}t + 2\phi) \\ & + A_{LO}^2\frac{1}{2}\cos(2\omega_{LO}t) \\ & + A_{sig}A_{LO}\frac{1}{2}\cos((\omega_{sig} + \omega_{LO})t + \phi) \\ & + A_{sig}A_{LO}\frac{1}{2}\cos((\omega_{sig} - \omega_{LO})t + \phi). \end{aligned} \tag{4.6}$$

A constant term, three (in this notation) high frequency terms with either the doubled frequency of ω_{sig}, ω_{LO} or the sum of them and the low frequency term formed by the difference of these frequencies. Band pass filtering can be used to exclude all but the low frequency term from further consideration. The filtered interference signal's amplitude is proportional to the product of the LO's and probe signal's amplitude. Therefore, by providing a strong LO signal, heterodyne techniques achieves an amplification of the signal resulting in an increased performance of heterodyne detection compared to direct detection [58–60]. If a lock-in amplifier is used with the difference frequency as the reference signal, the phase difference between locking frequency and beat signal can be obtained. This is all that is required for Fourier imaging since only the relative phase within

the Fourier plane is relevant and a constant phase offset is taken out of consideration in the first place (see section 3.1.5).

4.2 Optical setup for heterodyne detection

A heterodyne detection setup has to include two sources which have to have two slightly different frequencies mixed on a detector. For this purpose, a terahertz (THz) antenna coupled field effect transistor (TeraFET) is utilised to measure the mixed radiation from the source and LO. The detectors principle relays on resistive mixing below the transit-time and transforms to plasmonic effects above [22–25]. The presented data is conducted with two different setups, where one features a beam splitter to focus both source and LO on the detector. The second setup is based on a linear configuration without the need of a beam splitter. Firstly, the electronics of both setups is presented. The beam splitter configuration is presented in detail before the linear configuration is introduced which adopts most of the former techniques.

4.2.1 Electronics of heterodyne detection setup

This setup utilises two commercial available electronic 300 GHz emitters to generate two slightly different frequencies. Those emitters are based on multiplier chains and are widely used as sources for frequencies below 0.7 THz [61–63]. Two frequency synthesisers are used to generate the input frequencies between 12 and 18 GHz with a frequency difference of 1 kHz which are then multiplied ($\times 18$) to 216-324 GHz and emitted by the sources. Although, one synthesiser is clocked by the other, their respective phase delay is not stable enough to use an external 18 kHz ($1\text{kHz} \times 18$) reference for the lock-in amplifier. Figure 4.1 shows the configuration used, where a -10 dB part of the electrical 15 GHz and 15.000001 GHz (example frequency) signals are split, mixed and filtered to generate the 1 kHz difference frequency as a more stable reference input for the lock-in amplifier. This way, the reference frequency will dynamically adjust to any relative drift of the two synthesisers. Note that the lock-in amplifier has to be set to detect the 18th harmonics of the reference signal, since the synthesiser's frequency is multiplied. This configuration

ensures no frequency drift occurs. Therefore, the reference frequency can be efficiently generated, but also more easily compared to including another external signal generator.

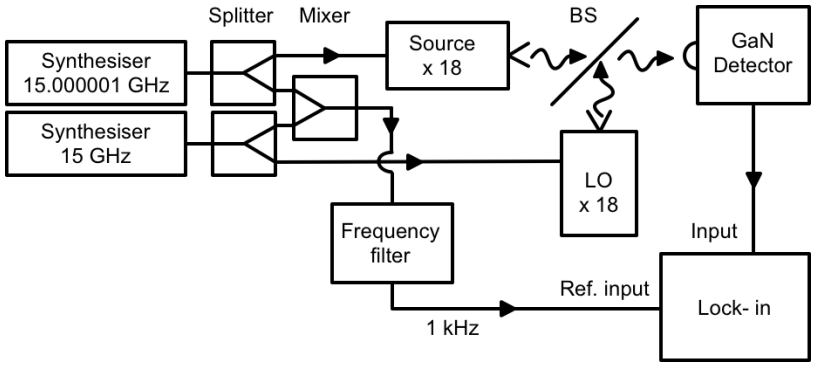

Figure 4.1: The electronics used in the heterodyne setup with two synthesisers (15 GHz example frequency), splitter, one mixer, frequency filter two sources, one detector and one lock-in amplifier.

4.2.2 Optical setup using the beam splitter configuration

To realise heterodyne detection, the radiation of source and LO has to be incident on the detector. Ensuring a stable LO signal over the entire measurement is crucial. For imaging, this means a constant LO signal over the whole detection range. The most effective way to achieve a constant relative position of LO and detector is to move the source arm relative to the LO and detector. A sketch of the optical setup is shown in figure 4.2 with source arm and LO oscillator arm. The latter consists of the source with mounted spherical collimating lens, a spherical focussing lens and the beam splitter to focus on the detector. The plano-convex lenses are made of polytetraflourethylene (**PTFE**) with a three inch diameter and a focal length of 150 mm [64]. The source arm indicated by the dashed rectangle features two spherical lenses for collimation and focussing. The object of interest is put inside the collimated beam path. The entire source arm is mounted on a three dimensional translation stage and is therefore movable in all directions for creating images through a scanning process.

The beam splitter which overlays both beam paths, is a whole 4 inch silicon waver coated at one side (towards the source) with a 7 nm chrome layer as an anti-reflection coating [65]. The detector is a single TeraFET detector with a 12 mm diameter substrate mounted

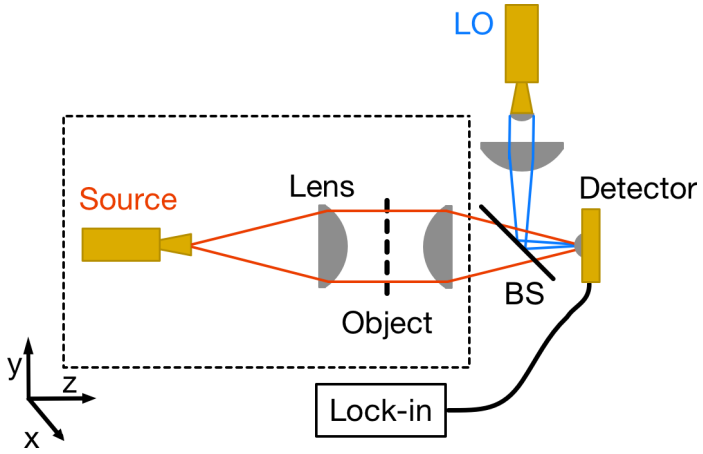

Figure 4.2: The Fourier optics setup with the source and local oscillator (LO) comined with a beam splitter on the detector for phase sensitive detection. The object is placed in the collimated beam of the source which is mounted together with the source, collimated lens, and focussing lens on a three dimensional translation stage.

hyper hemispheric silicon lens [40, 41]. Its antenna is optimised for the lower regime of the THz sources which results in a maximum signal at 239 GHz. In this configuration, the detector is based on GaN/AlGaN high-electron-mobility transistor (**HEMT**) technology [37–39]. The detector is housed in a small metal box with only one opening for the silicon lens, just like the detector in a previous section (see Fig. 2.4a). The required gate voltage is generated with a voltage supply/monitor over an SMA connector. Another SMA connector feeds the detector's output to the lock-in amplifier.

4.2.3 Optical setup without beam splitter

The same idea of a movable source arm relative to the LO and detector leads to another approach in the LO arm design in which the beam splitter is removed. First, because the beam splitter holder could cuts out parts of the fourier spectrum and secondly, astigmatism introduced by the tilted Si-waver in the beam path. Instead of coupling both beam paths through the silicon lens and substrate to the detector, the LO radiation illuminates the detector directly from air to antenna. This is not possible with a metal box housed detector described in the previous setup. For this configuration, the detector is mounted on a cage system with the lens pointing to the source and the other side pointing to the LO. Also, big

standing waves of the LO form between detector and source, leading to field enhancement which can be exploited for the heterodyne detection (see Fig. A.4). The spherical lenses[1] are again plano-convex made of PTFE. The substrate lens is a 4 mm diameter spherical silicon lens glued on the back side of the detector. The latter is still a TeraFET but changed to one based on CMOS technology [22–25] featuring a protection diode for this sensitive device. The spiral antenna has its highest signal output at 252 GHz. Although the coupling efficiency is expected to be reduced compared to the coupling through the substrate [66, 67], the relative loss in signal is not as severe because the beam splitter in the other configuration halves the signal before it even gets to the detector. With a higher noise equivalent power of this detector compared to the GaN/AlGaN detector, the overall performance is expected to be higher than the previous configuration. Just like in the previous configuration, the image is created through scanning the source arm over a certain range relative to single pixel detector.

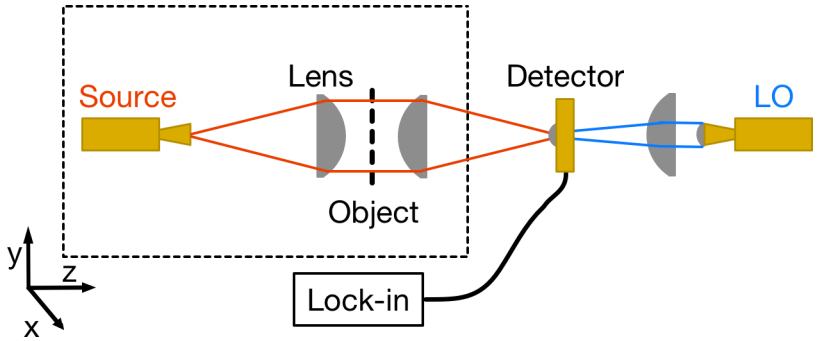

Figure 4.3: The Fourier optics setup with the source and local oscillator (LO), focussing the source through the substrate lens on the detector and the LO directly from air to the antenna. The object is placed in the collimated beam of the source which is mounted together with the source, collimated lens, and focussing lens on a three dimensional translation stage.

4.3 Heterodyne measurement results

The previous presented setup in the two configurations are used to measure different objects at various distances to the focus lens. The measurements are performed to

[1] The same lenses of the previous setup are reused in this setup.

resemble the above shown simulations to ensure comparability and enable statements on the data quality. First, the two distinctive objects, the grid and the Siemens-star are presented as well as their corresponding measurement with back calculation outcome are compared with the simulation results . To follow the previous simulation chapter, the Siemens-star input is placed at different positions and back calculated to show the predicted sensitivity to depth in front of the lens.

4.3.1 Measurement of different objects

The grid and the Siemens-star are the two objects chosen to be analysed in both setups. Since those objects are used in the Fourier simulation above (see section 3), the results of simulation and measurement can be compared. Figure 4.4 shows the grid and Siemens-star object used for the measurements. The grid's stripes as well as the Siemens-star fingers are both metal and therefore completely opaque for THz radiation. The plastics of the Siemens-star on which the metal is applied has a minor effect on the THz radiation. The square holes in the grid are 5 mm and the stripes are 2.5 mm wide. The Siemens-star has an outer and inner diameter of 105 mm and 5 mm, respectively. With twenty opaque fingers and twenty gaps, the tips of the metal fingers at the inner radius are roughly 0.6 mm wide.

By inserting the grid object of figure 4.4a in the collimated beam part (see Fig. 4.2), the intensity and phase shown in Fig. 4.5a are measured. The area of measurement covers an area of 8×8 cm^2 with a pixel pitch of 1 mm. The scanning program accounts for the different scanning directions of the detector is by shifting the pixels from forward and backward movement deleting the overhang, resulting in a lowered number of points in x-direction depending on the setting. In this case the resulting measurement includes 81×72 pixels for both amplitude and intensity. Before the data is saved, the center spot is shifted to the center of the array by adding rows and columns of zeros to the array. The center is determined by calculating the center of mass of the center spot (th magnitude is at least 0.7 of the maximum magnitude). After the shift, the measured data is padded with zeros to generate a square shape with a side length which is two times the side length

of the y-direction. For the presented data, the field is represented by a 170×170 pixels array. This padding results in an interpolated result for the back calculation. Padding of zeros is a standard procedure in Fourier analysis [49]. By applying formula (3.55) to the data, the field is back propagated to the object plane resulting in the figure shown in figure 4.6a. As before, the resolution in the Fourier plane determines the field of view of the back calculation while the field of view of the Fourier plane determines the resolution of the back calculation. A pixel pitch of 1 mm at 250 GHz and 0.15 m focus length results in a field of view of $\sim 9.4 \times 9.4$ cm^2, which is more than sufficient to display the whole area where THz radiation illuminates the grid object. The measurement range is restricted by the travel range of the translation stage. By padding the actual measured data with zeros, the back calculation is interpolated and therefore its resolution is increased from 4.55 pixels/cm to 9.1 pixels/cm. In comparison to the measured data, figure 4.5b shows the Fourier spectrum generated by simulating the propagation of a grid to the Fourier plane. There are no modifications to the previous object and data of chapter 3.5.2 with the exception of relating one pixel to 1.25 mm matching the grid dimensions for better comparability. The magnitude of the measurement and the simulation show the the same

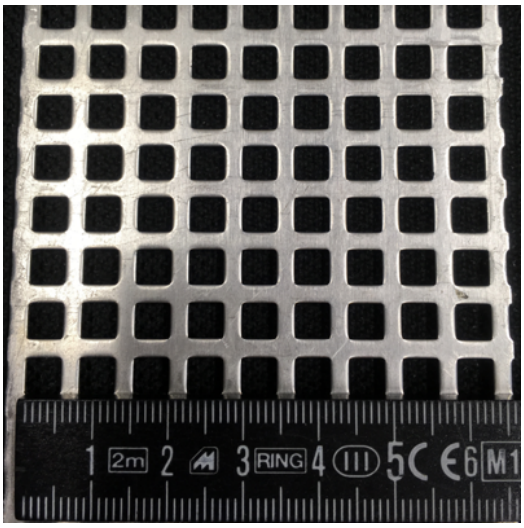

(a) Grid object

(b) Siemens-star object

Figure 4.4: (a) A picture of the used metal grid object with a ruler at the bottom. The square holes are 5x5 mm^2 in size and the opaque stripes are 2.5 mm wide. (b) A picture of the Siemens-star testchart with an outer and inner diameter of 105 mm and 5 mm respectively.

nine points with a similar diameter and relative strength to each other. Due to noise, shapeless noise can be seen specifically around the center spot of the measurement. Like the magnitude, the measured phase shares also some features with the simulated results. The nine spots which were already visible in the magnitude can be seen again. However, the simulation predicts concentric rings around the center spot, which are not visible in the measurement results. The back calculation of these two data sets are shown in figure 4.8. They both show the grid like pattern with round spots decreasing in intensity towards the edges of the round aperture.

Conducting the same measurement by inserting the Siemens-star object (see Fig. 4.4b)

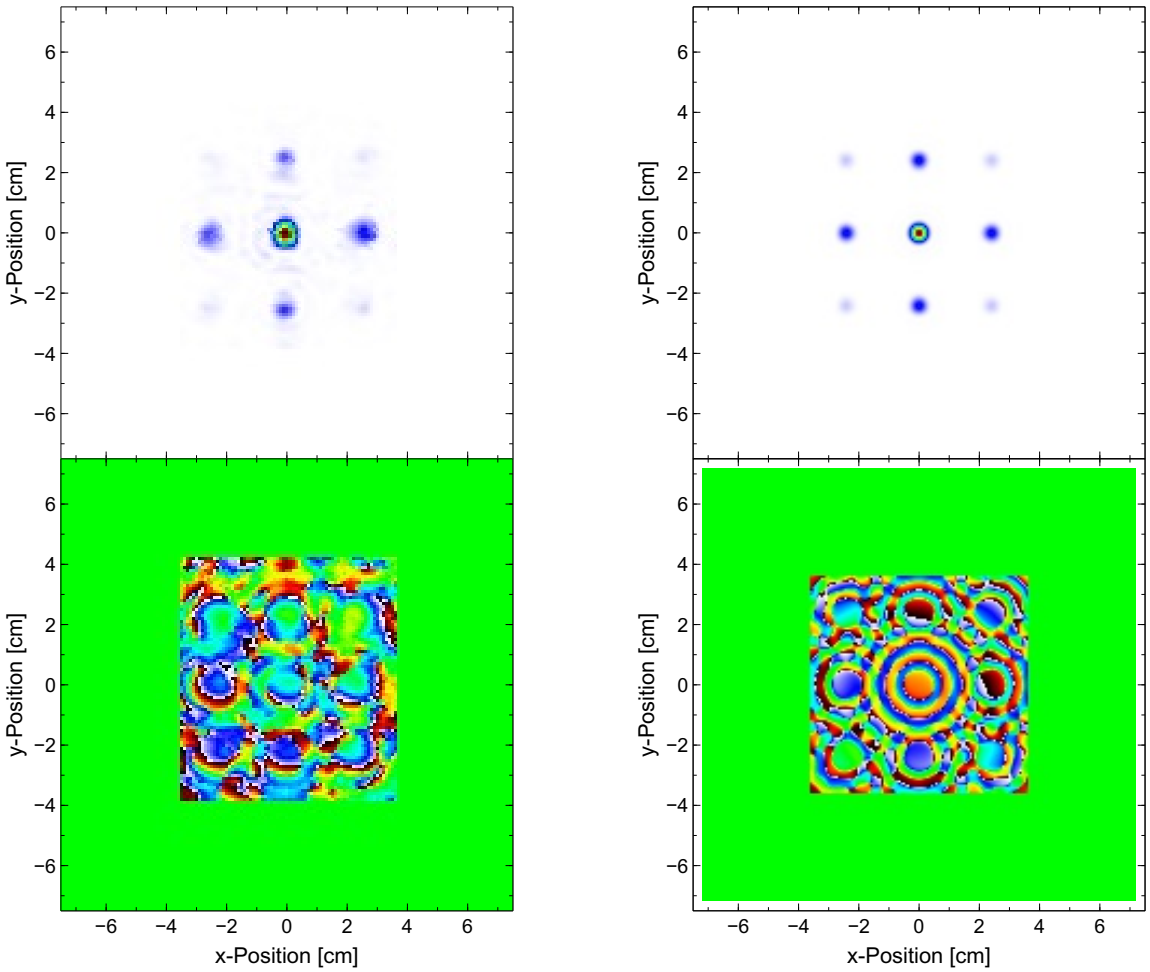

(a) Measured intensity and phase

(b) Simulated intensity and phase

Figure 4.5: (a) The intensity and phase of the grid object measured in the Fourier plane and padded with zeros. (b) The intensity and phase of the grid object simulated in the Fourier plane and padded with zeros.

in the collimated beam path (see Fig. 4.2), the Fourier spectrum with intensity and phase is measured, shown in figure 4.7a. Comparing the results with the results shown in figure 3.14, a number of similarities are visible, however some elements of the simulation do not match the measurement. The results at the right side in figure 4.7b, however, share many features of the measurement. Specially the phase matches very well. This is achieved by changing the simulation input situation. First, the object was modified to have twenty opaque metal fingers and the inner and outer diameter of the Siemens-star are changed to 4 pixels (5 mm) and 88 pixels (110 mm), respectively, to match the real test chart. Also the offset of the simulated Siemens-star was increased from 10 to 15 pixels. Just like before, the back calculation of the measurement and the back calculation of the simulation are displayed in figure 4.8a and 4.8b, respectively. Both show the highest intensity in the fingers while the simulation has a more evenly distributed intensity over the transparent regions in the center.

4.3.2 Measurements for different input to lens distances

In order to test the effect of different positions on the final image, the Siemens-star object is placed at four different positions in the collimated beam of the setup (Fig. 4.2) and

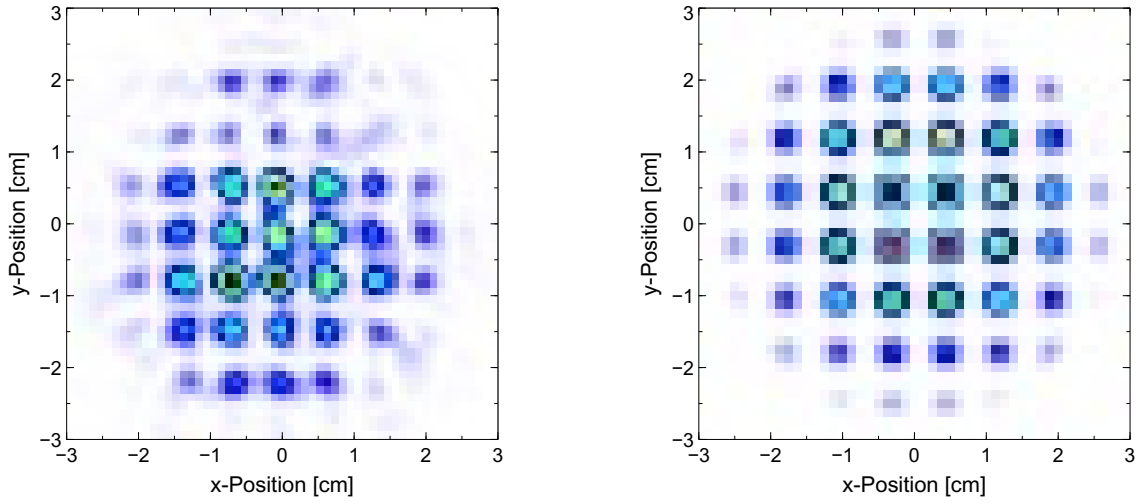

(a) Back calculation of measurement

(b) Back calculation of simulation

Figure 4.6: (a) Back calculation of the grid from the measured data in figure 4.5a. (b) Back calculation of the grid from the simulated data in figure 4.5b.

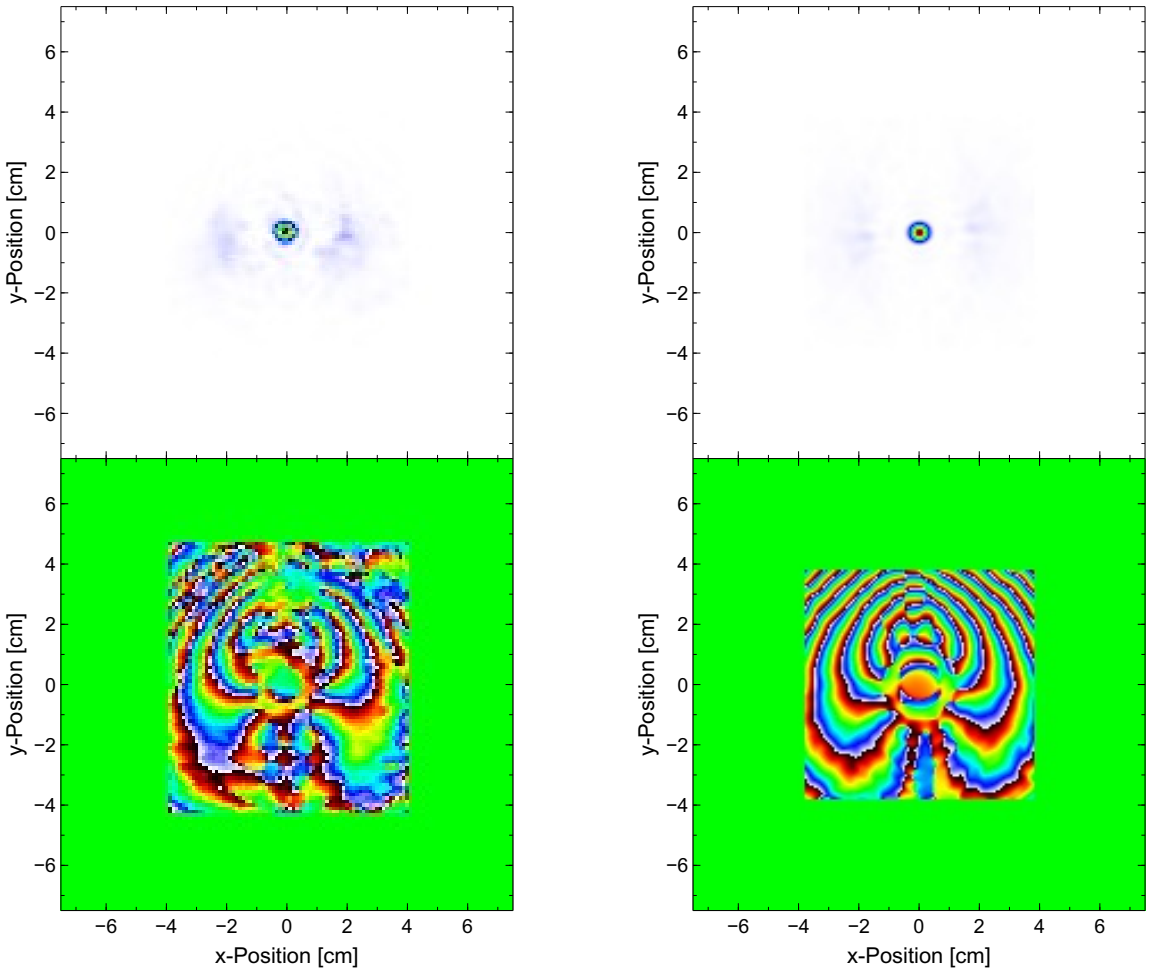

(a) Measured intensity and phase

(b) Simulated intensity and phase

Figure 4.7: (a) The intensity and phase of the grid object measured in the Fourier plane and padded with zeros. (b) The intensity and phase of the grid object simulated in the Fourier plane and padded with zeros..

their respective Fourier spectra are measured. The four different positions are 7, 9, 11 and 13 cm away from the focussing lens. Each set of data is used for back calculation, not only to its input plane but also to the distances of the other three data sets. The result is shown in figure 4.9. Each column stands for one set of data while each row represents the used distance for the back calculation. The sharpest image of the Siemens-star occurs where the used distance for back calculation matches the distance where the object is placed in the setup. It reaches for the normalised modulation transfer function (**MTF**) a value of $MTF_{50\%} \approx 0.1$ cycles/mm at 0.5 of the MTF [68–70]. This demonstrates the depth sensitivity of the presented imaging method. Even though the absolute distances

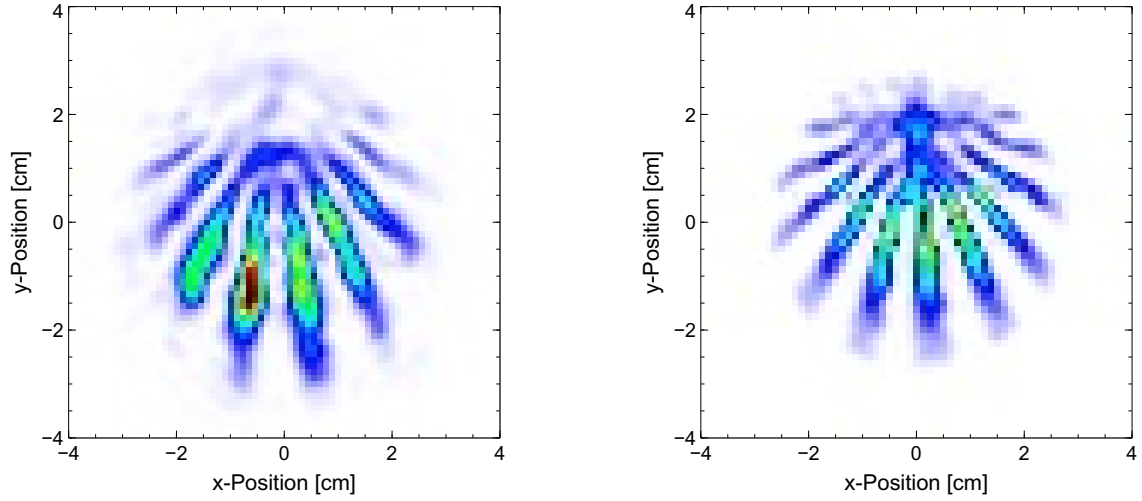

(a) Back calculation from measurement

(b) Back calculation from simulation

Figure 4.8: (a) Back calculation of the Siemens-star from the measured data in figure 4.7a. (b) Back calculation of the Siemens-star from the simulated data in figure 4.7b.

do not match the distances used for the simulation, the relative distances are the same. Blurring can be seen to depend only on the difference between actual (real or virtual) position and used distance for the back calculation.

So far, only objects with a high contrast are shown. However, the capability of displaying objects with lower contrast is crucial for general imaging applications. For this purpose, an "A" shaped piece of polyvinyl chloride (**PVC**) as shown in figure 4.10 is produced and inserted in to the collimated THz beam (see Fig. 4.3). Note, the setup without the beam splitter is used for this series of measurements. Figure 4.11 shows the same measurement presented before (see Fig. 4.9) but in this case the object is a low contrast piece of PVC. The intensity and the phase of the back calculation are shown in Fig. 4.11a and Fig. 4.11b, respectively. Again, for intensity and phase each column represents one measurement (at 8, 10, 12 and 14 cm) and every row represents a different distance (at 8, 10, 12 or 14 cm) for the back calculation. The THz radiation is not blocked by the PVC since 5 mm thickness reduces the transmitted intensity by about 60% [71]. Due to diffraction, the edges rather than the shape itself lack signal, which makes the "A" shape recognisable. For visibility, the colour scheme is logarithmic for the intensity plot. For transparent objects such as PVC, the phase shows a discontinuity at the edge due to the

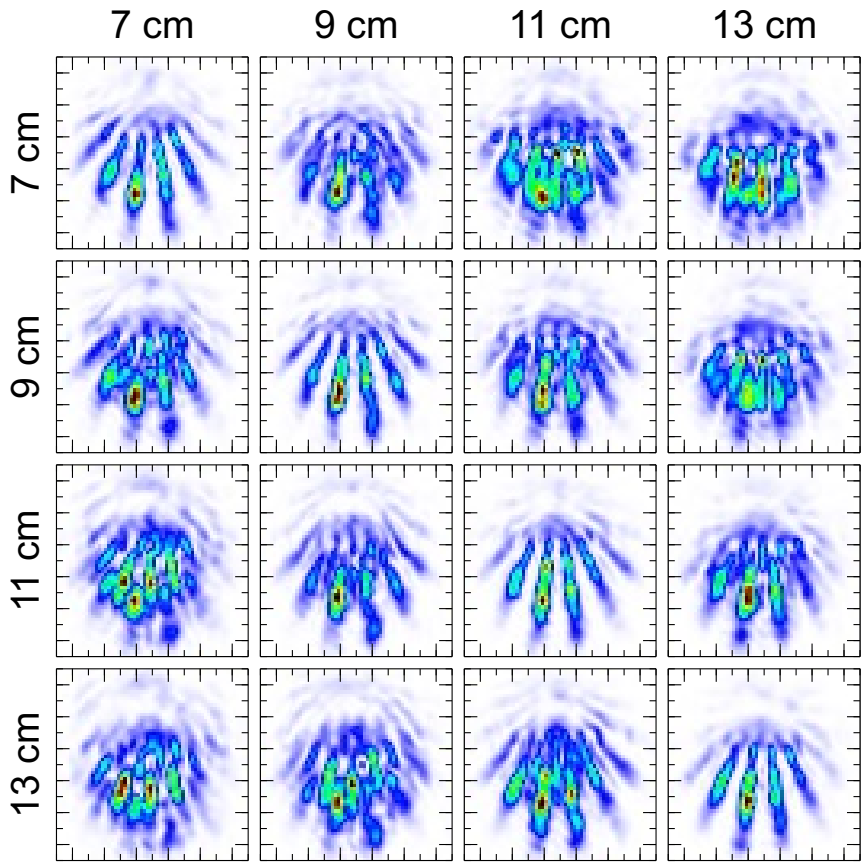

Figure 4.9: Each column represents a set of data at a distances 7, 9, 11 and 13 cm. Each row represents a set of back calculations with the back calculated distances 7, 9, 11 and 13 cm. The diagonal positions, where the back calculated distance match the real distance, the back calculation results in a sharp image of the Siemens-star input.

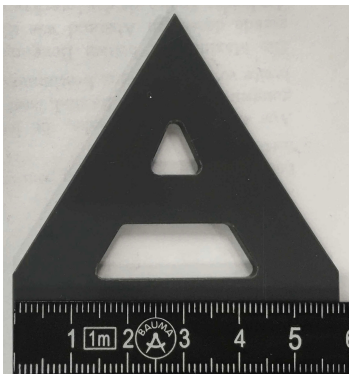

Figure 4.10: The used polyvinyl chloride (PVC) "A" object with a scale at the bottom.

optical path differences. As shown, the phase of the back calculation can help to interpret the result of the back calculation specially for transparent objects.

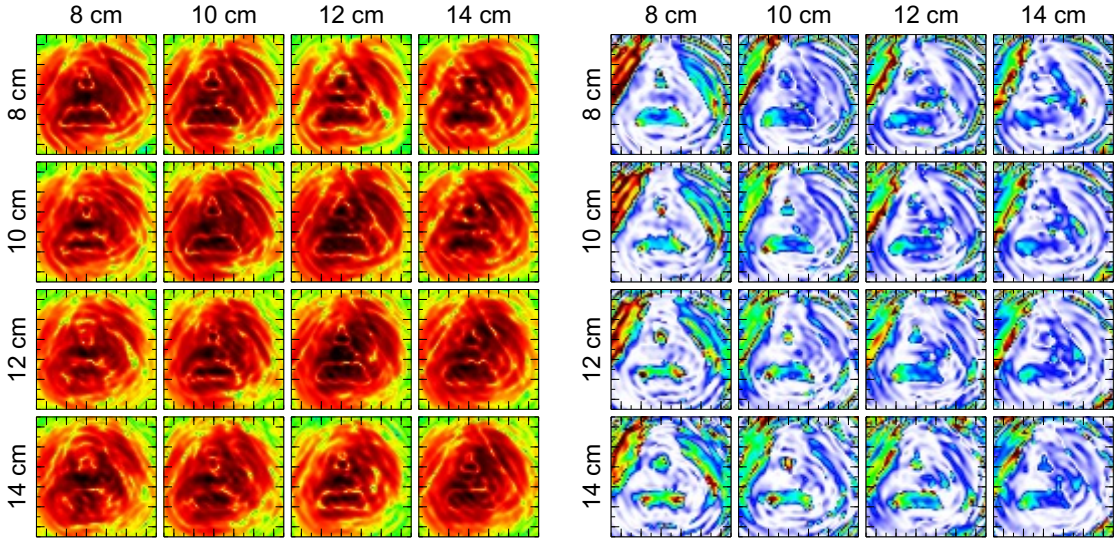

(a) Intensity of the back calculation (b) Phase of the back calculation

Figure 4.11: (a), (b) Plot of the back calculation's intensity (logaritc) and phase, respectively, for a PVC "A" which is placed at four different distances 8, 10, 12 and 14 cm plotted in each column. Each row represents one of the used distances 8, 10, 12 or 14 cm for the back calculation.

4.3.3 Three dimensional scene measurement

The sensitivity of the back calculation to the used distance can be exploited to "focus" on different positions and therefore different objects in the beam path. This enables a scanning through a three dimensional scene with different objects within the collimated beam. Figure 4.12a shows one measurement's back calculation for 8, 10, 12 and 14 cm distance (from top left to bottom right). Each panel shows a field of view of 10×10 cm^2 with a resolution of 9.03 pixel/cm. Two objects, the Siemens-star and the grid, are placed in the collimated beam path 14 cm and 8 cm in front of the lens, respectively. Consequently, these inputs should be visible for the back calculation at their respective distance. The grid object can be seen at the top left panel with some distortions. The residual three panels do not show any recognisable shape. Even the bottom right with the back calculation for 14 cm, which matches the distances of the Siemens-star, shows

no features of a Siemens-star. The right side of figure 4.12 shows again the simulation results of the previous chapter (see figure 3.17). The simulation data created resembles the measurement. The back calculation shows again a 10×10 cm^2 area with a 8 pixel/cm resolution which is close to the measurement specifications. Considering the finding of the simulation, the Siemens-star is not visible in the measurement's back calculation at its position of 14 cm in front of the lens. Reasons for this can be found in the measurement setup and the back calculation algorithm. Objects which are less opaque could improve the situation since the grid and Siemens-star each block a large portion of light. Without knowledge of the object's shape and position, it is not trivial to account for their impact on the field and requires further investigations.

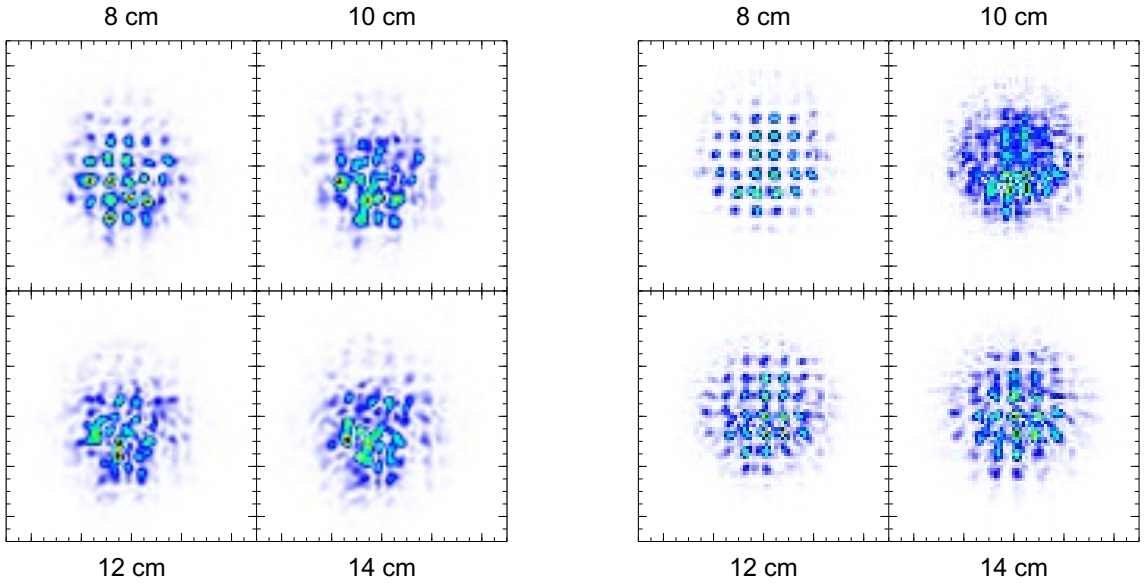

(a) Measured grid and Siemens-star

(b) Simulated grid and Siemens-star

Figure 4.12: Comparison between a measured and simulated three dimensional scene with grid and Siemens-star. (a) Measured scene with the grid placed 8 cm and the Siemens-star 14 cm away from the focussing lens. (b) Simulated scene with the grid placed 8 cm and the Siemens-star 14 cm away from the focussing lens.

4.4 Origins of noise in heterodyne imaging

Every measurement is affected by noise of various types and origins. The presented measurements are no exception and suffer from various different noise sources. In the two dimensional scanning process to measure intensity and phase with a single pixel detector, a number of different influential variables are conceivable as noise sources. The detector itselfe has an intrinsic noise dominated by the thermal Johnson-Nyquist noise [27, 72],

$$V_{noise} = \sqrt{4k_B T R}, \tag{4.7}$$

where k_B is the Boltzmann constant, T the temperature with $\approx 294K$ and R the resistance at the working point being $< 4k\Omega$ for this device, resulting in a total V_{noise} of < 10 nV. Therefore, the intrinsic noise of the detector is well below other influences and can be taken out of consideration. Simulations on how noise on the intensity and phase influences the back calculation were performed in the previous chapter (see section 3.4). There, it can be seen that noise on the phase has big consequences for the back calculation and recognisability. Relative intensity fluctuations do not have a high impact. However, coherent reflections from flat surfaces inside the beam path back to the Fourier plane could play a major role since those reflections add artefacts in the Fourier spectrum which then effect the back calculation. It is not trivial to quantify and identify the sources of noise which influence the spectrum the most and is still under investigation. The two noise sources which are believed to be the most critical are examined in the following section. The quantification of the influences, however, is not trivial and is also the subject of ongoing investigation.

4.4.1 Phase fluctuations

To enable Fourier imaging, the absolute phase is irrelevant while the relative phase plays the key role in the back calculation. Above, the generation of the reference for the lock-in amplifier is presented in subsection 4.2.1 where the electronics of the setup is introduced. By generating the intermediate frequency of the two synthesisers through

mixing a part of each signal, this intermediate frequency and its phase changes with small fluctuation of the output frequencies. Using this intermediate frequency as the reference for the lock-in amplifier dynamically accounts for frequency changes in the beat frequency (the difference frequency of signal and LO). Consequently, the relative phase is mostly immune to small frequency fluctuations of the synthesisers. In fact, the phase noise caused by the synthesiser is small enough to be neglected. This statement is strengthened by observations of the phase at a position with sufficient signal. However, phase fluctuations occur with a much higher variation in the regions where the signal is weak. This is common in regions of high spacial frequencies at the edges of the detection area. A reason for that is unwanted reflections, which take other than the designed beam path to the detector. At spatial frequencies where the signal strength of reflections is in the order of the direct beam, the lock-in amplifier locks to the reflections phase rather than to the desired one. Before this is adressed in the next subsection, one more factor inducing phase fluctuations will be mentioned. It must be kept in mind that the source arm and therefore the source is moved in this setup. The synthesiser device is too big to move along with the source and therefore the connecting cable which feeds the source with the synthesiser's signal is moved and bent during the scanning process. Bending a cable carrying a high frequency signal, however, leads to phase shifts of the signal [73]. To reduce the effect of this phenomenon, various different cable configurations are tested with the setup. The results show that short cables induce big phase shifts that back calculations do not show as a recognisable object. A long cable for connecting the synthesiser with the moving source improves the situation because the bending radius in a relative short cable is changed more than in a long cable.

4.4.2 Reflections inside the setup

Reflections from the surfaces in the setup back to the Fourier plane can be a major disturbing factor in the back calculation. Reflections not only add intensity where the initial Fourier spectrum should not show any or less, but also the phase is changed since the lock-in amplifier locks to the signal with a changed beam path. To limit the complexity,

only the first reflection is taken into consideration. Even though multiple different surfaces with different properties have to be accounted for. The reflection coefficient for parallel R_P and perpendicular R_S polarised light can be calculated with the refraction coefficients and the angle of incident with [74]

$$R_P = \left| \frac{n_1 \tan\theta_t - n_2 \tan\theta_i}{n_1 \tan\theta_t + n_2 \tan\theta_i} \right|^2 \text{ and} \tag{4.8}$$

$$R_S = \left| \frac{n_1 \tan\theta_i - n_2 \tan\theta_t}{n_1 \tan\theta_i + n_2 \tan\theta_t} \right|^2, \tag{4.9}$$

where n_1, n_2 are the refractive indices of the two media at the interface and θ_i, θ_t are the incident and transmission angle. Because conservation of energy, the transmittance is calculated with

$$T_P = 1 - R_P \text{ and} \tag{4.10}$$

$$T_S = 1 - R_S, \tag{4.11}$$

for parallel and perpendicular polarised light, respectively. For simplicity, the reflective index for perpendicular incident light to the surface is assumed, which yields,

$$R = \left| \frac{n_1 - n_2}{n_1 + n_2} \right|^2, \tag{4.12}$$

where transmission and reflection is independent of the polarisation.

Figure 4.13 shows a simplified setup which displays the numbered surfaces considered for the configuration without a beam splitter (see Fig. 4.3). The detector is glued on a piece of silicon waver on which the silicon lens is glued from the other side. For estimation, object ① is assumed to be a flat silicon surface which has a refraction index of 3.45 at 300 GHz [75] resulting in a reflectivity of ~ 0.3. The objects at ② and ④ are PTFE (Teflon) THz lenses [64] with a refraction index of 1.44 at 300 GHz [64, 76]. The reflectivity of 0.03 is rather low and the absorption of 0.4 cm^{-1} weakens the radiation with every transmission. The commercial Teflon lens is spherical shaped with a center thickness of 1.81 cm and 0.57 cm at the edge. Assuming an aperture of 6 cm in diameter

results in a average thickness of 1.57 cm which the radiation has to travel through the lens resulting in $0.6 \approx 0.4$ cm$^{-1} \cdot 1.57$ cm absorption. The metal object at position ③ is assumed to be a 50% free standing perfect reflector. The source at position ⑤ is composed of metal again which is in the worst case 100% reflecting back to the beam path when the focused reflection hits a metal part.

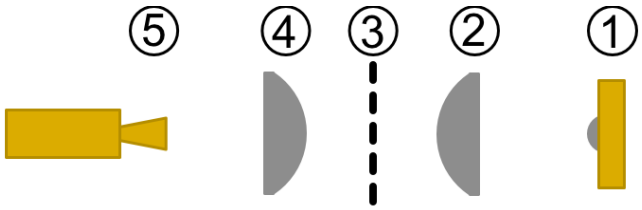

Figure 4.13: Simplified setup with numbered surfaces which have to be considered for reflection. Silicon at the detector position 1, Teflon (PTFE) at position 2 and 4, the object input at position 3 and the source at position 5.

With the coefficients above, four critical situations are identified where reflections might come back by a considerable amount to the detector. 30% of the radiation is reflected from the silicon back to the optical components. First surface to encounter on the way back is the fat side of the PTFE lens ② which reflects 3% back to the detection plane. However, the reflection is not focused by the lens but travels twice the focus distance. The diameter of the initial aperture has doubled to 12 cm, an area of 113 cm^2 over which the radiation is distributed. Since the detection range is only 64 cm^2, the detectable ratio of this radiation is only $\sim 57\%$. This means up to $0.005 \approx 0.3 \cdot 0.03 \cdot 0.57$ of the incident radiation on the detector is reflected back to the detector plane detecting an even smaller fraction at a time. The second situation to consider is the reflection at the object ③ . The radiation has to pass the Teflon lens two times where reflection and absorption take place. The ratio of radiation transmitted through the lens is calculated by the previously approximated absorption coefficient of 0.6 and considering two PTFE air interfaces resulting in $(1-0.6)\cdot 0.97^2 \approx 0.376$ transmission. If the object reflects 50%, the ratio which hits again the detector is estimated to be $0.3 \cdot 0.376^2 \cdot 0.5 \approx 0.021$. The third situation is the standing wave between source and detector. In the worst case, the source reflects completely, having the reflected radiation to pass four times through a Teflon lens

and two times the object. The reflected radiation, which reaches again the detector plane can be estimated to $0.3 \cdot 0.376^4 \cdot 0.5^2 \approx 0.0016$ for a 50% transmitting object which increases to 0.6% for no object. Depending on the object, the most prominent reflection occurs between ⑤ and ③ where the highest ratio of radiation with $0.071 \approx 0.376^2 \cdot 0.5$ returns on the beam path.

From above, the input object is identified as being the highest impact factor on disturbing reflections. The higher the reflectance of the input, the higher its impact. Especially the last considered case with an object of 50% metallisation could add 7% to the initial signal which drastically lowers the DR. It can be reduced by tilting the object by a certain degree making sure the reflection does not form standing waves in the setup.

4.5 Discussion and comparison

The feasibility of a phase sensitive heterodyne Fourier imaging setup is demonstrated using two commercial available 300 GHz electronic multiplier chain sources together with a TeraFET detector (CMOS or GaN/AlGaN). The majority of the presented measurements feature a beam splitter to superimpose LO and source (see Fig. 4.2). A second configuration of the setup is introduced as an alternative to the previous one and is intended to be used for future investigations (see Fig. 4.3). It is expected that the latter surpasses the previous configuration, since a beam splitter reduces signal and due to a limited aperture the order of spacial frequencies in the Fourier plane is restricted. Furthermore, removing the beam splitter simplifies the alignment and the overall setup. An increased flexibility is noted, since without the need of a beam splitter between focussing lens and detector, no minimum focus length is required to fit the additional optical component in the beam path. Removing the beam splitter is not the only difference between the two configurations. The detector technology was changed from GaN/AlGaN to CMOS because of increased sensitivity (for the used frequency) of the latter. Even though the configuration without the beam splitter shows a $\sim 30\%$ higher signal, the back calculations from measurements of the same object are too similar to favour one over the other in that perspective. In fact, the signal strength alone is no sufficient criteria to rate the perfor-

mance of a Fourier imaging setup, since disturbance due to reflections, phase shifts or similar play a much more important role for object reconstruction. In terms of alignment and flexibility, the setup without the beam splitter surpasses the previous one, but future experiments have to prove its superiority in imaging performance.

Figures 4.6 and 4.8 show the back calculation of the grid and Siemens-star, respectively, with the back calculation of the measurement on the left and the simulation on the right reaching a resolution of ≈ 2 mm. The simulation predicts an intensity and phase of the grid input in the focus plane which is also measured and shown side by side for comparison (see Fig. 4.5). The distinct intensity pattern of a Fourier transformed grid is visible in the measurement even though with visible noise. In contrast to the intensity which is only dependent on the grid's shape, the exact appearance of the phase is dependent on several more influences like distance of the object to the lens, offset of the Gaussian intensity distribution and aperture size. Therefore, the simulated and measured phase do not look much alike. The dot shaped phase islands in the positions of the intensity dots are the most prominent features which can be found with almost every simulation input (see Fig 3.13). Again, with some restrictions, these features are visible in the measured phase. Those measurements are sufficient enough to achieve a back calculated grid close to the simulated grid reconstruction. In order to quantify the similarity of the back calculation for simulation and measurement, the normalised cross correlation is used [77]. A maximum cross correlation of 72.87 % was found which can be stated as high correlation [78]. Obviously, the correlation has again a grid like pattern since the simulation and the measurement have the same periodicity (see figure A.5b). A similar situation is observed with the comparison of the Fourier plane data of the measured and simulated Siemens-star (see Fig. 4.7). The features of the intensity in the focus plane are not as distinctive as the grids intensity pattern. However, the simulation and measurement show similarities. Just like before, the phase of the Siemens-star is also very dependent on the same input parameter as for the grid input. The simulation, however, is very much like the measurement. The measurement shows the same features with even the same absolute values observable. This is a good agreement and therefore results in a back calculation shown in figure 4.8a close to the prediction of the simulation. However, the

maximum calculated cross correlation is with 65.51 % for simulation and measurement back calculation lower than the grid's result which is reasonable since the Siemens-star is more complicated than the grid object. Also the correlation pattern is more distinct than the simulation and measured grid correlation (see figure A.5a). To summarise, grid and Siemens-star measurements result in sufficient good data for reconstructing the inputs. Further investigations are planed to include a reference measurement without object in the beam path to increase reconstruction quality.

Simulations show a high enough depth sensitivity to distinguish between different positions of the input in front of the lens (see Fig. 3.16). The sharpest input is reconstructed for the virtual distance of the input object which is experimentally confirmed. In a series of measurements, the Siemens-star test chart is placed at several positions from 7 cm to 13 cm away from the lens (see Fig. 4.9). It is easy to see that the clearest image of the Siemens-star is where the back calculation distance matches the real distance. The sharpness of the back calculation is only dependent on the relative difference between used distance for the back calculation and actual distance. This is best seen in the simulation where the same relative distances result in the exact same reconstruction. The back calculation of the measurement does not show this behaviour revealing an asymmetry in the experiments. This irregularity can be reasoned with several different origins. For example in an inaccurate positioning of the objects, a noisy detection process or not perfectly collimated light to name a few explanations.

Another series of measurements feature a PVC "A" as the input object (see Fig. 4.11). A PVC object provides a low contrast because it is transparent for THz radiation. The PVC input can still be seen in the back calculations. This is due to the diffraction at the object's edges as well as the phase of the back calculation. The reconstructed objects quality does not degenerate as quickly with increasing relative distance to the real input as it is observed with the Siemens-star input. Future experiments have to investigate on this behaviour which might be disturbing for reconstruction of a three dimensional scene or a transparent volume.

By placing multiple opaque objects in the beam path, a three dimensional scene was created which was simulated with two objects by numerically propagating the first input

to the second input and to the Fourier plane from there. The simulations reveal that it is not trivial to reconstruct two opaque objects in the beam path at their respective input distances. One reason is the altered field incident on the second object and the shadowing of the first by the second. Secondly, it is questionable if a simple back calculation is adequate, since in the present simulations and measurement, the influence on the light field of the closer object is ignored for the back calculation of the object further away from the lens and vice versa. This complicated situation requires special attention and a more careful approach as simply ignoring the first input object when calculating the second or the other way around. Further investigations on existent data have to be undertaken by altering the reconstruction algorithm optimising it for a three dimensional scene reconstruction. For future measurements, it must be considered to expand the detection range or shortening the focus length to include higher spacial frequencies into the calculation to gather more data which is necessary for a thee dimensional scene reconstruction. However, one has to be sure to resolve the intensity and phase features in the Fourier plane or information about the object will be lost. Also, one has to keep in mind that even when in principle a large area can be scanned to attempt high resolution of the back calculation, the wavelength will still limit the achievable resolution because the electromagnetic wave does not resolve the small features, diminishing its high spacial frequencies in the regions far away from the center. The wavelength dependent k-vector can also be used to obtain a Fourier spectrum without performing a 2D raster scan. Hichem Guerboukha and his team exploid this fact using a TDS setup [79]. There, the scanning happens in a circle considering the different frequencies present in the short pulse to sample the k-space. This is an interesting solution but one has to be sure that the transmission of the investigated object is not frequency dependent. The setup's sources in the present work emits just one frequency at a time which makes the frequency scan more difficult.

5 Conclusion and Outlook

There have been many approaches in the realisation of THz imaging for various applications using different sources, detectors and techniques with advantages and disadvantages to each method [10, 79–86]. This work presents two novel systems for THz imaging. The two set-ups are related to the purpose of THz imaging but are otherwise separately discussed in chapters on low-repetition-rate THz pulse detection and Fourier imaging.

5.1 Low-repetition-rate terahertz pulse imaging and spectroscopy sensing

In summary, single pulse detection is realised using low repetition THz pulses from a commercial available Q-switched OPO THz source, the "Firefly-THz" in conjunction with a TeraFET detector based on GaN/AlGaN technology for the first time. A double stage amplification circuit based on low noise operational amplifier was designed and fabricated to visualise each pulse with an ordinary oscilloscope enabling video rate imaging.

The quality of the source's cavity is switched by a high voltage, inducing an ubiquitous pulsed electric field which can be picked up by any cable in the set-up. Shielding the detector from the high voltage is achieved by including the detector and the amplification circuit with batteries as power supply in a metal housing. Also, the gate voltage is supplied with a battery. By applying these measures, single pulse detection with a maximum pulse to pulse signal to noise ratio of 25.5 and a dynamic range of 300 at 0.8 THz is achieved. The source's THz pulses carry enough power to drive the detector in saturation which indicates that the pulse energy is high enough to be distributed over multiple detectors enabling single shot imaging with a detector array. The principle of imaging

is demonstrated using a scanning set-up achieving a lateral resolution of 1.2 mm. The spectroscopy capabilities of the set-up were demonstrated using the explosive simulant PABA where the absorption at 0.8 THz was resolved. Although, the highest sensitivity of the detector is not within the tuning range of the Firefly-THz resulting in a strong decreasing signal over the spectrum, the TeraFET detector was shown to be a capable detection system together with Firefly-THz [47].

Attempts to increase the SNR by referencing the THz output with the corresponding infrared or pump signal of the THz generation did not succeed. Further studies are necessary to identify characterise the cascade effect and their threshold in the non liner OPO process. With a strong correlation, a high increase of signal to noise ratio could be achieved even if the THz output power has to be decreased. Furthermore, the sensitivity of the detector is not matched with the tuning range of the "Firefly-THz". Further studies using this kind of set-up should include a TeraFET with an antenna optimised to between 0.8 and 1.7 THz. Special care has to be taken that a detector with its highest sensitivity near the maximum output power is not exposed by the focused intensity of the "Firefly-THz" in order to avoid saturation or even destruction of the detector. A detector array with appropriate actuators could be used to record a hole area with frame rates up to 90 Hz resulting in a real time recording in the THz regime.

5.2 Fourier imaging through terahertz heterodyne detection

The second main topic addresses the concept, simulation and accomplishment of THz Fourier imaging. The simulations which are based on the Fresnel diffraction integral, are performed to study an electric field illuminating an input object and its propagation to the focus plane. Numerical studies also help to predict properties, features and potential outcomes of an experimental measurements. Two electrical multiplier chain THz sources are used in a heterodyne configuration to enable phase sensitive image detection of a TeraFET detector for the first time. Simple input objects like a metal grid and a Siemens-

star test chart are clearly recognisable and the predicted depth sensitivity is demonstrated.

The simulations give an idea of which objects create which characteristic intensity and phase pattern. Numerical calculations also help to predict the impact of noisy intensity and phase on the back calculation. Obviously, different objects result in different Fourier spectra with the highlighted spacial frequencies from the features of the object. It can be shown that the phase is more important in the Fourier plane than the intensity for the input retrieval. Therefore, the back calculation suffers less from noise on the intensity than from noise on the phase which also carries the depth information. Corresponding measurements with the grid and Siemens-star object were performed achieving the predicted depth sensitivity for numerical focussing and a lateral resolution of 2 mm. The retrieved input of the objects results in a high correlation with the numeric prediction (see section 4.5) making it easy to distinguish between the objects. Multiple objects in the beam path prove to be challenging for the presented set-up in the current configuration. Nevertheless, heterodyne detection enables to capture a 3D scene by numerical focussing to different depth after taking one set of data. Also, Fourier optics allows to generate a large, low resolution image by taking high resolution, compact data and vice versa.

The lateral resolution is currently restricted by the scanning range. To increase the resolution of the retrieved input, future experiments have to increase the range in k space. This can either be achieved by increasing the travel of the translation stages or lower the focus length and/or the wavelength. As mentioned before, coherent reflections change the phase in the Fourier plane and therefore have a high impact on the quality of the reconstruction. The coherent length in succeeding experiments has to be carefully shortened to reduce standing waves but not destroy the phase behaviour of the Fourier spectrum. To make use of the measurement's resolution in the Fourier plane, the field of view has to be broadened in the Fourier setup and filter the THz beam so that the object is illuminated with a homogeneous intensity distribution instead of a Gaussian one. Using the current setup, there is no estimate on how precise the phase curvature was measured and therefore how depth sensitive the measurements are. In conclusion, this study realises the potential of THz sources for applications in imaging and spectroscopy.

List of Figures

Appendices

A Complementary Figures

The appendices include some pictures which were believed to not fit in the continuous text but are still interesting additional material for the reader's consideration.

A.1 Pulsed terahertz detection

Section 2.3.2 addresses the topic of parasitic effects during the nonlinear optical process in the OPO. Without taking good care about the reflexes in the "Firefly-THz" one can easily couple out frequencies which were never designed to leave the output window of the source as one can see through a IR-viewer (see Fig. A.1).

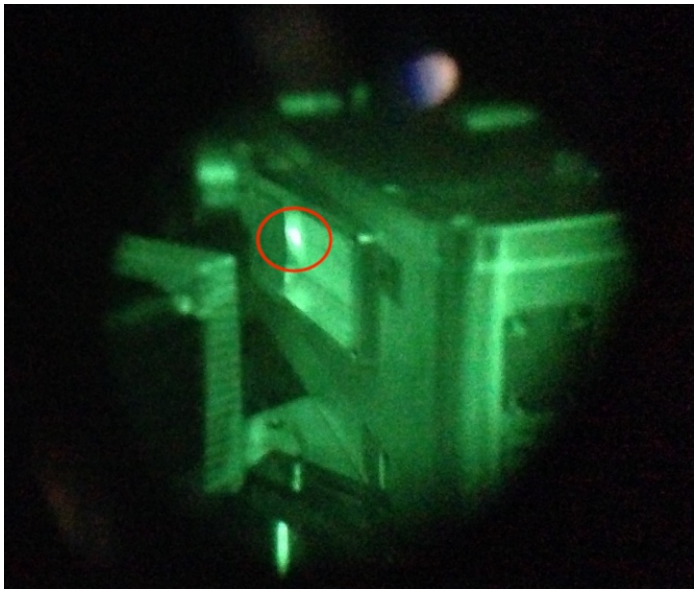

Figure A.1: View of the Firefly-THz output window through a IR-viewer. The area with increased IR intensity at the corner of the output window is highlighted in red.

The simultaneous detection with several detectors at the same time reduces acquisition time if the radiation is distributed over multiple detectors. A possible implementation is shown in figure A.2c. The detector array was used to generate the THz image scan (see Fig. A.2b) of a cell phone (see Fig. A.2a).

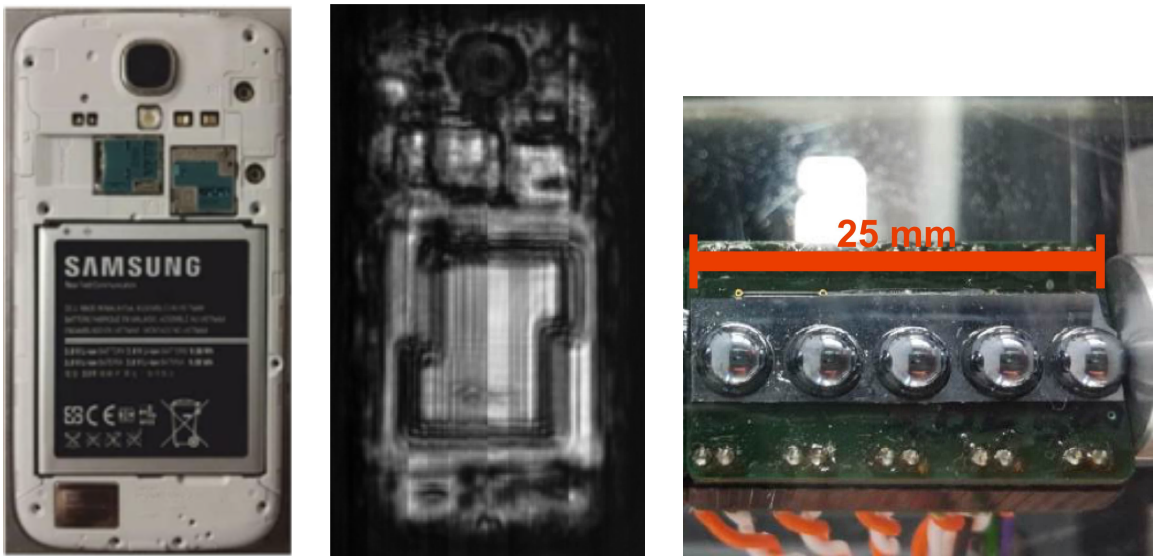

(a) Cell phone image (b) THz image (c) Detector array with silicon lenses

Figure A.2: (a) Optical image of a cell phone without the back cover. (b) Reflective THz image scan of the cell phone where one can easily see different metal parts as bright areas. (c) Used detector array seen from the back with each detector featuring a 4 mm hemispherical silicon lens with a total width of 25 mm.

A.2 Fourier optics simulation

As an interesting test to demonstrate the importance of the phase in the Fourier transform, one can Fourier transform two total different images and swap their resulting phases. The inverse Fourier transform shows the features of the image of the phase. The figure below (Fig. A.3) demonstrates this small experiment.

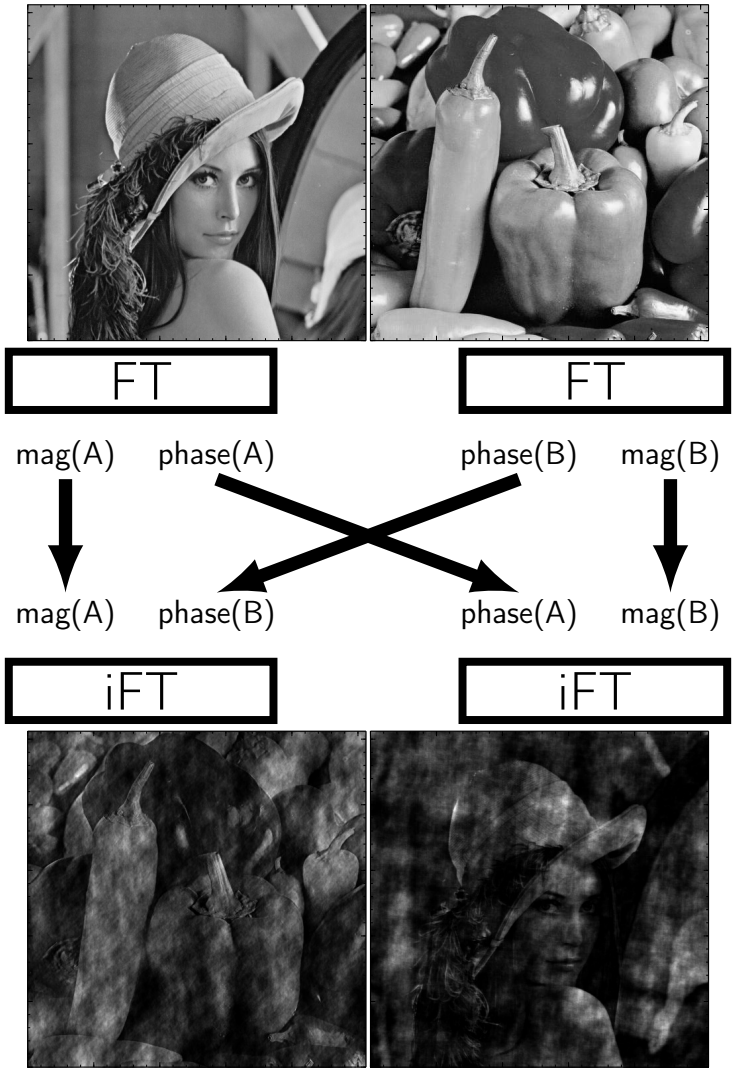

Figure A.3: The top row shows two pictures which were Fourier transformed and its phase and amplitude were switched before the inverse Fourier transform with its result shown in the bottom row.

A.3 Terahertz Fourier imaging

The local oscillator in a heterodyne measurement setup interferes with the probing signal and forms the beat frequency. The setup presented in section 4.2.3 uses a linear approach without a beam splitter. The local oscillator forms a standing wave between source and detector. This leads to field enhancements for frequencies with constructive interference. This can be seen in the figure below (Fig. A.4) in the frequency range between 240 and 320 GHz.

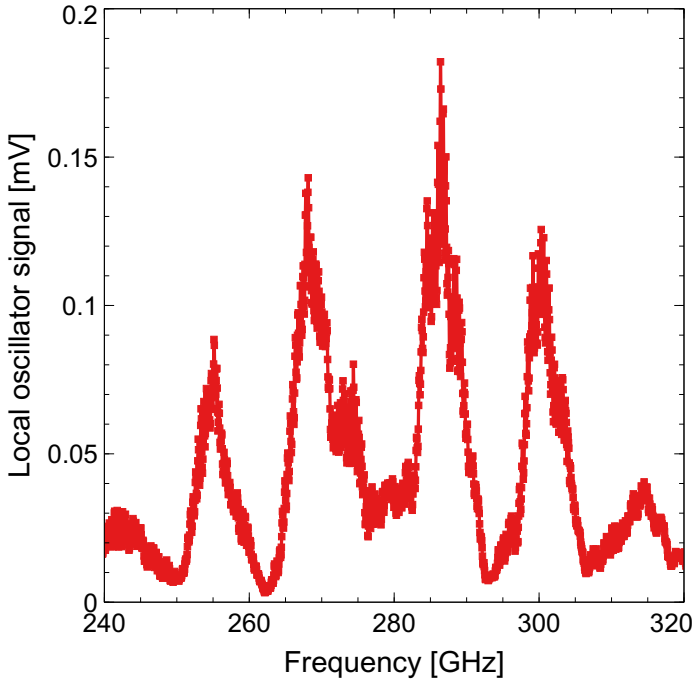

Figure A.4: The spectrum of the local oscillator response where standing waves lead to field enhancements.

In order to calculate a cross correlation between two figures, their resolution must be matched. The way the algorithm works is that the first picture is padded with zeros half the side length (width or height) of the second image. The second picture is placed at each position of the padded first picture and the correlation for that picture position is calculated. This generates another figure of correlation where each pixel represents the value of correlation between the two pictures where a value of one represents the perfect match. Below, this cross correlation can be seen for the grid and the Siemens-star data set on the left and right, respectively (see Fig. A.5). The correlation of the grid is again a

grid. Because of its periodicity, the images look similar every grid period. The correlation of the Siemens-star, however, looks more complicated. In the case of chapter 4.3, only the maximum value is of interest.

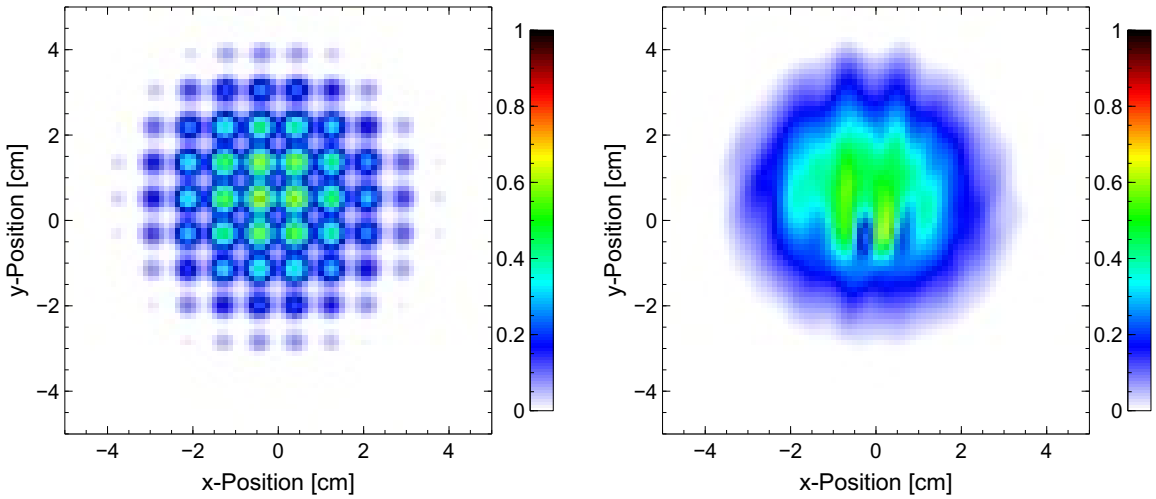

(a) Normalised cross correlation of grid

(b) Normalised cross correlation of Siemens-star

Figure A.5: Normalised cross correlation of the back calculation of the measured and simulated Fourier spectrum. The back calculation's correlation of simulation and measurement from the grid Fourier spectrum is shown on the left. The right shows the corresponding figure of the Siemens-star.

B Python code for Fourier optic simulation and back calculation

B.1 Implemented functions

```
#import modules
from scipy import constants      #for constants
import numpy as np               #for maths

def create_x_and_y(real_grid_period, grid_period, N):
        """This function creates x and y arrays that...
         contain a zero element with resolution...
         'grid_period/real_grid_period'."""
    if N%2:
        limit = real_grid_period*(N-1)/grid_period/2
        x = np.linspace(-limit,limit,N)
    else:
        limit = real_grid_period*N/grid_period/2
        x = np.linspace(-limit,limit,N, endpoint = False)

    if N%2:
        limit = real_grid_period*(N-1)/grid_period/2
        y = np.linspace(-limit,limit,N)
    else:
```

```
        limit = real_grid_period*N/grid_period/2
        y = np.linspace(-limit,limit,N, endpoint = False)
    return x,y
```

```
def create_xf_and_yf(x,y,lam,f):
    """Creates the coordinates for the Fourier plane."""
    nx = np.size(x)
    ny = np.size(y)
    fx_max = (nx-1)/(x.ptp() * 2)
    fy_max = (ny-1)/(y.ptp() * 2)

    if nx%2:
        xf = lam*f*np.linspace(-fx_max, fx_max,
                               nx, endpoint = True)
    else:
        xf = lam*f*np.linspace(-fx_max, fx_max,
                               nx, endpoint = False)

    if ny%2:
        yf = lam*f*np.linspace(-fy_max, fy_max,
                               ny, endpoint = True)
    else:
        yf = lam*f*np.linspace(-fy_max, fy_max,
                               ny, endpoint = False)
    return xf, yf
```

```
def sim_field_through_inf_lens(field, x, y, frequency,
                        focal_length, dist_obj, dist_screen):

    def my_fft(array):
        """Internal function for the FFT"""
        return np.fft.fftshift(np.fft.fft2(
                                np.fft.ifftshift(array)))

    if np.shape(field) == (np.size(y),np.size(x)):
        #the shape has to fit with the dimensions of x and y
        c = constants.c #speed of light
        nx = np.size(x)
        ny = np.size(y)

        nu = frequency
        f = focal_length
        d = dist_obj

        lam = c/nu
        k0 = 2*np.pi/lam

        #define the dimensions
        xx, yy = np.meshgrid(x,y)
        xf,yf = create_xf_and_yf(x,y,lam,f)
        xxf, yyf = np.meshgrid(xf, yf)

        Exy0 = field #complex field array

        F0 = my_fft(Exy0*np.exp(1j*k0/2*(xx**2+yy**2)
                        *(1/f-1/dist_screen)))
```

```
        U_f = 1j*F0/(lam*dist_screen)
                *np.exp(-1j*k0/2*(1/dist_screen-d/f**2)
                *(xxf**2+yyf**2))

    else:
        raise RuntimeError("The length of x and y have
                        to match the dimensions of 'field'.")
    return U_f, xf, yf
```

```
def retrieve_object_from_field(field, xf, yf, frequency,
                        focal_length, dist_obj, dist_screen):

    def my_ifft(array):
        """Internal function for the iFFT"""
        return np.fft.fftshift(np.fft.ifft2(
                                np.fft.ifftshift(array)))

    if np.shape(field) == (np.size(yf),np.size(xf)):
        c = constants.c #the speed of light
        nx = np.size(xf)
        ny = np.size(yf)

        nu = frequency
        f = focal_length
        d = dist_obj

        lam = c/nu              #wave length
        k0 = 2*np.pi/lam        #wave vector

        #define the dimensions
        xxf, yyf = np.meshgrid(xf, yf)
        fx = xf/(lam*f)
        fy = yf/(lam*f)
        x_step = 1/(np.abs(fx).max()*2)
        y_step = 1/(np.abs(fy).max()*2)
```

```
        #define x and y making sure there is a 0 element
        if nx%2:
            x = np.linspace((-nx+1)/2,(nx-1)/2,
                            nx, endpoint = True)*x_step
        else:
            x = np.linspace(-nx/2,nx/2,
                            nx, endpoint = False)*x_step
        if ny%2:
            y = np.linspace((-ny+1)/2,(ny-1)/2,
                            ny, endpoint = True)*y_step
        else:
            y = np.linspace(-ny/2,ny/2,
                            ny, endpoint = False)*y_step

        xx, yy = np.meshgrid(x, y)

        PXY = ((1j*k0)/(2*np.pi*dist_screen))
                *np.exp(-1j*k0/2*(1/dist_screen-d/f**2)
                        *(xxf**2+yyf**2))
        F0_back = field / PXY
        E0_back =  my_ifft(F0_back)
                *np.exp(1j*k0/2*(xx**2+yy**2)
                        *(1/f-1/dist_screen))
    else:
        raise RuntimeError("The length of x and y have to
                        match the dimensions of 'field'.")

    return E0_back, x, y
```

B.2 Fourier simulation script

```
#import modules
import matplotlib.pyplot as plt #plotting module
from scipy import constants     #for constants
import numpy as np              #for maths
import mycode                   #custom functions


################   defining input parameters   ################
c = constants.c          #the speed of light [m/s]
N = 201                  #the pixel number for the NxN field
d = 0.1                  #distance object to the lens [m]
f = 0.15                 #focus length of the lens [m]
screen_dist = 0.15       #detection plane distance [m]
nu = 13.27*18*10**9      #frequency [Hz]
lam = c/nu               #wavelength
k0 = 2*np.pi/lam         #wave vector

# define a relation between real size and representation
grid_period = 6 #pixel
grid_width = 2 #pixel
real_grid_period = 0.0075 #[m]
real_grid_width = 0.0025 #[m]
##############################################################
```

```
##############   create object transparency   ##############
Ixy1 =  mycode.aperture((N,N),22)
        *mycode.gaussian((N,N),9,9,1,2)
        *mycode.create_grid((N,N),grid_period,grid_width)
#############################################################

#generate x and y so that there is a zero element
x,y = mycode.create_x_and_y(real_grid_period,grid_period,N)

#create field at the input transparencies
phixy0 = np.zeros((N,N))                #zero phase
Exy1 = np.sqrt(Ixy1)*np.exp(1j*phixy0)  #E-field


#################   Fourier simulation   ###################
#simulate input
U_f1, xf, yf = mycode.sim_field_through_inf_lens(
                Exy1,x,y,nu,f,d,screen_dist)

#modifications on the simulation result come here

#back calculation
E_b1, x, y = mycode.retrieve_object_from_field(
                U_f1,xf,yf,nu,f,d,screen_dist)
#############################################################

#calculate intensity and phase
intensityFourierPlane = np.abs(U_f1)**2
phaseFourierPlane = np.angle(U_f1)
intensityBackCalculation = np.abs(E_b1)**2
```

```
######################    plot results    ######################
fig = plt.figure()
mycode.center_plot(Ixy1,Ixy1.shape)
plt.colorbar()

fig = plt.figure()
mycode.center_plot(intensityFourierPlane,U_f1.shape,xf,yf)
plt.colorbar()

fig = plt.figure()
mycode.center_plot(phaseFourierPlane,U_f1.shape,xf,yf)
plt.colorbar()

fig = plt.figure()
mycode.center_plot(intensityBackCalculation,E_b1.shape)
plt.colorbar()

plt.show()
```

Bibliography

[1] W. Herschel, "Xiv. experiments on the refrangibility of the invisible rays of the sun", *Philosophical Transactions of the Royal Society of London*, vol. 90, pp. 284–292, 1800.

[2] P. E. Hockberger, "A history of ultraviolet photobiology for humans, animals and microorganisms", *Photochemistry and Photobiology*, vol. 76, no. 6, pp. 561–579, Mar. 2002.

[3] H. Rubens and E. F. Nichols, "Heat rays of great wave length", *Phys. Rev. (Series I)*, vol. 4, pp. 314–323, Jan. 1897. DOI: 10.1103/PhysRevSeriesI.4.314.

[4] J. HEY, "Reports on the progress of astronomy radio astronomy", *Monthly Notices of the Royal Astronomical Society*, vol. 109, no. 2, pp. 179–214, 1949.

[5] A. Rogalski, "History of infrared detectors", *Opto-Electronics Review*, vol. 20, no. 3, pp. 279–308, Sep. 2012. DOI: 10.2478/s11772-012-0037-7.

[6] M. Tonouchi, "Cutting-edge terahertz technology", *Nature Photonics*, vol. 1, 97 EP, Feb. 2007. DOI: 10.1038/nphoton.2007.3.

[7] R. R. A. Pavel Shumyatsky, "Terahertz sources", *Journal of Biomedical Optics*, vol. 16, pp. 16–10, 2011. DOI: 10.1117/1.3554742.

[8] S. S. Dhillon, M. S. Vitiello, E. H. Linfield, A. G. Davies, M. C. Hoffmann, and et al., "The 2017 terahertz science and technology roadmap", *Journal of Physics D: Applied Physics*, vol. 50, no. 4, p. 043 001, 2017.

[9] P. H. Siegel, "Terahertz technology", *IEEE T. Microw. Theory Tech.*, vol. 50, pp. 910–928, 2002.

[10] K. J. Siebert, T. Löffler, H. Quast, M. Thomson, T. Bauer, R. Leonhardt, S. Czasch, and H. G. Roskos, "All-optoelectronic continuous wave thz imaging for biomedical applications", *Phys. Med. Biol.*, vol. 47, pp. 3743–3748, 2002.

[11] P. L. Richards, "Bolometers for infrared and millimeter waves", *Journal of Applied Physics*, vol. 76, no. 1, pp. 1–24, 1994. DOI: 10.1063/1.357128.

[12] H. Wang, X. Yi, J. Lai, and Y. Li, "Fabricating microbolometer array on unplanar readout integrated circuit", *International Journal of Infrared and Millimeter Waves*, vol. 26, no. 5, pp. 751–762, May 2005. DOI: 10.1007/s10762-005-4983-8.

[13] N. Palka, P. Zagrajek, A. Czerwinski, T. Trzcinski, E. Rurka, M. Szustakowski, and M. Sypek, "Hot electron bolometer for detection of fast terahertz pulses from optical parametric oscillator", in *Millimetre Wave and Terahertz Sensors and Technology V*, N. Salmon and E. Jacobs, Eds., ser. Proceedings of SPIE, vol. 8544, 2013. DOI: 10.1117/12.974490.

[14] Q. Han, T. Gao, R. Zhang, Y. Chen, J. Chen, G. Liu, Y. Zhang, Z. Liu, X. Wu, and D. Yu, "Highly sensitive hot electron bolometer based on disordered graphene", *Scientific Reports*, vol. 3, no. 3533, Dec. 2013. DOI: 10.1038/srep03533.

[15] V. Dobrovolsky and F. Sizov, "A room temperature, or moderately cooled, fast thz semiconductor hot electron bolometer", *Semiconductor Science and Technology*, vol. 22, no. 2, p. 103, 2007.

[16] M. J. E. Golay, "Theoretical consideration in heat and infra-red detection, with particular reference to the pneumatic detector", *Review of Scientific Instruments*, vol. 18, no. 5, pp. 347–356, 1947. DOI: 10.1063/1.1740948.

[17] K. Kawase, Y. Ogawa, H. Minamide, and H. Ito, "Terahertz parametric sources and imaging applications", *Semicond. Sci. Technol.*, vol. 20, S258, 2005.

[18] G. P. A. Malcolm, D. A. Walsh, and M. Chateauneuf, "Physics and applications of t-rays", in *Physics and Applications of Terahertz Radiation*, Springer, 2014, pp. 149–175.

[19] Nov. 2018. [Online]. Available: `http://www.m2lasers.com/Lasers.html`.

[20] K. Kawase, Y. Ogawa, Y. Watanabe, and H. Inoue, "Non-destructive terahertz imaging of illicit drugs using spectral fingerprints", *Opt. Express*, vol. 11, pp. 2549–2554, 2003.

[21] F. Z. Meng, M. D. Thomson, D. Molter, T. Löffler, J. Jonuscheit, R. Beigang, J. Bartschke, T. Bauer, M. Nittmann, and H. G. Roskos, "Coherent electro-optical detection of terahertz radiation from an optical parametric oscillator", *Opt. Express*, vol. 18, pp. 11 316–11 326, 2010.

[22] W. Knap, F. Teppe, Y. Meziani, N. Dyakonova, J. Lusakowski, F. Boeuf, T. Skotnicki, D. Maude, S. Rumyantsev, and M. S. Shur, "Plasma wave detection of sub-terahertz and terahertz radiation by silicon field-effect transistors", *Appl. Phys. Lett.*, vol. 85, pp. 675–677, 2004.

[23] E. Öjefors, U. Pfeiffer, A. Lisauskas, and H. G. Roskos, "A 0.65 thz focal-plane array in a quarter-micron cmos process technology", *IEEE J. Solid-St. Circ.*, vol. 44, pp. 1968–1976, 2009.

[24] S. Boppel, A. Lisauskas, M. Mundt, D. Seliuta, L. Minkevičius, I. Kašalynas, G. Valušis, M. Mittendorff, S. Winnerl, V. Krozer, and H. G. Roskos, "Cmos integrated antenna-coupled field-effect transistors for the detection of radiation from 0.2 to 4.3 thz", *IEEE T. Microw. Theory Tech.*, vol. 60, pp. 3834–3843, 2012.

[25] A. Lisauskas, U. Pfeiffer, E. Öjefors, P. Haring Bolívar, D. Glaab, and H. G. Roskos, "Rational design of high-responsivity detectors of terahertz radiation based on distributed self-mixing in silicon field-effect transistors", *J. Appl. Phys.*, vol. 105, p. 114 511, 2009.

[26] S. Regensbuger, M. Mittendorff, S. Winnerl, H. Lu, A. C. Gossard, and S. Preu, "Broadband thz detection from 0.1 to 22thz with large area field-effect transistors", *Opt. Express*, vol. 23, pp. 20 732–20 742, 2015.

[27] M. Bauer, R. Venckevičius, I. Kašalynas, S. Boppel, M. Mundt, L. Minkevičius, A. Lisauskas, G. Valušis, V. Krozer, and H. G. Roskos, "Antenna-coupled field-effect transistors for multi-spectral terahertz imaging up to 4.25 thz", *Opt. Express*, vol. 22, no. 16, pp. 19 235–19 241, 2014. DOI: 10.1364/OE.22.019235.

[28] A. Lisauskas, M. Bauer, S. Boppel, M. Mundt, B. Khamaisi, E. Socher, R. Venckevičius, L. Minkevičius, I. Kašalynas, D. Seliuta, G. Valušis, V. Krozer, and H. G. Roskos, "Exploration of terahertz imaging with silicon mosfets", *J. Infrared Millim. Te.*, vol. 35, pp. 63–80, 2014.

[29] M. Naftaly and R. Dudley, "Methodologies for determining the dynamic ranges and signal-to-noise ratios of terahertz time-domain spectrometers", *Opt. Lett.*, vol. 34, pp. 1213–1215, 2009.

[30] R. A. Barrett, *Broadband rf power detector using fet*, Mar. 1987.

[31] H. G. Krekels, B. Schiek, and E. Menzel, "Power detector with gaas field effect transistors", in *1992 22nd European Microwave Conference*, vol. 1, Sep. 1992, pp. 174–179. DOI: 10.1109/EUMA.1992.335736.

[32] J. Grzyb and U. Pfeiffer, "Thz direct detector and heterodyne receiver arrays in silicon nanoscale technologies", *J. Infrared Millim. Te.*, vol. 36, pp. 998–1032, 2015.

[33] J. Zdanevičius, M. Bauer, S. Boppel, V. Palenskis, A. Lisauskas, V. Krozer, and H. G. Roskos, "Camera for high-speed thz imaging", *J. Infrared Millim. Te.*, vol. 36, pp. 986–997, 2015.

[34] R. A. Hadi, H. Sherry, J. Grzyb, Y. Zhao, W. Förster, H. M. Keller, A. Cathelin, A. Kaiser, and U. R. Pfeiffer, "A 1 k-pixel video camera for 0.7-1.1 terahertz imaging applications in 65-nm cmos", *IEEE J. Solid-St. Circ.*, vol. 47, pp. 2999–3012, 2012.

[35] S. Boppel, A. Lisauskas, V. Krozer, and H. G. Roskos, "Performance and performance variations of sub-1 thz detectors fabricated with 0.15 mu m cmos foundry process", *Electron. Lett.*, vol. 47, pp. 661–662, 2011.

[36] D. J. Cheney, E. A. Douglas, L. Liu, C.-F. Lo, B. P. Gila, F. Ren, and S. J. Pearton, "Degradation mechanisms for gan and gaas high speed transistors", *Materials*, vol. 5, pp. 2498–2520, 2012.

[37] M. Bauer, A. Rämer, S. Boppel, S. Chevtchenko, A. Lisauskas, W. Heinrich, V. Krozer, and H. G. Roskos, "High-sensitivity wideband thz detectors based on gan hemts with integrated bow-tie antennas", in *10th European Microwave Integrated Circuits Conference (EuMIC)*, IEEE, 2015, pp. 1–4.

[38] S. Boppel, M. Ragauskas, A. Hajo, M. Bauer, A. Lisauskas, S. Chevtchenko, A. Rämer, I. Kašalynas, G. Valušis, H. J. Würfl, W. Heinrich, G. Tränkle, V. Krozer, and H. G. Roskos, "0.25- µm gan terafets optimized as thz power detectors and intensity-gradient sensors", *IEEE T. THz Sci. Techn.*, vol. 6, pp. 348–350, 2016.

[39] Y.-F. Sun, J.-D. Sun, X.-Y. Zhang, H. Qin, B.-S. Zhang, and D.-M. Wu, "Enhancement of terahertz coupling efficiency by improved antenna design in gan/algan high electron mobility transistor detectors", *Chin. Phys. B*, vol. 21, p. 108 504, 2012.

[40] J. Van Rudd and D. M. Mittleman, "Influence of substrate-lens design in terahertz time-domain spectroscopy", *J. Opt. Soc. Am. B*, vol. 19, no. 2, pp. 319–329, 2002.

[41] D. F. Filipovic, S. S. Gearhart, and G. M. Rebeiz, "Double-slot antennas on extended hemispherical and elliptical silicon dielectric lenses", *IEEE Trans. Microw. Theory Tech.*, vol. 41, pp. 1738–1749, 1993.

[42] N. Dyakonova, P. Faltermeier, D. B. But, D. Coquillat, S. D. Ganichev, W. Knap, K. Szkudlarek, and G. Cywinski, "Saturation of photoresponse to intense thz radiation in algan/gan hemt detector", *J. Appl. Phys.*, vol. 120, p. 164 507, 2016.

[43] W. Zouaghi, D. Voß, C. McDonnell, D. Mundy, J. R. P. Bain, N. Hempler, G. P. Malcolm, G. T. Maker, A. Rämer, S. A. Chevtchenko, W. Heinrich, V. Krozer, and H. G. Roskos, "Real-time detection of the thz pulses from a thz opo using algan/gan terafets", in *41st International Conference on Infrared, Millimeter, and Terahertz waves (IRMMW-THz)*, 2016.

[44] N. Palka, "Thz reflection spectroscopy of explosives measured by time domain spectroscopy", *Acta Phys. Pol. A*, vol. 120, pp. 713–715, 2011.

[45] C. R. Phillips, J. S. Pelc, and M. M. Fejer, "Continuous wave monolithic quasi-phase-matched optical parametric oscillator in periodically poled lithium niobate", *Optics letters*, vol. 36, no. 15, pp. 2973–2975, 2011.

[46] D. J. M. Stothard, I. D. Lindsay, and M. H. Dunn, "Continuous-wave pump-enhanced optical parametric oscillator with ring resonator for wide and continuous tuning of single-frequency radiation", *Opt. Express*, vol. 12, no. 3, pp. 502–511, Feb. 2004. DOI: 10.1364/OPEX.12.000502.

[47] D. Voß, W. Zouaghi, M. Jamshidifar, S. Boppel, C. McDonnell, J. R. P. Bain, N. Hempler, G. P. A. Malcolm, G. T. Maker, M. Bauer, A. Lisauskas, A. Rämer, S. A. Shevchenko, W. Heinrich, V. Krozer, and H. G. Roskos, "Imaging and spectroscopic sensing with low-repetition-rate terahertz pulses and gan terafet detectors", *Journal of Infrared, Millimeter, and Terahertz Waves*, vol. 39, no. 3, pp. 262–272, Mar. 2018. DOI: 10.1007/s10762-017-0447-1.

[48] F. Schuster, D. Coquillat, H. Videlier, M. Sakowicz, F. Teppe, L. Dussopt, B. Giffard, T. Skotnicki, and W. Knap, "Broadband terahertz imaging with highly sensitive silicon cmos detectors", *Opt. Express*, vol. 19, no. 8, pp. 7827–7832, Apr. 2011. DOI: 10.1364/OE.19.007827.

[49] J. W. Goodman, *Introduction to Fourier optics*, ser. McGraw-Hill physical and quantum electronics series. The McGraw-Hill companies, 1968, ISBN: 007023776X.

[50] R. N. Bracewell, *The Fourier transform and its applications*, 2. ed., ser. McGraw-Hill electrical and electronic engineering series. McGraw-HIll, 1978, ISBN: 007007013x.

[51] H. D. Meikle, *A new twist to Fourier transforms*. Wiley-VCH, 2004, ISBN: 3527404414.

[52] J. F. James, *A student's guide to Fourier transforms : with applications in physics and engineering*, 2. ed. Cambridge University Press, 2002, ISBN: 052180826X.

[53] E. O. Brigham, *The fast Fourier Transform*. Englewood Cliffs, NJ : Prentice-Hall, 1974, ISBN: 013307496X.

[54] P. R. Griffiths and J. A. DeHaseth, *Fourier Transform Infrared Spectroscopy*. Wiley, 1986, ISBN: 978-0-471-19404-0.

[55] D. Meschede, *Optik, Licht und Laser*, 3., durchges. Aufl. Vieweg +Teubner, 2008, ISBN: 978-3-8351-0143-2.

[56] W. Zinth and U. Zinth, *Optik : Lichtstrahlen - Wellen - Photonen*, 4., aktualisierte Aufl. Oldenbourg Verlag München, 2013, ISBN: 9783486721362.

[57] D. Kühlke, *Optik : Grundlagen und Anwendungen*, 3., überarb. und erw. Aufl. Verlag Harri Deutsch, 2011, ISBN: 9783817118786.

[58] B. E. A. Saleh and M. C. Teich, *Fundamentals of photonics*. John Wiley and Sons, Inc., 1991, ISBN: 9780471839651.

[59] J. W. Goodman, R. B. Miles, and R. B. Kimball, "Comparative noise performance of photographic emulsions in holographic and conventional imagery", *J. Opt. Soc. Am.*, vol. 58, no. 5, pp. 609–614, May 1968. DOI: 10.1364/JOSA.58.000609.

[60] A. Yariv and P. Yeh, *Photonics : optical electronics in modern communications*, 6. ed., ser. Oxford series in electrical and computer engineering. Oxford University Press, 2007, ISBN: 9780195179463.

[61] M. T. Faber, J. Chramiec, and M. E. Adamski, *Microwave and Millimeter-Wave Diode Frequency Multipliers*. Artech House, 1995.

[62] E. Camargo, *Design of FET Frequency Multipliers and Harmonic Oscillators*, ser. Artech House microwave library. Artech House, 1998, ISBN: 9780890064818.

[63] J. Ward, E. Schlecht, G. Chattopadhyay, A. Maestrini, J. Gill, F. Maiwald, H. Javadi, and I. Mehdi, "Capability of thz sources based on schottky diode frequency multiplier chains", in *2004 IEEE MTT-S International Microwave Symposium Digest (IEEE Cat. No.04CH37535)*, vol. 3, 2004, 1587–1590 Vol.3.

[64] Mar. 2018. [Online]. Available: `www.thorlabs.com`.

[65] J. Kröll, J. Darmo, and K. Unterrainer, "Metallic wave-impedance matching layers for broadband terahertz optical systems", *Opt. Express*, vol. 15, no. 11, pp. 6552–6560, May 2007. DOI: `10.1364/OE.15.006552`.

[66] R. Han, C. Jiang, A. Mostajeran, M. Emadi, H. Aghasi, H. Sherry, A. Cathelin, and E. Afshari, "25.5 a 320ghz phase-locked transmitter with 3.3mw radiated power and 22.5dbm eirp for heterodyne thz imaging systems", in *2015 IEEE International Solid-State Circuits Conference - (ISSCC) Digest of Technical Papers*, Feb. 2015, pp. 1–3. DOI: `10.1109/ISSCC.2015.7063118`.

[67] M. T. Reiten and R. A. Cheville, "Effect of spherical aberration and surface waves on propagation of lens-coupled terahertz pulses", *Opt. Lett.*, vol. 30, no. 6, pp. 673–675, Mar. 2005. DOI: `10.1364/OL.30.000673`.

[68] K. Rossmann, "Point spread-function, line spread-function, and modulation transfer function", *Radiology*, vol. 93, no. 2, pp. 257–272, 1969. DOI: `10.1148/93.2.257`.

[69] P. F. Judy, "The line spread function and modulation transfer function of a computed tomographic scanner", *Medical Physics*, vol. 3, no. 4, pp. 233–236, 1976. DOI: `10.1118/1.594283`.

[70] S. D. S. Jason A. Mazzetta, *Automated testing of ultraviolet, visible, and infrared sensors using shared optics*, 2007. DOI: `10.1117/12.719532`.

[71] R. Piesiewicz, C. Jansen, S. Wietzke, D. M. Mittleman, M. Koch, and T. Kürner, "Properties of building and plastic materials in the thz range", 2007.

[72] J. D. Sun, Y. F. Sun, D. M. Wu, Y. Cai, H. Qin, and B. S. Zhang, "High-responsivity, low-noise, room-temperature, self-mixing terahertz detector realized using floating antennas on a gan-based field-effect transistor", *Applied Physics Letters*, vol. 100, no. 1, p. 013 506, 2012. DOI: 10.1063/1.3673617.

[73] J. J. Krempasky, "Analysis of tem mode on a curved coaxial transmission line", *IEEE Transactions on Microwave Theory and Techniques*, vol. 38, no. 6, pp. 739–747, Jun. 1990. DOI: 10.1109/22.130968.

[74] M. Born and E. Wolf, *Principles of Optics: Electromagnetic Theory of Propagation, Interference and Diffraction of Light*. Elsevier Science, 2013, ISBN: 9781483103204.

[75] M. N. Afsar and K. J. Button, "Millimeter-wave dielectric measurement of materials", *Proceedings of the IEEE*, vol. 73, no. 1, pp. 131–153, Jan. 1985.

[76] M. N. Afsar, "Precision millimeter-wave measurements of complex refractive index, complex dielectric permittivity, and loss tangent of common polymers", *IEEE Transactions on Instrumentation and Measurement*, vol. IM-36, no. 2, pp. 530–536, Jun. 1987.

[77] J. P. Lewis, "Fast template matching", in *Vision interface*, vol. 95, 1995, pp. 15–19.

[78] M. Kozak, "What is strong correlation?", *Teaching Statistics*, vol. 31, no. 3, pp. 85–86, 2009. DOI: 10.1111/j.1467-9639.2009.00387.x.

[79] H. Guerboukha, K. Nallappan, and M. Skorobogatiy, "Exploiting k-space/frequency duality toward real-time terahertz imaging", *Optica*, vol. 5, no. 2, pp. 109–116, Feb. 2018. DOI: 10.1364/OPTICA.5.000109.

[80] H. Zhong, A. Redo, Y. Chen, and X. .-.-. Zhang, "Standoff distance detection of explosive materials with thz waves", in *2005 Joint 30th International Conference on Infrared and Millimeter Waves and 13th International Conference on Terahertz Electronics*, vol. 1, Sep. 2005, 42–43 vol. 1. DOI: 10.1109/ICIMW.2005.1572397.

[81] Z. D. Taylor, R. S. Singh, D. B. Bennett, P. Tewari, C. P. Kealey, N. Bajwa, M. O. Culjat, A. Stojadinovic, H. Lee, J. Hubschman, E. R. Brown, and W. S. Grundfest, "Thz medical imaging: In vivo hydration sensing", *IEEE Transactions on Terahertz Science and Technology*, vol. 1, no. 1, pp. 201–219, Sep. 2011. DOI: 10.1109/TTHZ.2011.2159551.

[82] G. C. Trichopoulos, H. L. Mosbacker, D. Burdette, and K. Sertel, "A broadband focal plane array camera for real-time thz imaging applications", *IEEE Transactions on Antennas and Propagation*, vol. 61, no. 4, pp. 1733–1740, Apr. 2013. DOI: 10.1109/TAP.2013.2242829.

[83] H. Song and T. Nagatsuma, "Present and future of terahertz communications", *IEEE Transactions on Terahertz Science and Technology*, vol. 1, no. 1, pp. 256–263, Sep. 2011. DOI: 10.1109/TTHZ.2011.2159552.

[84] K. Tanaka, H. Hirori, and M. Nagai, "Thz nonlinear spectroscopy of solids", *IEEE Transactions on Terahertz Science and Technology*, vol. 1, no. 1, pp. 301–312, Sep. 2011. DOI: 10.1109/TTHZ.2011.2159535.

[85] H.-B. Liu, G. Plopper, S. Earley, Y. Chen, B. Ferguson, and X.-C. Zhang, "Sensing minute changes in biological cell monolayers with thz differential time-domain spectroscopy", *Biosensors and Bioelectronics*, vol. 22, no. 6, pp. 1075–1080, 2007. DOI: 10.1016/j.bios.2006.02.021.

[86] D. Saeedkia, *Handbook of terahertz technology for imaging, sensing and communications*. Elsevier, Jan. 2013, ISBN: 9780857092359.

Danksagung

An dieser Stelle michte ich allen Meschen danken, die diese Arbeit möglich gemacht haben. Ein besonderer Dank geht daher an Herrn Prof. Dr. Hartmut Roskos für das entgegengebrachte Vertrauen und die Überlassung der Projekte. Ich danke allen ehemaligen und aktuellen Mitgliedern der Arbeitsgruppen von Prof. Roskos und Prof. Krozer sowie der Werkstatt für das sehr gute Arbeitsklima in freundschaftlicher Atmosphäre. Eine besondere Erwähnung gebührt hier Alvydas Lisauskas als meinen ersten Ansprechpartner, der während der Forschungsarbeit von unschätzbarem Wert war.

Auch meine Kollegen, die während meiner Zeit in Schottland mir stets mit Rat zur Seite standen, möchte ich nicht unerwähnt lassen. Vor allem Wissem Zouaghi, Sebastian Boppel, Mehran Jamshidifar und Cormac McDonnell haben mich dort tatkräftig unterstützt, woraus in Cormacs Fall eine wertvolle Freundschaft entstanden ist. Im Rahmen der Forschungsarbeit in Frankfurt hat David Mundy einen großartigen Grundstein gelegt und Hui Yuan durch ihren Ideenreichtum frischen Auftrieb gebracht. Beiden bin ich zu großem Dank verpflichted. Viele weitere großartige Menschen bleiben hier leider unerwähnt, doch meine Korrekturleser verdienen nochmals ein tiefempfundenes Dankeschön. Darunter finden sich meine großartige Freundin Sandra Salzwedel, Tobias Lohrey, Hui Yuan und Cormac McDonnell, die sich meine Dissertation in sprachlicher und fachlicher Hinsicht zur Brust genommen haben.

Nicht zuletzt können sich meine langjährigen Freunde, meine Freundin Sandra und insbesondere meine Eltern meiner allergrößten Dankbarkeit sicher sein. Sie sorgten durch zahlreiche Aktivitäten, regelmäßige Treffen und Gespräche für den nötigen Ausgleich. Sie sind immer für mich da und brachten mir die Geduld und das Verständnis entgegen, das mich durch alle Höhen und Tiefen getragen hat und tragen wird.